Contents

List of Figures

List of Tables

List of Equations

List of Abbreviations

ACL	Average Chain Length
APC	Average Product Correction
CC	Correlation Coefficient
CMO	Contact Map Overlap
DCA	Direct Coupling Analysis
EC	Evolutionary Coupling
eLLG	expected Log-Likelihood Gain
FP	False Positive
KDE	Kernel Density Estimate
LLG	Log-Likelihood Gain
M_{eff}	Number of Effective Sequences
MAE	Mean Absolute Error
MR	Molecular Replacement
MSA	Multiple Sequence Alignment
MX	Macromolecular Crystallography
NMR	Nuclear Magnetic Resonance
NOE	Nuclear Overhauser Effect
PDB	Protein Data Bank
PDBTM	Protein Data Bank of Transmembrane Proteins

RIO	Residue-Independent Overlap
RMSD	Root Mean Square Deviation
SML	Supervised Machine Learning
TFZ	Translation Function Z-score
TM-score	Template-Modelling score
TP	True Positive

Chapter 1

Introduction

1.1 Macromolecular X-ray crystallography

The discovery of X-ray diffraction by crystals by Max van Laue [1, 2] marked the origins of modern crystallography. However, it was not until the work of William Lawrence Bragg and William Henry Bragg that X-ray scattering could be translated into atomic positions [3–5]. Since then, X-ray crystallography and the determination of atomic positions in organic and inorganic molecules of has come a long way and shaped the path for many 21st century discoveries. Amongst those ground-breaking discoveries are the earliest structural models of biological molecules including DNA [6], vitamin B12 [7], and the first protein structures [8–11]. These structure elucidations hallmarked the dawn of a new era in biological and biomedical research. At the time of writing, 124,551 structural models were determined by X-ray diffraction studies [12], and thus X-ray crystallography is a key method in biological research.

1.1.1 X-ray scattering

X-rays are high energy photons part of the electromagnetic spectrum with a wavelength 0.1-100Å [13]. X-rays can be described as packets of travelling electromagnetic waves, whose electric field vector interacts with the charged electrons of matter [13]. Such interaction, typically termed scattering, results in the diffraction of the incoming wave, which X-ray crystallography relies on.

In its simplest form, scattering of X-ray radiation can be explained in the scenario of exposure to a single free electron. The resulting scattering can be classed as elastic (Thomson scattering) or inelastic (Crompton scattering) [13]. The latter — scattering that results in a loss of energy of the emitting photon due to energy transfer onto the electron — does not contribute to discrete scattering, the type of scattering X-ray diffraction relies on. In comparison, Thomson scattering does not result in a loss of energy of the emitting photon. This has significant effects, the incoming photon emits with the same frequency causing the electron to oscillate identically further enhancing the signal.

If we expand the example to include all electrons in an atom and expose the atom to X-ray radiation, our theory needs to be slightly expanded. Given that one or more electrons in an atom are not free but orbit around the atom's nucleus in a stable and defined manner, the distribution of these electrons around the nucleus determines the scattering of the incoming X-ray photons. The distribution of scattered photon waves is thus an overall representation of the probability distributions of each electron in the atom and is refered to as electron density $\rho(\boldsymbol{r})$. In X-ray scattering, it suffices to approximate the shape of the electron density to a sphere. If we now consider the emitting wave $\boldsymbol{s_1}$ of an X-ray photon scattered by any position $\boldsymbol{r}$ in the electron density of an atom, then the phase difference $\Delta\varphi$ to the incoming wave $\boldsymbol{s_0}$ can be described by Eq. 1.1 [13].

$$\Delta\varphi = 2\pi \left(\boldsymbol{s_1} - \boldsymbol{s_0}\right) \boldsymbol{r} = 2\pi \cdot \boldsymbol{Sr} \tag{1.1}$$

If more than one electron in an atom's electron density scatter the incoming X-ray wave, then the emitting partial waves can be described by the atomic scattering function f_s (Eq. 1.2), which describes the interference of all scattered waves [13]. The total scattering power of an atom is proportional to the number of electrons and element-specific with heavier atoms scattering more strongly. Given the approximation of a centrosymmetric electron density, the atomic scattering function is also symmetric.

$$f_s = \int_{\boldsymbol{r}}^{V(atoms)} \rho\left(\boldsymbol{r}\right) \cdot e^{2\pi i \boldsymbol{Sr}} \cdot d\boldsymbol{r} \tag{1.2}$$

With an enhanced understanding of X-ray scattering of electrons orbiting a single atom, it is important to consider X-ray scattering of adjacent atoms, such as it is typically found in molecules. If the electromagnetic wave of a X-ray photon excites all electrons of adjacent atoms, then the resulting partial waves result in constructive or destructive interference. Maximal interference can be obtained when all partial waves are in phase, and maximal destructive interference when out-of-phase. This leads to varying intensities of the emitting X-ray photon at different points in space. To obtain the overall scattering power F_s of all contributing atoms, Eq. 1.2 needs to be modified to include the sum over all atoms j as described in Eq. 1.3.

$$F_s = \sum_{j=1}^{atoms} f_{s,j}^{0} \cdot e^{2\pi i \boldsymbol{Sr}_j} \tag{1.3}$$

If we now translate our hypothetical experiment into a crystal lattice then our understanding described in Eq. 1.3 needs to be expanded from a 1-dimensional distance vector $\boldsymbol{r}$ to the three dimensional lattice translation vectors $\boldsymbol{a}$, $\boldsymbol{b}$ and $\boldsymbol{c}$. The Laue equations (Eq. 1.4) do exactly that and ultimately determine the positions of the diffraction peaks in 3-dimensional space.

$$\boldsymbol{S} \cdot \boldsymbol{a} = n_1, \qquad \boldsymbol{S} \cdot \boldsymbol{b} = n_2, \qquad \boldsymbol{S} \cdot \boldsymbol{c} = n_3 \tag{1.4}$$

$$n\lambda = 2d_{hkl} sin\theta \tag{1.5}$$

Such determination is possible through the findings made by Bragg and Bragg [3], who identified the relationship between the scattering vector $\boldsymbol{S}$ and the planes in the crystal lattice. Today, this relationship is defined by the Bragg equation (Eq. 1.5) [3], which allows us to interpret X-ray diffraction as reflections on discrete lattice planes, which relates the diffraction angle θ to the lattice spacing d_{hkl} (Fig. 1.1) [13]. For maximum diffraction n needs to be integer multiples to result in maximum constructive interference of wavelength λ.

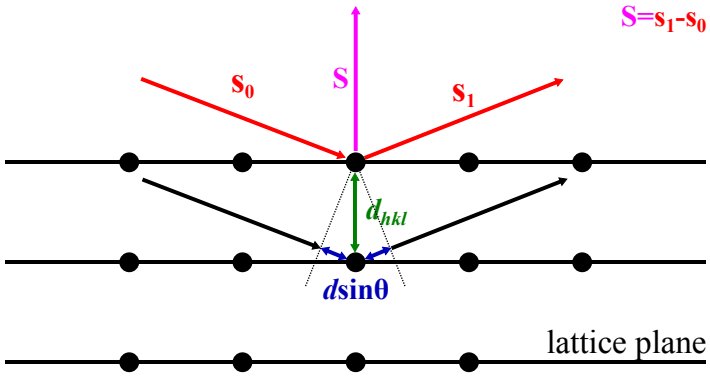

Figure 1.1: Schematic of Bragg scattering.

Lastly, if the hypothetical model is expanded to molecular crystals, then the total scattering from the unit cell is merely a summation of all molecular unit cell scattering contributions in the crystal. Mathematically, this results in Eq. 1.3 being generalised to Eq. 1.6 through the application of the Laue equations (Eq. 1.4) to express the scattering vector $\boldsymbol{Sr}_j$ as Miller indices of the reflection planes $\boldsymbol{hx}_j$.

$$F_h = \sum_{j=1}^{atoms} f_{s,j}^0 \cdot e^{2\pi i \boldsymbol{hx}_j} \tag{1.6}$$

The structure factor equation defines the scattering power from a crystal in a given reciprocal lattice direction $\boldsymbol{h}$. The scattering is enhanced by the number of repeating units of lattice translation vectors $\boldsymbol{a}$, $\boldsymbol{b}$ and $\boldsymbol{c}$, and thus the overall scattering power is proportional to the number of unit cells in the crystal.

It should be noted that Eq. 1.6 is a simplification of the problem at hand. In reality, instrument and experimental corrections need to be applied to the structure factor equation. A correction factor for each experiment-dependent parameter needs to be applied to the structure factor equation. However, in the scope of this work the details of such correction factors do not need to be discussed.

$$\rho(x,y,z) = \frac{1}{V}\sum_{h=0}^{+\infty}\sum_{k=-\infty}^{+\infty}\sum_{l=-\infty}^{+\infty} \boldsymbol{F}(hkl)\cdot e^{-2\pi i(hx+ky+lz)} \tag{1.7}$$

Since complex structure factors describe the molecular structure in the reciprocal space domain, the conversion to the real space domain in form of electron density is required. This can be conveniently done through the bijective Fourier transform, which allows to convert complex structure factors to electron density and vice versa without the loss of any information [13]. Thus, electron density can be obtained from the complex structure factors using Eq. 1.7. The normalisation factor $1/V$ provides the correct units for the electron density $\rho(x,y,z)$.

1.1.2 From crystal to structure

In X-ray crystallographic experiments, X-ray radiation is measured using light detectors. However, the measurement taken is incomplete. Light detectors only capture the intensity of the scattered X-ray photons but crucially lose the phase information. The latter is essential for atomic reconstruction of the molecule in the crystal, and thus needs to be obtained. In Macromolecular Crystallography (MX), experimentalists have a number of alternative techniques to compensate for the lost phase information.

Prior to the big advances in computing power and the successful elucidation of many protein structures, MX crystallographers primarily recovered the lost phase information through Direct Methods or Experimental Phasing [13]. Today, the most popular method to recovering the lost phase information is MR [14, 15]. In a MR search, a known structure ('search model') similar to the unknown is relocated in the unit cell until the solution with the best fit between calculated and observed diffraction data is obtained [13]. A 6-dimensional search, i.e. a simultaneous rotation and translation search, is possible [16–18], however computationally very expensive and less suitable for challenging cases. In comparison, most modern crystalloraphic applications opt for two distinct sub-searches, the rotation search to orient the search model within the unit cell followed by the translation search to locate it [13]. The benefits over a combined search include search-specific target functions that enable increased sensitivity and additional terms to compensate for imperfect data.

The most successful MR algorithms perform the rotation and translation searches using Patterson methods or Maximum Likelihood functions. Patterson methods — originally developed by Rossmann and Blow [19] — rely on the use of a map of vectors between the scattering atoms, which can be determined for the calculated and observed structure factor amplitudes. Patterson vectors can be sub-classed as intra- and inter-molecular vectors. A distinct separation of the observed vectors is impossible. However, inter-molecular vectors appear further away from the central peak of self-vector (vector from atom to itself) in

the Patterson map [13]. The calculated Patterson vectors for the search model allow for a clearer distinction between the intra- and inter-molecular vectors. If the search model is placed in a large unit cell, then inter-molecular vectors must scale with the unit cell dimension [13]. Ultimately, using the intra-molecular Patterson vectors, the search probe can be oriented against the experimentally determined Patterson vectors. Similarly, the inter-molecular vectors can be used to identify the correct translation of the search probe. Patterson methods are very sensitive to small orientation errors of the search probe [13]. Thus, orientations with the highest vector peak overlaps are trialed in the subsequence translation search.

In comparison to the Patterson methods, Maximum Likelihood methods do not rely on inter-atomic vectors in Patterson maps. Instead, Maximum Likelihood methods make use of Bayes' theorem [20] to compare calculated structure factors and observed structure factor amplitudes directly [18]. Bayes' theorem in crystallographic Maximum Likelihood methods is applied to compute the likelihood that an experimental value is observed given the current search model. The maximal likelihood indicates the best search model given the observed experimental data. Since the search model likelihood term is the product of many individual probabilities, which are difficult to represent computationally due to floating point representations, the log of the likelihood is commonly used [13]. The major advantage of Maximum likelihood methods over Patterson methods centres on the more realist target functions, which consider errors and incompleteness of the search model, applies bulk solvent correction and conducts multi-model searches [18]. The latter is of particularl relevance since the Maximum likelihood rotation function can thus consider already placed search model probes in a fixed position whilst trialling additional ones [21], which proves to be a major advantage over Patterson methods. Furthermore, likelihood target functions consider the structural variance of multiple superposed models in an ensemble search model, which is used to weight structure factors at the various positions to improve the overall likelihood term [18].

The initial electron density map after MR is almost always inaccurate because of the search model-based phases. Inaccuracies arise from experimental errors, model incompleteness, low signal-to-noise or model bias. Thus, approaches for improving the phases used to calculated the initial electron density map have been developed and are routinely applied in MX. Density modification describes a set of methods that improve the obtained electron density typically by applying statistical corrections to electron density distributions. These corrections are based on prior knowledge or assumptions of the physical properties of macromolecular structures [13]. This process can transform initially poor or uninterpretable initial electron density maps to high quality ones. Three pre-dominant density modification approaches exist: solvent flattening, histogram matching and the "sphere-of-influence" method. Solvent flattening is an approach first proposed by Wang [22], which exploits the fact that solvent regions in protein crystals are disordered, and thus differ in electron density volume from macromolecule-containing regions. If solvent electron density is set to a constant, then it is essentially flattened which will result in improved

structure factors with improved phases and thus improved electron density. Histogram matching [23] exploits the defined characteristics of an electron density distribution determined from sets of proteins at the same resolution, irrespectivce of individual structural details. The electron density distribution for noisy maps are Gaussian-shaped. In contrast, the electron density distribution of a feature-defined map is positively skewed. The "sphere-of-influence" method was introduced by Sheldrick [24] and classifies solvent and protein electron density by observing its variance across the shell surface of a 2.42Å sphere (dominant 1-3 atom distance in macromolecular structures). If the sphere is positioned in the disordered solvent region typically found in intermolecular channels, the density variance will be low. Thus, this approach allows to smoothen solvent-containing regions of the electron density [24]. Independent of the density modification strategy applied, it is important to understand that improvements to the electron density map anywhere lead to improvements everywhere by transferral of information from one part of the map to another [25].

A second approach to improving the initial electron density is termed Refinement. Iteratively, the placed search model is optimised to better describe the experimentally observed data. This optimisation problem is typically broken down into three main steps: the definition of the model parameters, the scoring function and the optimisation method. The model parameters describe the crystal and its content and can be subdivided into atomic and non-atomic model parameters [26]. These parameters combined are used to score the current model. The scoring function relates the experimental data to the model parameters. The scoring function contains two primary terms, the refinement data target and an *a priori* knowledge term. The former defines a target function that assesses the similarity between calculated and experimental structure factors. The target function is commonly a Maximum Likelihood-based function that considers missing or incomplete data [26, 27]. The *a priori* knowledge term in the scoring function defines the properties of a good model by including stereochemical property terms. Lastly, optimisation methods provide tools to vary the model parameters to better fit the experimental data. Different optimisation techniques can be used depending on the severity of model parameter alteration, which generally depend on the entrapment of states in local energy minima. The three steps combined form a macrocycle that iteratively modifies the model to optimise its fit to the experimental data. This ultimately improves both the electron density map interpretability and model quality. MX refinement can be performed in structure-factor-based reciprocal space and electron-density-based real space [26]. A combination allows global and local refinement strategies and enables grid-like searches to optimise the model parameters until convergence.

Once initial phase information is improved through refinement and density modification, attempts can be made to build atomic model coordinates into the electron density map. This process is typically coupled with refinement or density modification to iteratively improve the quality of the partially built model and the electron density map [13]. A small number of distinct algorithms are currently used to automatically build atomic

coordinates into electron density: main-chain autotracing [28], fitting pseudo-atoms into electron density [29], or fitting reference coordinates with similar electron density maps [30, 31]. In essence, all algorithms attempt to maximise the number of correctly identified and placed atomic coordinates into available electron density. Whilst autotracing solely builds main-chain peptides, the other two approaches rely on sequence information to also build side-chains. Independent of the complexity of the model building task, the higher the resolution and the more complete the initial starting model, the less ambiguous and challenging this overall task becomes [13].

1.1.3 Unconventional Molecular Replacement

The process of macromolecular structure determination via conventional MR has been outlined previously. Search models are typically derived from structural homologs identified by sequence similarity to the crystallised target [13]. However, with decreasing sequence similarity between homologs, it becomes more challenging to identify structural templates suitable for MR. Furthermore, experimental phasing approaches to circumvent the absence of MR templates can be expensive, unsuccessful and very challenging for certain protein targets, and thus remain unfeasable to pursue at times. Under such circumstances, alternative approaches are required, which are referred to as "unconventional" MR approaches from here onwards. The unconventional MR approach most relevant to the work presented in this thesis utilises the 3-dimensional structure prediction of a protein target starting from its sequence [32–34].

1.2 *Ab initio* protein structure prediction

The folding of protein structures is commonly described by the folding funnel hypothesis [35]. It assumes that the native state of a protein fold corresponds to its global minimum free energy state along its energy surface (Fig. 1.2) [36]. *In silico* protein folding experiments attempt to find this lowest-free-energy state of the protein fold; however, to unambiguously identify it sampling of all polypeptide chain conformations is necessary. In theory, sampling of all conformations for a 100-residue protein takes in the order of approximately 10^{52} years (10^{7} configurations with 10^{-11} seconds per configuration), yet in practice an equivalent polypeptide chain would fold in milliseconds to seconds [37, 38]. This paradox — termed the Levinthal paradox [37] — created the basis for the folding funnel hypothesis.

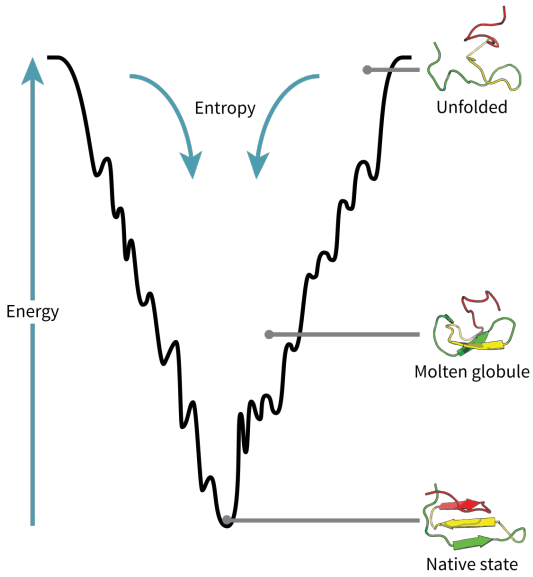

Figure 1.2: Schematic of the folding funnel hypothesis [35]. Diagram produced by Wikipedia [39] contributors.

In *ab initio* protein structure prediction, the tertiary structure of a protein is predicted using its primary structure alone. This problem is in its nature identical to finding the lowest-energy state along the protein's energy landscape. However, in an attempt to avoid the Levinthal paradox, different knowledge- and physics-based energy functions coupled with a variety of conformational-search sampling algorithms are employed [40].

Physics-based energy functions use physiochemical force fields typically coupled with Molecular Dynamics simulations to sample the folding trajectory of a protein sequence (true physics-based approaches are computationally intractable because quantum mechanics models would need to be used). Force fields describe parameter sets used to calculate energy potentials for a system of atoms in a simulation run, and include potentials such as van der Waals and electrostatic interactions [40]. In the context of *ab initio* protein structure prediction, pure physics-based approaches are often less favourable, because the computational complexity to find the lowest free-energy state of a large protein structure remains intractable without the use of supercomputers.

Knowledge-based energy functions rely on empirical energy terms derived from statistics and regularities of experimentally determined structures [40]. These energy terms can be subdivided into two types, the generic or sequence-independent terms and amino-acid or sequence-dependent terms [41]. The former include terms to describe the backbone hydrogen-bonds and local backbone stiffness of a polypeptide chain. The latter describes terms such as pairwise residue contact potential, distance-dependent atomic contact potential, and secondary structure propensities. However, predicting local or global tertiary structure of a protein sequence using empirical energy terms alone is very difficult. Subtle differences in the local and global environment of a primary structure alongside the subtle differences in primary structures leading to common secondary structure features are very

difficult to reproduce in a modelling scenario. Thus, knowledge-based energy functions are often coupled with the assembly of fragments extracted from other protein structures to predict the unknown tertiary structure of the target sequence [40].

The most successful *ab initio* structure prediction protocols use knowledge-based and physics-based energy functions combined with fragment-assembly-based conformational searches to find the lowest free-energy state [42–46]. Structural fragments of varying lengths (typically 3-20 residues) are extracted from existing protein structures [47–54]. These fragments are used in a Monte-Carlo simulation to search the conformational space of the polypeptide chain to search for low free-enery states [55]. The insertion of overlapping fragments results in the replacement of torsion angles either at random positions or sequentially from pre-defined starting position (such as N- or C-termini), and each move is scored against the Metropolis criterion [55] consisting of knowledge-based and physics-based terms. If a fragment passed the Metropolis criterion, its torsion angles are accepted and integrated in the polypeptide chain for the next fragment-insertion iteration. This process is repeated until convergence of the decoy, i.e. no lower free-energy state can be found. In all routines, these steps are independently repeated thousands of times to create a pool of decoys.

In order to identify the correct fold amongst the thousands of generated decoys, clustering approaches are commonly in combination with *ab initio* protocols. Shortle et al. [56] identified that the most-similar decoy to the native structure is most often the centroid (decoy with most neighbours in the cluster) of the largest cluster. Further studies showed that the selection of those centroid decoys helps to identify the most native-like folds amongst the many thousands generated [57–59]. Some protocols use clustering as an intermediate or final step to identify decoys for which it will perform more computationally demanding all-atom refinement [58] or other decoy hybridisation [43, 60, 61] approaches to further approach the native-like fold [62].

Despite active research in *ab initio* protein structure prediction over decades, all approaches cannot reliable predict high-resolution structures for anything but small globular folds [58, 63–65]. The major issue arises from the sampling of the conformation space since incorrect local changes influence the global structure. Furthermore, β-sheets are inheritely difficult to predict given that β-strands in fragment-based approaches are inserted one at a time yet rely on the hydrogen bond network typically found in β-sheets to reduce the overall energy of the decoy. To address this issue, Lange et al. [66], Raman et al. [67], and Göbl et al. [68] started to use Nuclear Overhauser Effect (NOE) data as residue-residue distance restraints to reduce the sampling space of conformations, which enabled high-resolution prediction of tertiary structure for longer protein peptides. Nevertheless, only the use of residue-residue contact information as proxy for spatial proximity of amino acid pairs enabled accurate *ab initio* structure prediction for longer polypeptide chains (e.g., [45, 46, 69–75]).

1.3 Residue-residue contact prediction

The use of residue-residue contact information to reduce the conformational search space in protein structure prediction relies on the identification of amino acids in close spatial proximity. Today, such identification can be detected from sequence information alone by either Direct Coupling Analysis (DCA) or Supervised Machine Learning (SML) algorithms.

1.3.1 Direct Coupling Analysis

Direct Coupling Analysis relies on the use of protein sequence information to identify coordinated changes of amino acids in sequences of a protein family (Fig. 1.3). These coordinated changes are caused by evolutionary pressure to maintain residue interactions important for protein structure and function. However, original attempts to detect covariation signal from sequences in a protein family were unsuccessful for many years [76–79]. The applied (local) statistical model suffered from numerous drawbacks, including the loss of covariation signal due to phylogenetic dependencies, limited availability of sequence data, and the potentially false assumption that truly coevolved residues are in close proximity [80–82]. Implementations of the local statistical model used raw covariation frequencies between pairs of positions in the sequence alignment. This further poses issues since successful distinction between "direct" casual (A-B and B-C) and "indirect" transitive (A-C) correlations is essential for successful protein structure prediction.

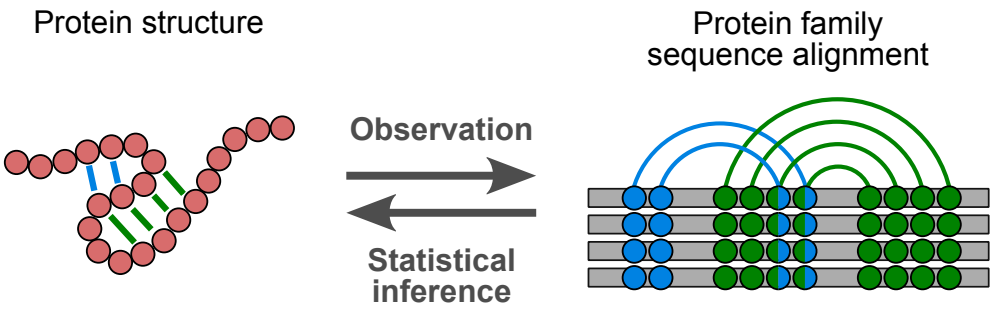

Figure 1.3: Schematic of inference of covariance signal originating from evolutionary pressure in protein tertiary structures and encoded in its family's sequence alignment (adapted from [83]).

Lapedes et al. [81] proposed the use of a global statistical model to infer correlations of residue pairs to circument the main problem of decoupling causal and transitive correlations. However, it was not until a decade later before first implementations of the global statistical model surfaced to successfully disentangle these types of correlations [69, 84–

91]. Global statistical models achieve successul disentanglement by inferring a probabilistic description of the sequence alignment that best explains observed correlations using underlying causal couplings between positions [92]. Such couplings can be inferred by maximising the likelihood of observing the sequences in the alignment under the maximum entropy probability model. In other words, by considering all amino acid pair positions simultaneously, causal and transitive couplings can be successfully disentangled [89].

The pairwise probabilistic model $P(\boldsymbol{\sigma})$ of the amino acid sequence $\boldsymbol{\sigma} = (\sigma_1, \sigma_2, \ldots, \sigma_N)$ of length N is defined in Eq. 1.8, which contains the amino acid configuration constraints σ_i and σ_j at positions i and j, the single-site conservation bias term h_i, and co-conservation term J_{ij} between position pairs i, j.

$$P(\boldsymbol{\sigma}) = \frac{1}{Z} \exp\left(\sum_{i=1}^{N} h_i(\sigma_i) + \sum_{1 \leqslant i < j \leqslant N} J_{ij}(\sigma_i, \sigma_j)\right) \tag{1.8}$$

The partition function Z (Eq. 1.9) acts as normalising constant, and additionally has the property to maximise the entropy in the probabilistic model. However, the computation of Z is intractable for the feature space found in DCA since the number of summations in Z exponentially increases with N for all 20 amino acid configurations. Thus, approximations of Z are typically used, which were shown lead to precise covariance predictions [89].

$$Z = \sum_{\boldsymbol{\sigma}} \exp\left(\sum_{i=1}^{N} h_i(\sigma_i) + \sum_{1 \leqslant i < j \leqslant N} J_{ij}(\sigma_i, \sigma_j)\right) \tag{1.9}$$

Over the last decade, numerous approximations for the parameter inference of $P(\boldsymbol{\sigma})$ have been implemented, which include gradient ascent with Monte Carlo sampling [82], message passing [84], mean-field [69, 87, 88, 93], and pseudolikelihood maximisation [86, 89–91, 94]. However, it is the latter that has proven to be most successful, and thus it is commonly used in most applications. In pseudolikehood maximisation DCA approaches, the full likelihood for each sequence position i in $\boldsymbol{\sigma}$ across all sequences in the alignment is approximated by a product of conditional likelihoods (Eq. 1.10) [92].

$$\mathcal{L}(\mathbf{h}, \mathbf{J}) = \prod_{\sigma \in \Sigma} P(\sigma | \mathbf{h}, \mathbf{J}) \approx \prod_{i=1}^{N} P(\sigma_i | \sigma \backslash \sigma_i, \mathbf{h}, \mathbf{J}) \tag{1.10}$$

Equation 1.10 describes the conditional probability of observing amino acid (σ_i) in position i given all other amino acids $(\sigma \backslash \sigma_i)$ in $\boldsymbol{\sigma}$. This leads to the cancellation of the partition function Z, and instead normalises locally over all possible 20 amino acid

configurations at each site i. The parameters $\mathbf{h}$ and $\mathbf{J}$, which minimise Eq. 1.10, are identified using iterative optimisation algorithms [92]. Typically, regularisation terms are also added to Eq. 1.10 to avoid overfitting of the input data [92].

The positional constraint matrices J_{ij} for all amino acid (k) pairs across all combinations of σ_i and σ_j in $\boldsymbol{\sigma}$ need be summarised to a coupling score between σ_i and σ_j. The Frobenius norm is the preferred summary statistic (Eq. 1.12), and applied to a row- and column-means-centered coupling matrix J'_{ij} (Eq. 1.11). Furthermore, Average Product Correction (APC) is applied to remove background coupling that arises due to noise from phylogentic relationships between sequences to provide the final evolutionary coupling Evolutionary Coupling (EC) score (Eq. 1.13) [88–91, 95].

$$J'_{ij} = J_{ij}(k,l) - J_{ij}(\cdot,l) - J_{ij}(k,\cdot) + J_{ij}(\cdot,\cdot) \tag{1.11}$$

$$FN(i,j) = \sqrt{\sum_k \sum_l J'_{ij}(k,l)^2} \tag{1.12}$$

$$EC(i,j) = FN(i,j) - \frac{FN(i,\cdot)FN(\cdot,j)}{FN(\cdot,\cdot)} \tag{1.13}$$

Despite the great precision achievable by DCA algorithms, such algorithms suffer from one major drawback. All covariance-based algorithms rely on sufficiently large and diverse Multiple Sequence Alignment (MSA)s. Although the minimum number of sequences required per MSA might be target- and algorithm-dependent, early works suggested a minimum required of > 1000 sequence homologs [88, 96, 97]. Simultaneously, Marks et al. [69] and Kamisetty et al. [90] recommended a more sequence-specific length-dependent factor, whereby the sequence count in the alignment should exceed at least five times protein length for precise predictions. Whilst those earlier suggestions permit crude estimations of the likelihood of obtaining precise contact predictions, researchers realised that highly redundant MSAs could surpass such a threshold yet not provide enough diversity typically required for covariance-signal detection. Thus, the measure of *alignment depth* (also termed *number of effective sequences*) was introduced to capture both the sequence count and diversity in a given alignment [87, 98–100]. Although target- and algorithm-dependent threshold persist, a minimum of 100-200 effective sequences are typically required [99, 100]. Furthermore, individual sequence weights used to calculate the alignment depth are widely used in covariance-based algorithms to reweight individual sequences to reduce the phylogenetic effect of non-independently evolved sequences in the MSA [89].

1.3.2 Supervised Machine Learning

Unlike DCA approaches, Supervised Machine Learning algorithms do not rely on the availability of homologous sequences to predict residue-residue contacts. Instead, SML models are trained on a variety of sequence-dependent and sequence-independent features to infer contacting residue pairs [101–106]. Broadly speaking, such SML algorithms rely on the analysis of sequence-based features, such as secondary structure, and sequence profiles. SML algorithms suffer from a similar inability to distinguish between residue pairs that form direct and indirect contact pairs, similar to earlier implementations of covariance-based methods. However, pure SML-based algorithms are not relevant to the work described in this thesis, and thus not further discussed. It is worth noting though that covariance-based algorithms outperform pure SML algorithms for protein families with many homologous sequences. However, SML algorithms do outperform DCA algorithms for families with fewer homologous sequences [99, 106, 107].

1.3.3 Contact metapredictors

The most recent approaches in residue-residue contact prediction use combinatorial approaches to exploit information from DCA and SML approaches. Metapredictors commonly use SML approaches as priors [71] or posteriors [75, 99, 100, 108–110] in addition to DCA algorithms. Furthermore, metapredictors use multiple input MSAs and/or DCA algorithms to further enhance the prediction precision. In most cases, metapredictors outperform their individual approaches and improvements are most noticable for targets with lower alignment depths [75, 111, 112].

1.4 AMPLE

The major challenge in unconventional MR is to reliably identify local or global folds from existing structures to derive phase information complementary to the experimentally determined structure factor amiplitudes. The ensemble search model preparation pipeline AMPLE (Ab initio Modelling of Proteins for moLEcular replacement) — based on the work of Rigden et al. [33] — attempts to tackle this challenge by utelising structural information from a variety of sources, such as *ab initio* structure predictions [113–117], Nuclear Magnetic Resonance (NMR) ensembles [118], and single [119] or multiple distant homologs [120, 121].

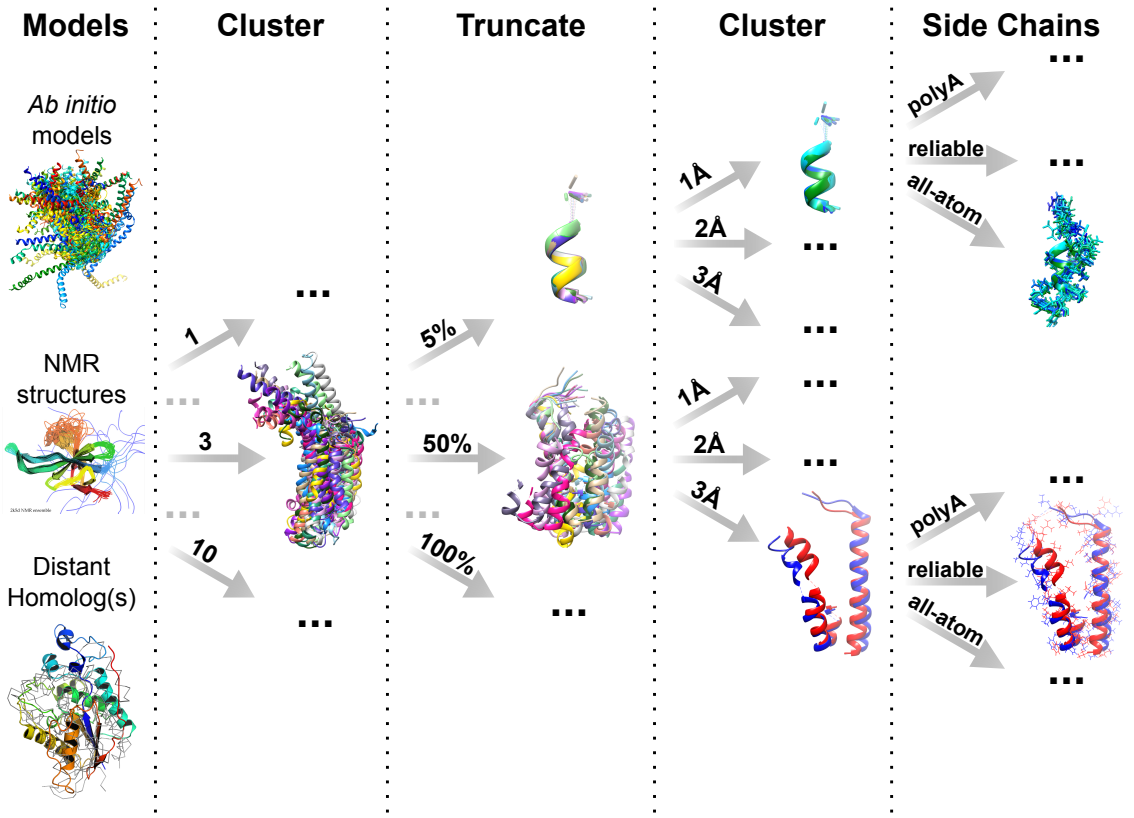

Figure 1.4: Cluster-and-truncate approach employed by AMPLE.

AMPLE attempts to identify a conserved core amongst the initial starting structures. The idea is simple, if a conserved core is present amongst a set of many structures, the likelihood of its presence in the unknown target is high. AMPLE attempts to identify such a conserved core by employing a cluster-and-truncate approach (Fig. 1.4) [113]. The latter can be separated into three main parts: (i) clustering of starting models to identify subsets of similar folds, (ii) incremental truncation of each cluster by its structural variance, and (iii) sub-clustering of each truncated set of models to further identify sub-groups.

Ultimately, this leads to the unbiased generation of a large number of ensemble search models. These ensemble search models cover a great diversity of its original structural information, and hopefully capture in one or more the conserved core necessary for successful structure solution.

Beyond the generation of ensemble search models for MR, AMPLE also integrates the automated MR pipeline MRBUMP [122]. In AMPLE, MRBUMP's structure determination features are of particular interest. It employs PHASER [123] and MOLREP [124] for MR, refines the MR solutions with REFMAC5 [27], uses SHELXE for density modification and main-chain tracing [125], and attempts automated model building with ARP/wARP [126] and BUCCANEER [31]. These features enable the sampling of each AMPLE-generated ensembl for its suitability as MR search model.

Chapter 2

Materials & Methods

2.1 Selection of datasets

2.1.1 ORIGINAL dataset

A test set of 21 globular protein targets was manually selected to include a range of chain lengths, fold architectures, X-ray diffraction data resolutions and MSA depths for contact prediction (Table 2.1). The test set covered the three fold classes (α-helical, mixed α-β and β-sheet) and targets were grouped using their DSSP [127] secondary-structure assignment. Target chain lengths fell in the range of [62, 221] residues. Each crystal structure contained one molecule per asymmetric unit and the resolutions of the experimental data was in range from 1.0 to 2.3Å.

2.1.2 PREDICTORS dataset

An unbiased selection of 27 non-redundant protein targets was selected using the following protocol (Table 2.2).

The Pfam v29.0 [148] database was filtered for all protein families with at least one representative structure in the RCSB PDB [12] database. Each representative had to have monomeric protein stoichiometry and its fold classified in the SCOPe v2.05 database [149]. Targets with fold assignments other than "a" (all-α), "b" (all-β), "c" (mixed α+β) or "d" (mixed α/β) were excluded to exclusively focus on regular globular protein folds. Each resulting protein target was screened against the RESTful API of the RCSB PDB (`www.rcsb.org`) webserver to identify targets meeting the following criteria: experimental technique is X-ray crystallography; chain length is $\geq$ 100 residues and $\leq$ 250 residues; resolution is between 1.3 and 2.3Å; structure factor amplitudes are deposited in the Protein Data Bank [12] database; and there is only a single molecule in the asymmetric unit. The resulting protein structures were cross-validated against the Protein Data Bank of Transmembrane Proteins (PDBTM) [150] to exclude any possible matches. Subsequently, one representative entry was randomly selected for each Pfam family.

The final set of 27 non-redundant targets was determined using further target characterisation and grouping of Pfam families. All targets were grouped using three criteria: domain fold, target chain length and alignment depth. The former consisted of the three fold classes all-α, all-β, and mixed α-β (α+β and α/β) and targets were group using the SCOPe assignment. The target chain lengths were obtained from the deposited information via the RESTful API of the RCSB PDB web server and split into three bins, using 150 and 200 residues as bin edges. Furthermore, the alignment depth was calculated for the sequence alignment of each Pfam family and three bins established with bin edges of 100 and 200 sequences. Thus, all targets were classed in three bins for each of the three features.

Table 2.1: Summary of the ORIGINAL dataset.

PDB ID	Molecule	Resolution (Å)	Space Group	Chain ID	Chain Length	Molecules per ASU	Matthew's Coefficient	Solvent Content (%)	Fold	Citation
1a6m	Oxy-myoglobin	1.00	$P2_1$	A	151	1	1.90	36.00	all-α	[128]
1aba	T4 glutaredoxin	1.45	$P2_12_12_1$	A	87	1	2.22	44.62	mixed α/β	[129]
1bdo	Biotinyl domain of acetyl-coenzyme A carboxylase	1.80	$P2_12_12$	A	80	1	2.48	49.00	all-β	[130]
1bkr	Calponin Homology (CH) domain from β-spectrin	1.10	$P2_1$	A	109	1	2.04	39.80	all-α	[131]
1chd	CheB methylesterase domain	1.75	$P3_221$	A	203	1	2.35	47.65	mixed α/β	[132]
1e0s	G-protein Arf6-GDP	2.28	$P6_122$	A	174	1	2.18	37.00	mixed α/β	[133]
1eaz	Phosphoinositol (3,4)-bisphosphate PH domain	1.40	$C222_1$	A	125	1	2.48	48.00	mixed α+β	[134]
1hh8	N-terminal region of P67Phox	1.80	$P3_1$	A	213	1	2.71	45.00	all-α	[135]
1kjl	Galectin-3 domain	1.40	$P2_12_12_1$	A	146	1	2.15	42.68	all-β	[136]
1kw4	Polyhomeotic SAM domain	1.75	$P6_5$	A	89	1	2.25	45.27	all-α	[137]
1lo7	4-hydroxybenzoyl CoA thioesterase	1.50	I222	A	141	1	2.06	40.22	mixed α+β	[138]
1npu	Extracellular domain of murine PD-1	2.00	$P2_12_12_1$	A	117	1	1.67	25.80	all-β	[139]
1pnc	Poplar plastocyanin	1.60	$P2_12_12_1$	A	99	1	1.82	32.48	all-β	[140]
1tjx	Synaptotagmin I C2B domain	1.04	$P3_221$	A	159	1	2.40	48.00	mixed α+β	[141]
1tlv	LicT PRD	1.95	$P3_221$	A	221	1	2.80	50.00	all-α	[142]
2nuz	α-spectrin SH3 domain	1.85	$P2_12_12_1$	A	62	1	2.57	52.16	all-β	
2qyj	Ankyrin	2.05	$P6_1$	A	166	1	2.28	45.99	all-α	[143]
3w56	C2 domain	1.60	I2	A	131	1	2.05	40.10	all-β	[144]
4cl9	N-terminal bromodomain of Brd4	1.40	$P2_12_12_1$	A	127	1	2.21	44.37	all-α	[145]
4u3h	FN3con	1.98	$P4_132$	A	100	1	2.47	50.27	all-β	[146]
4w97	KstR2	1.60	C2	A	200	1	2.75	55.25	all-α	[147]

The final selection of the 27 targets was performed by randomly selecting one target for each feature combination. To ensure even sampling across the three different fold categories, a target function was employed to identify roughly even target characteristics in each group. The alignment depth and chain length were used as metrics, and had to be within ±15 units to the values of the other fold classes. This created two conditions that had to be met for a randomly chosen sample to be accepted.

2.1.3 TRANSMEMBRANE dataset

The selection of this dataset was done by [117]. In summary, 14 non-redundant transmembrane protein targets were selected from the PDBTM [150], with a chain length of < 250 residues and resolution of < 2.5Å. The final selection is summarised in Table 2.3.

2.2 Enhancement of β-sheet restraints

Structure prediction of β-strand containing protein targets *ab initio* is a notoriously challenging task. β-strands, potentially far in sequence space, form a β-sheet in 3-dimensions. Since fragment-assembly algorithms work on the basis of randomly inserting one fragment at the time, the probability of β-strand formation is much lower compared to α-helices.

Recent advances in *ab initio* structure prediction have seen great improvements in structure prediction quality through the use of predicted residue-residue contacts as distance restraints (see Section 1.3). However, only a single approach specifically focused on improvements to the structure prediction of β-sheet formation [188]. To enhance the probability of β-sheet formation in *ab initio* structure prediction, part of this thesis focused on a more general model to enrich restraints between β-strands to attempt better super-secondary quality in the final decoys.

A more general approach, compared to [188] focusing on β-barrel proteins, was developed combining a starting set of contact pairs with a specifically-prepared set obtained from BBCONTACTS [97]. A HHBLITS [189] MSA was constructed using two sequence-search iterations with an E-value cutoff of 10^{-3} against the UniProt20 database [190]. Redundant sequences were removed from the MSA to 90% sequence identity using HHFILTER [189]. Subsequently, the MSA was subjected to CCMPRED [91] for co-evolution based contact prediction. The BBCONTACTS algorithms also requires a secondary-structure prediction, which was obtained using the ADDSS.PL script [189] distributed with the HHSUITE [191]. Both input files were subjected to BBCONTACTS to obtain a final set of β-strand specific contact pairs.

The BBCONTACTS contact pairs were added to a base set of contact pairs usually obtained from a separate (meta-)predictor. The combination of the two sets of contact pairs was done by simple union of the lists; however, if a contact pair was in the inter-

Table 2.2: Summary of the PREDICTORS dataset.

PDB ID	Molecule	Resolution (Å)	Space Group	Chain ID	Chain Length	Molecules per ASU	Matthew's Coefficient	Solvent Content (%)	Fold	Citation
1fcy	Retinoic acid nuclear receptor HRAR	1.30	$P4_12_12$	A	236	1	2.25	45.50	all-α	[151]
1fvg	Peptide methionine sulfoxide reductase	1.60	C121	A	199	1	2.10	41.55	mixed α+β	[152]
1gm4	Cytochrome C3	2.05	$P6_122$	A	107	1	2.48	50.43	all-α	[153]
1gv8	N-II domain of ovotransferrin	1.95	$P3_1$	A	159	1	2.24	45.00	mixed α/β	[154]
1k40	FAT domain of focal adhesion kinase	2.25	C121	A	126	1	2.21	44.40	all-α	[155]
1oee	Hypothetical protein YodA	2.10	C121	A	193	1	2.30	46.20	all-β	[156]
1oz9	Hypothetical protein AQ_1354	1.89	$P4_32_12$	A	150	1	2.76	55.07	mixed α+β	[157]
1q8c	Hypothetical protein MG027	2.00	$P4_1$	A	151	1	2.42	49.25	all-α	[158]
1rlh	Conserved hypothetical protein	1.80	$P6_3$	A	173	1	2.12	41.98	mixed α+β	
1s2x	Cag-Z	1.90	$P2_12_12_1$	A	206	1	2.74	54.70	all-α	[159]
1u61	Putative Ribonuclease III	2.15	$I4_132$	A	138	1	6.50	80.80	all-α	
1zxu	At5g01750 protein	1.70	$P2_12_12_1$	A	217	1	2.50	50.20	mixed α+β	
2eum	Glycolipid transfer protein	2.30	C121	A	209	1	2.25	45.39	all-α	[160]
2ol8	Outer surface protein A	1.90	$P12_11$	O	249	1	2.19	43.87	all-β	[161]
2oqz	Sortase B	1.60	$P12_11$	A	223	1	2.07	40.71	all-β	[162]
2x6u	T-Box transcription factor TBX5	1.90	$P2_12_12_1$	A	203	1	2.20	44.21	all-β	[163]
2y64	Xylanase	1.40	$P2_12_12_1$	A	167	1	2.15	43.00	all-β	[164]
2yjm	TtrD	1.84	C121	A	176	1	2.08	40.80	all-α	[165]
2yq9	2, 3-cyclic-nucleotide 3-phosphodiesterase	1.90	$P2_12_12_1$	A	221	1	2.10	41.70	mixed α+β	[166]
3dju	Protein BTG2	2.26	$P2_12_12_1$	B	122	1	1.98	37.73	mixed α+β	[167]
3g0m	Cysteine desulfuration protein sufE	1.76	$P12_11$	A	141	1	1.88	34.58	mixed α+β	
3qzl	Iron-regulated surface determinant protein A	1.30	$P2_12_12$	A	127	1	2.42	49.12	all-β	[168]
4aaj	N-(5-phosphoribosyl)anthranilate isomerase	1.75	$P6_1$	A	228	1	2.38	48.30	mixed α/β	[169]
4dbb	Amyloid-β A4 precursor protein-binding family A1	1.90	$P4_12_12$	A	162	1	3.25	62.10	all-β	[170]
4e9e	Methyl-CpG-binding domain protein 4	1.90	H3	A	161	1	2.42	49.23	all-α	[171]
4lbj	Galectin-3	1.80	$P2_12_12_1$	A	138	1	2.09	41.01	all-β	[172]
4pgo	Hypothetical protein PF0907	2.30	$P6_522$	A	116	1	3.25	62.10	all-β	[173]

Table 2.3: Summary of the TRANSMEMBRANE dataset.

PDB ID	Molecule	Resolution (Å)	Space Group	Chain ID	Chain Length	Molecules per ASU	Matthew's Coefficient	Solvent Content (%)	Fold	Citation
1gu8	Sensory rhodopsin II	2.27	$C222_1$	A	239	1	2.75	53.00	all-α	[174]
2bhw	Chlorophyll A-B binding protein AB80	2.50	C121	A	232	3	4.10	69.00	all-α	[175]
2evu	Aquaporin aqpM	2.30	I4	A	246	1	3.38	63.57	all-α	[176]
2o9g	Aquaporin Z	1.90	I4	A	234	1	3.34	63.19	all-α	[177]
2wie	ATP synthase C chain	2.13	$P6_322$	A	82	5	3.41	68.00	all-α	[178]
2xov	Rhomboid protease GLPG	1.65	H32	A	181	1	3.50	64.92	all-α	[179]
3gd8	Aquaporin 4	1.80	$P42_12$	A	223	1	2.73	54.97	all-α	[180]
3hap	Bacteriorhodopsin	1.60	$C222_1$	A	249	1	2.73	54.99	all-α	[181]
3ldc	Calcium-gated potassium channel mthK	1.45	$P42_12$	A	82	1	2.48	50.44	all-α	[182]
3ouf	Potassium channel protein	1.55	I2	A	97	2	2.40	48.76	all-α	[183]
3pcv	Leukotriene C4 synthase	1.90	F23	A	156	1	4.91	74.77	all-α	[184]
3rlb	ThiT	2.00	C121	A	192	2	3.89	68.39	all-α	[185]
3u2f	ATP synthase subunit C	2.00	$P4_222$	K	76	5	2.32	46.92	all-α	[186]
4dve	Biotin transporter BioY	2.09	C121	A	198	3	3.27	62.40	all-α	[187]

section, a contact-pair related weight was doubled to allow subsequent modifications of the energy term in distance restraint creation. Furthermore, additional contact pairs were inferred if not present in the base set of contact pairs. The inference worked on the basis that any neighbouring contacts (i.e. $i, j \pm 1$; $i, j \pm 2$; $i \pm 1, j$; $i \pm 2, j$) to contact i, j must be present, and thus any missing were automatically added to the final list. Again, any already present contact pair was assigned double the weight compared to the rest.

2.3 Evaluation of data

This section defines and describes concepts used throughout this thesis to assess and/or validate various data.

2.3.1 Sequence alignment data

2.3.1.1 Seqeuence alignment depth

Co-evolution based residue-residue contact prediction is dependent on an input MSA ideally containing all homolohous sequences found in the queried database. However, the MSA needs a certain level of sequence diversity amongst the homologs to accurately capture the co-evolution signal. The alignment depth — often also referred to as Number of Effective Sequences (M_{eff}) — captures this diversity by computing the number of non-redundant sequences in the MSA.

$$M_{eff} = \sum_{i} \frac{1}{\sum_{j} S_{i,j}} \tag{2.1}$$

Various approaches exist for computing M_{eff} [87, 88, 100] yielding similar results [99]. In this thesis, the approach defined by Morcos et al. [87] is used. Morcos et al. [87] first described the approach by which sequence weights are computed by means of Hamming distances between all possible sequence combinations in the MSA (Eq. 2.1). If a Hamming distance was < 0.2 (sequence identity of 80%), the binary value $S_{i,j}$ was assigned 1 and otherwise a 0. The sum of fractional weights of the similarity of each sequence compared to all others ultimately describes the alignment depth.

2.3.2 Contact prediction data

2.3.2.1 Contact map coverage

The fraction of residues covered by a set of contact pairs (N_{map}) out of the total number of residues in the target sequence ($N_{sequence}$) (Eq. 2.2).

$$Cov = \frac{N_{map}}{N_{sequence}} \tag{2.2}$$

2.3.2.2 Contact map precision

The precision of a set of contact pairs is equivalent to the the proportion of True Positive (TP) contact pairs in the overall set (Eq. 2.3). A contact pair was defined as TP if the equivalent Cβ (Cα in case of Gly) atoms in the native crystal structure were < 8Å apart. The precision value is in range [0, 1], whereby a value of 1 means all contact pairs are TPs.

$$Prec = \frac{TP}{TP - FP} \tag{2.3}$$

If contacts were unmatched between the target sequence and reference structure, they were not taken into account in the calculation of the precision score.

2.3.2.3 Contact map Jaccard index

The Jaccard index quantifies the similarity between two sets of contact pairs. It describes the proportion of contact pairs in the intersection compared to the union between the two sets [112] (Eq. 2.4).

$$J_{x,y} = \frac{|x \cap y|}{|x \cup y|} \tag{2.4}$$

The variables x and y are two sets of contact pairs. $|x \cap y|$ is the number of elements in the intersection of x and y, and the $|x \cup y|$ represents the number of elements in the union of x and y. The Jaccard index falls in the range [0,1], with a value of 1 corresponding to identical sets of contact pairs and 0 to non-identical ones. It is worth noting that only exact matches are considered and the neighbourhood of a single contact ignored.

2.3.2.4 Contact map singleton content

Almost all sliced sets of residue-residue contact pairs contain a fraction of contact pairs not co-localising with others. These contact pairs — referred to as singleton contact pairs from here onwards — typically show a high False Positive (FP) rate and could be considered noise (although sometimes they encode TP contacts in an oligomeric interface). To quantify this fraction, a distance-based clustering analysis was defined to identify singleton contact pairs, and thus describe the level of noise in the prediction, or alternatively how well contact pairs co-localise typically between secondary structure features.

To identify singleton contact pairs in a set of contacts, the neighbourhood of each pair was searched for the presence of other contacts. The search radius was defined by ±2 residues in a 2D-representation of the contact map. If no other contact pair was identified under such constraint, the contact pair was classified as singleton.

2.3.3 Structure prediction data

2.3.3.1 Root Mean Squared Deviatio

The RMSD is a measure to quantify the average atomic distance between two protein structures (Eq. 2.5). The RMSD is sequence-independent, and measures the distance between Cα atoms.

$$RMSD = \sqrt{\frac{1}{n}\sum_{i,j}(x_i - x_j)^2 + (y_i - y_j)^2 + (z_i - z_j)^2} \tag{2.5}$$

2.3.3.2 Template-Modelling score

The Template-Modelling score (TM-score) is a more accurate measure of structure similarity between two protein structures than the RMSD [192]. Unlike the RMSD, the TM-score score assigns a lenght-dependent weight to the distances between atoms, with shorter distances getting assigned stronger weights [192]. The TM-score has widely been accepted as a standard for assessing the similarity between two structures, particularly in the field of *ab initio* structure prediction.

$$TMscore = max\left[\frac{1}{L_{target}}\sum_{i}^{L_{aligned}}\frac{1}{1+\left(\frac{d_i}{d_0}\right)^2}\right] \tag{2.6}$$

d_i describes the distance between the ith pair of residues. The distance scale d_0 to normalise the distances is defined by the equation $1.24\sqrt[3]{L_{target}-15}-1.8$. The TM-score

value falls in the range (0, 1]. A TM-score value of < 0.2 indicates two random unrelated structures, and a value > 0.5 roughly the same fold [193]

2.3.3.3 Long-range contact precision

The long-range contact precision score is computed identically to the precision of sets of contact pairs (Section 2.3.2.2). However, the precision score is computed solely for long-range contacts (> 23 residues sequence separation).

2.3.4 Molecular Replacement data

2.3.4.1 Register-Independent Overlap

The Residue-Independent Overlap (RIO) score [116] is a measure of structural similarity between two protein structures considering the total number of atoms within < 1.5Å. The RIO can be separated into the in- (RIO_{in}) and out-of-register (RIO_{out}) score considering the sequence register between the model and the target. The RIO score is primarily a measure for post-MR search models to assess the placement of search model atoms with respect to the previously solved crystal structure. To avoid the addition of single atoms place correctly purely by chance, the RIO metric requires at least three consecutive Cα atoms to be within th 1.5Å threshold.

2.3.4.2 Structure solution

MR structure solutions were assessed throughout all works presented in this thesis by the Correlation Coefficient (CC) [194] and Average Chain Length (ACL) scores computed by SHELXE. SHELXE performs density modification and main-chain tracing of the refined MR solution [125]. Thorn and Sheldrick [125] highlighted in their work that a CC of $\geq 25\%$ indicates a successful structure solution. Additionally, previous research with AMPLE [116] has shown that an ACL of the trace needs to be ≥ 10 residues.

In most studies in this thesis, additionally to the SHELXE metrics the post-SHELXE auto-built structures needed R values of ≤ 0.45. The R values had to be acquired by at least one of the Buccaneer [31] or ARP/wARP [126] solutions.

Lastly, the PHASER Translation Function Z-score (TFZ) and Log-Likelihood Gain (LLG) metrics were also considered when automatically judging a MR solution. Values of > 8 and > 120 were required, respectively. However, the PHASER metrics do not always indicate a structure solution — particularly for smaller fragments — and thus was not considered an essential metric to pass to be considered a successful solution.

Chapter 3

Evaluation of ROSETTA distance-restraint energy functions on contact-guided *ab initio* structure prediction

3.1 Introduction

The extended tractability of the AMPLE program for globular protein targets through the use of residue-residue contact information to restrain *ab initio* structure prediction has been highlighted in chapter XYZ. However, that study only focused on PCONSC2 as a metapredictor without considering alternatives, and thus served only as a proof-of-principle work for applications of contact information in unconventional MR.

Besides the individual contact prediction algorithms employed by the PCONSC2 protocol, numerous metapredictors have been developed exploiting different combinations of starting alignments and individual contact predictors to identify the strongest correlating pairs for optimal contact prediction [75, 90, 99, 100, 107, 109, 110]. Furthermore, each of those protocols typically includes its own post-prediction algorithms to find a consensus amongst individual predictions and/or further identify patterns characteristic for residue pairings between secondary structure elements in a protein fold. Thus, depending on the overall protocol, the resulting predictions may differ significantly despite the same underlying algorithms to generate starting alignments and to predict residue contact pairs.

Furthermore, the precision of contact predictions used as distance restraints in *ab initio* structure prediction improves the accuracy of the folding process significantly. However, a diversity of structure prediction protocols, whether fragment-based or not, have been applied and each with a unique integration of contact information as distance restraints [69–71, 100, 195, 196]. Such divergence results in three major problems: (1) researchers cannot directly compare results, and thus have to test each protocol against their own with every newly published approach; (2) novice users might find it difficult to make appropriate decisions given the diversity of algorithms and lack of comparative studies; and (3) users only interested in the information encoded in predicted contact pairs are at risk of picking the most readily available approach over the most accurate for their problem.

Thus, the work presented in this chapter was aimed at extensively comparing state-of-the-art contact- and structure-prediction protocols with a focus on the use of such decoys for AMPLE users.

3.2 Methods

3.2.1 Target selection

This study was conducted using 18 out of 27 targets from the PREDICTORS dataset (Section 2.1.2). The nine targets with alignment depths of < 100 in the Pfam MSA were excluded.

3.2.2 Covariance-based contact prediction

Residue contacts for each target sequence were predicted using three different metapredictors, namely METAPSICOV [100], GREMLIN [90], and PCONSC2 [99]. Online servers for METAPSICOV (`http://bioinf.cs.ucl.ac.uk/METAPSICOV`) and GREMLIN (`http://gremlin.bakerlab.org`) were used to predict two sets of contact pairs. The choice of online servers over local installations was justified to directly imitate most AMPLE users. Both servers were used with default settings.

The GREMLIN web server returns the raw contact prediction files as well as preformatted ROSETTA distance restraints. The raw contact prediction files were downloaded to allow different contact selection thresholds as well as local conversion into ROSETTA restraints files. The METAPSICOV web server returned two contact prediction files, one after Stage 1 and another after Stage 2 post-prediction processing. In this study, contact predictions after Stage 1 (referred to as METAPSICOV from here onwards) were chosen. The PCONSC2 contact prediction set was obtained using a local installation of PCONSC2 due to downtime of the web server at the time of this study. Additionally to the three main contact predictions outlined above, a set of BBCONTACTS restraints was obtained for protein targets containing β-strands. The approach was identical to that outlined in Chapter XYZ.

The sequence-database versions of all three metapredictors, whether on- or offline, were identical to those used in Chapter XYZ.

3.2.3 Contact pair to ROSETTA distance restraint formatting

Contact restraints for *ab initio* protein structure prediction were generated by selecting the top-ranking contact pairs from each prediction and reformatting them into a ROSETTA-readable format. The number of top-ranking contact pairs varied according to the two energy functions used (FADE cutoff: L; SIGMOID cutoff: $3L/2$; where L corresponds to the number of residues in the protein chain). Both energy functions are sigmoidal functions and introduced into the ROSETTA folding protocol in the same fashion.

Neither energy function enforces a specified distance between restrained atoms but reward those that meet it. The two energy functions (Fig. 3.1) differ in that the FADE function does not only have an upper but also a lower bound. Based on previous findings [70, 99], the FADE function was set to acknowledge a formed restraint if the participating Cβ atoms (Cα in case of Gly) were within 9Å. In comparison, the SIGMOID function was defined with amino acid specific distances for Cβ atoms (Cα in case of Gly) to recognise the different sizes of each amino acid [71, 90].

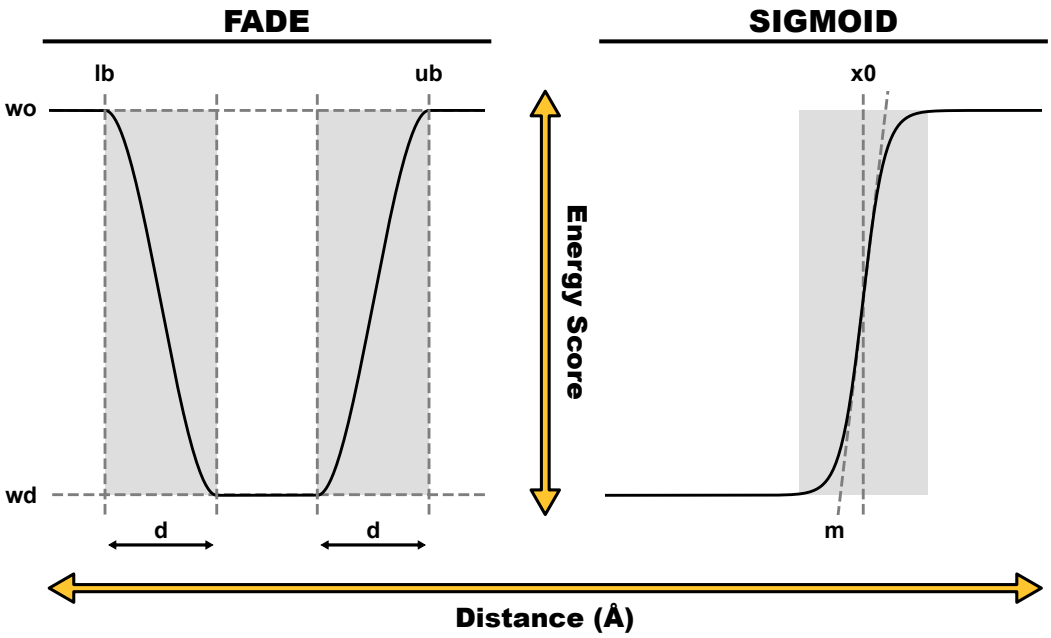

Figure 3.1: ROSETTA energy function comparison. Abbreviations corresponds to input parameters.

To explore the effects of the varying energy function definitions, we created six lists of contact restraints for each α-helical target and nine lists for each β-structure containing one. The top-ranking contact pairs per prediction were converted using the PCONSFOLD definition of the FADE function [70], the GREMLIN definition of the SIGMOID function [71], and additionally the PCONSC2 BBCONTACTS definition of the FADE function for β-structure containing targets (see Chapter XYZ).

The conversion was handled in AMPLE (see Chapter XYZ) and invoked with the keywords outlined in Table 3.1. The `-restraints_factor` keyword defines the factor used to select contact pairs based on the target chain length, i.e. a factor of `1.5` would correspond to $3L/2$ contact pairs. The `-distance_to_neighbour` keyword defines the minimum distance in sequence space between contact pair participating residues, which were set to `5` residues for the FADE function [70] and `3` for the SIGMOID function [71]. Additionally, all distance restraints were given an additional weight when introduced via the SIGMOID energy function to balance its energy term with all remaining terms in the ROSETTA scoring function (Sergey Ovchinnikov, personal communication). This was achieved by using the `-restraints_weight` keyword and weights of `1.0` and `3.0` for the FADE and SIGMOID energy functions.

The addition of BBCONTACTS to existing sets of contacts was achieved with the FADE function in an identical manner as described in Chapter XYZ. In comparison, the SCALARWEIGHTED term in the GREMLIN implementation of the SIGMOID energy function [71] was multiplied by the number of occurrences of each contact pair in the combined map.

Table 3.1: Summary of AMPLE keyword arguments for FADE and SIGMOID ROSETTA energy functions.

Energy Function	**AMPLE keywords**
FADE	-contact_file <FILENAME> -contact_format <FORMAT> -energy_function FADE -restraints_factor 1.0 -distance_to_neighbour 5 -restraints_weight 1.0
FADE (BBCONTACTS)	-contact_file <FILENAME> -contact_format <FORMAT> -energy_function FADE -restraints_factor 1.0 -distance_to_neighbour 5 -restraints_weight 1.0
SIGMOID	-contact_file <FILENAME> -contact_format <FORMAT> -energy_function SIGMOID -restraints_factor 1.5 -distance_to_neighbour 3 -restraints_weight 3.0
SIGMOID (BBCONTACTS)	-contact_file <FILENAME> -contact_format <FORMAT> -energy_function SIGMOID_bbcontacts -restraints_factor 1.5 -distance_to_neighbour 3 -restraints_weight 3.0

3.2.4 *Ab initio* structure prediction

Six or nine individual lists of contact restraints generated for each target were used in separate ROSETTA *ab initio* protein structure prediction runs. Additionally, protein structures were predicted without any contact restraints to acquire a control set of decoys. Homologous fragments were excluded during fragment library generation to imitate the folding process of a target with unknown fold. Fragment libraries were generated once per target and used throughout. In total, 1,000 *ab initio* decoys were generated per run using ROSETTAs default settings [42] and one of the seven contact conditions described previously. In total, 162 sets of models were generated across 18 protein targets.

3.2.5 Molecular Replacement

Besides considering model quality, one key interest of this study was the assessment of the model sets created in the previous step as *ab initio* MR search model templates. To reduce the enormous computational cost linked to trialling 162 sets of models, 108 sets were chosen from the following conditions: simple Rosetta, PCONSC2 prediction and FADE function, GREMLIN prediction and SIGMOID function, METAPSICOV prediction and FADE function, and where applicable, PCONSC2 BBCONTACTS, GREMLIN BBCONTACTS and METAPSICOV STAGE 1 BBCONTACTS predictions and FADE function. Overall, this resulted in four MR runs for the six α-helical targets, seven runs for the six all-β, and seven runs for the six mixed α-β targets. The resulting 108 model sets were trialled in AMPLE v1.1.0. Structure solution success was assessed as described in Section 2.3.4.2.

3.3 Results

3.3.1 Direct comparison of three contact metapredictors

In this study, a direct comparison between three metapredictors — GREMLIN, METAPSICOV and PCONSC2 — was carried out. Residue-residue contact pairs were predicted for 18 protein target sequences with a range of chain lengths and numbers of effective sequences in their Pfam MSAs.

METAPSICOV is the most precise contact predictor across the protein target dataset in this study (Fig. 3.2). The difference between the three metapredictors is most evident in the highest-scoring contact pairs ($L/10$). The median precision values for METAPSICOV and PCONSC2 contact predictions are above 50% up to L contact pairs. GREMLIN, in comparison, predicts contacts with a median precision score at least 20% worse than that of METAPSICOV and 15% worse than PCONSC2. However, at $3L/2$ contact pairs the median precision scores are much more similar across the three different metapredictors: METAPSICOV and PCONSC2 are near identical, and GREMLIN is at most 12% worse compared to the other two. Inspecting the mean precision scores over a continuous range of selection cutoff values illustrates further the difference between METAPSICOV, PCONSC2 and GREMLIN (Fig 3.3). The former two similarly high precision scores compared to the average precision scores for GREMLIN, which are 0.2 precision score units lower. Added to the difference in precision scores is the difference in sequence coverage (Fig. 3.3). Although producing the on-average worst contact predictions out of the three metapredictors used in this study, GREMLIN contact predictions have the highest sequence coverage. However, an analysis of singleton contact pairs, usually with high degrees of false positives, revealed a positive correlation ($\rho_{Pearson} = 0.47$; $p < 0.001$) between the fraction of singleton contact pairs and sequence coverage and hints to a weak negative

correlation ($\rho_{Pearson} = -0.27$; $p < 0.05$) between the fraction of singleton contact pairs and contact precision (Fig. 3.4).

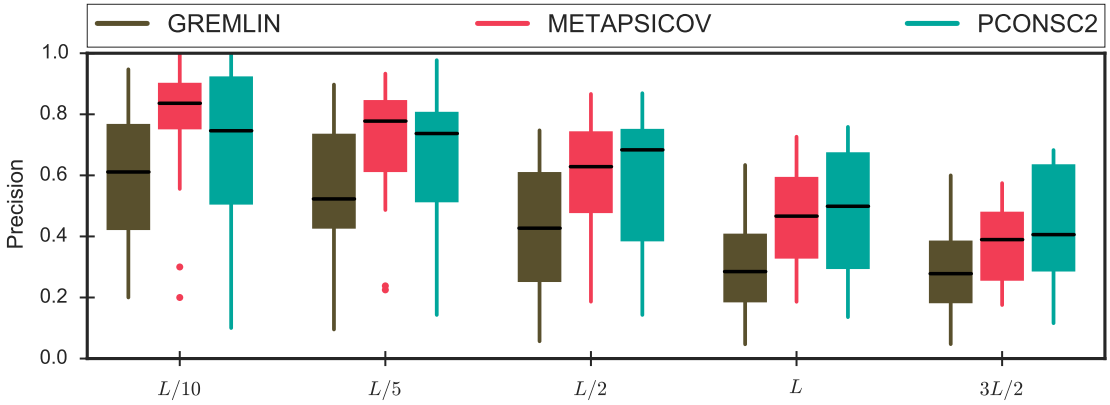

Figure 3.2: Precision spread for three metapredictors computed at five contact selection cutoff values relative to the target chain length (L).

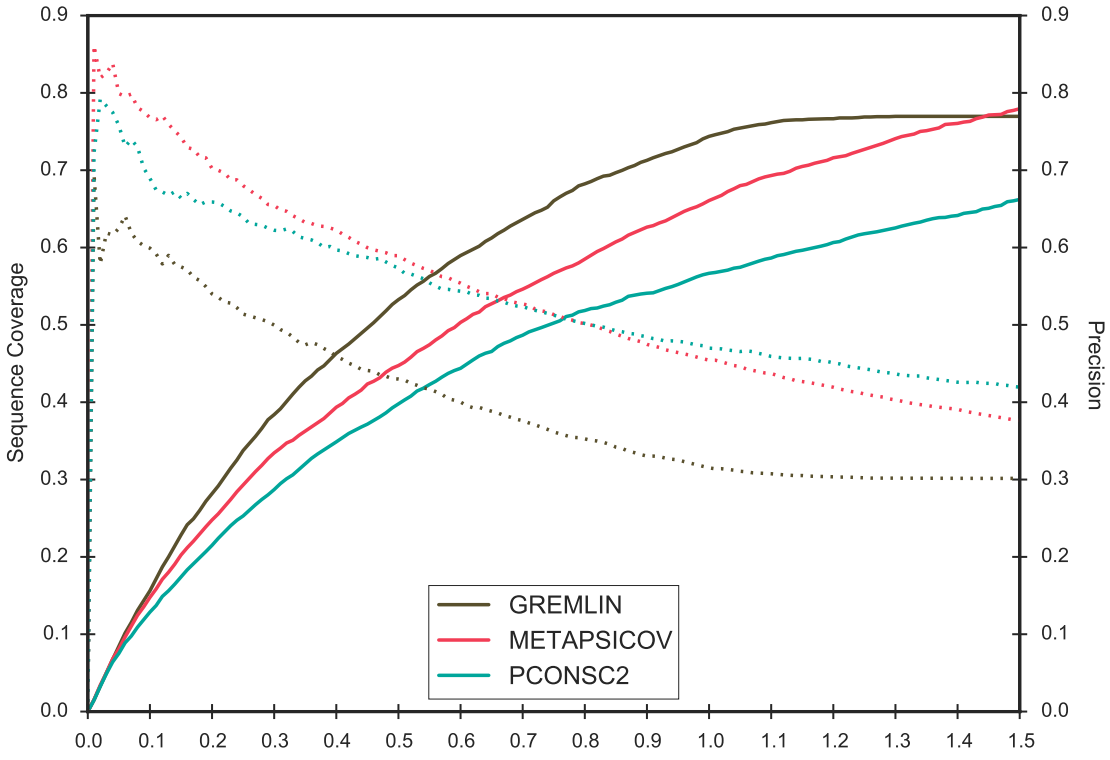

Figure 3.3: Average sequence coverage (line) and contact prediction precision scores (dashed) across a continuous range of contact selection cutoffs ranging from $[0.0, 1.5]$ for all targets.

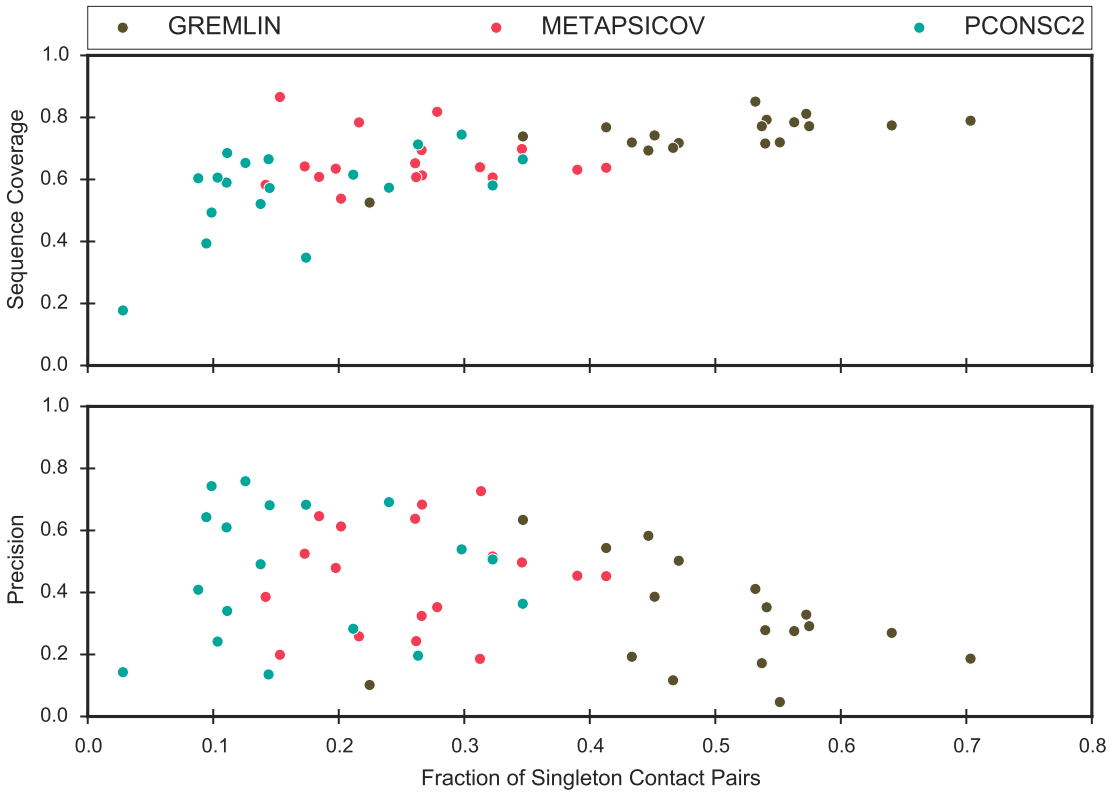

Figure 3.4: Contact singleton analysis compared against the precision of L contact pair lists for three metapredictors.

Given that the overall precision of contact pairs predicted by the three metapredictors differs, it is important to understand where the difference originates. To investigate this, a comparison of the precision values at different cutoff levels on a per-target basis was performed. For the majority of targets the precision scores are very similar across the three metapredictors (Fig. 3.5). However, the prediction precision of some targets differs significantly. For example, the METAPSICOV prediction for the human retinoic acid nuclear receptor HRAR (PDB: 1fcy) contains high precision in its highest scoring (top-$L/10$) contact pairs (Fig. 3.5). In comparison, GREMLIN and PCONSC2 predictions for the same target contain less precise contact pairs ($\Delta Precision_{METAPSICOV-GREMLIN} L/10 = -0.522$; $\Delta Precision_{METAPSICOV-PCONSC2} L/10 = -0.435$). However, the addition of further contact pairs up to $3L/2$ results in near-identical precision across the three metapredictors for this target. A second example illustrating such a difference are the contact predictions for the human galectin-3 CRD sequence (PDB: 4lbj). In contrast to the previous example, the data shows high precision scores for the METAPSICOV and PCONSC2 predictions for this target, yet low precision for the top GREMLIN contact pairs ($\Delta Precision_{METAPSICOV-GREMLIN} L/10 = -0.231$; $\Delta Precision_{METAPSICOV-PCONSC2} L/10 = +0.077$).

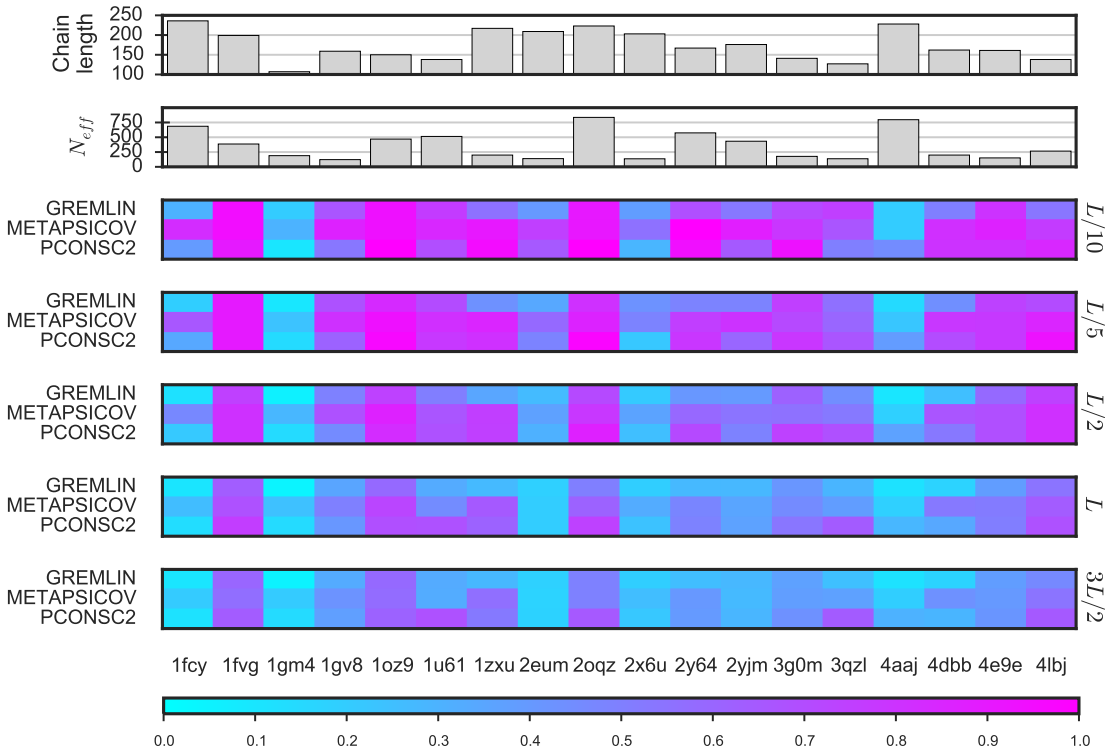

Figure 3.5: Contact prediction precision scores from three metapredictors for 18 targets at different contact pair selection thresholds. The Pfam alignment depth is given by means of number of effective sequences (*Neff*). The color scale corresponds to the precision in $[0, 1]$.

The data presented in Fig. 3.5 also indicates that there is no direct link between chain length or Neff and the precision of the resulting contact predictions. The N-(5'-phosphoribosyl)anthranilate isomerase sequence (PDB: 4aaj) with a chain length of 228 residues and 750 effective sequences in its Pfam MSA yielded a mean precision at $L/10$ contact pairs of 0.283 (top-L: 0.195) across the three metapredictors. This strongly contrasts with the sequence of sortase B (PDB: 2oqz), which shows similar characteristics yet obtained mean precision at $L/10$ contact pairs of 0.938 (top-L: 0.622).

Although the contact predictions differ in precision, an interesting question rests with the similarity of the predicted contact pairs amongst the sets. Thus, the similarity of contact predictions across the three metapredictors is an important metric to evaluate the most appropriate algorithm for AMPLE users. Using the Jaccard similarity index to evaluate the direct overlap of contact pairs across sets of predictions, the data suggests very little similarity between the contact predictions of the three metapredictors for each target (Fig. 3.6). As with the differences in precision scores at higher cutoff thresholds, the Jaccard index is also lower — indicating less overlap — at higher cutoff thresholds. However, it is worth noting that the Jaccard index only considers identical matches and does not consider the neighbourhood of a contact pair. Thus, the index does not highlight similar regions with contact pairs in both maps.

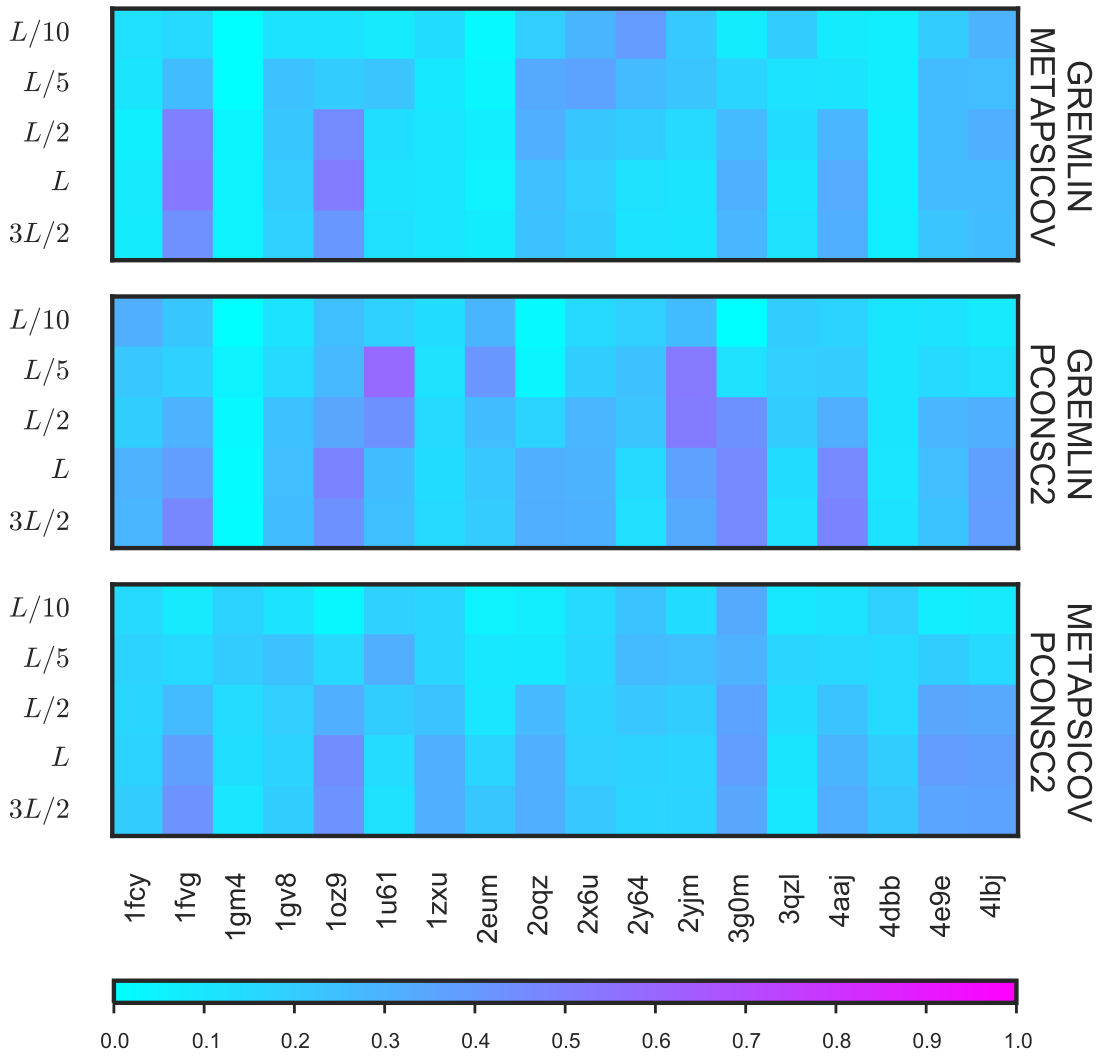

Figure 3.6: Jaccard similarity index illustrates a higher degree of overlap between metapredictor contact predictions with increasing numbers of contact pairs included in the calculation. The three panels show the different comparisons. The color scale corresponds to the Jaccard index in $[0, 1]$.

3.3.2 Protein structure prediction with two ROSETTA energy functions

The accuracy of the starting decoys is a major factor for an AMPLE run to succeed [117]. Thus, the quality of the decoys is of great essence to this study. Given the two different ROSETTA energy functions, FADE and SIGMOID, all contacts predicted were subjected to individual *ab initio* structure prediction runs. Additionally, all contact predictions were enriched with BBCONTACTS for all β-containing targets in separate trials. A total of 234,000 individual decoys were generated in this study through all permutations of targets, contact predictions and ROSETTA energy function combinations.

Separating these individual decoys solely by the ROSETTA energy function (excluding unrestrained ROSETTA decoys) shows that the FADE energy function results in

marginally more accurate decoys (median TM-score FADE: 0.3541; median TM-score SIGMOID: 0.2969). To further investigate which energy function is more suitable for the target dataset used in this study, the decoy sets were grouped by two additional characteristics: the fold of the target, and the source of distance restraints used. The results strongly suggest that the FADE energy function results in more accurate decoy sets (Fig. 3.7), outperforming the SIGMOID energy function by median TM-score in two-thirds of all decoys sets (FADE: 58; SIGMOID: 32). A split of the decoy sets into separate categories by fold and the addition of BBCONTACTS reveals that the SIGMOID energy function only yields similar results for all-β targets in combination with BBCONTACTS-supported distance restraints. Although the total count of decoy sets with higher accuracies between the two energy functions in this category are similar, the actual differences in TM-scores further supports the strength of the FADE energy function compared to the SIGMOID.

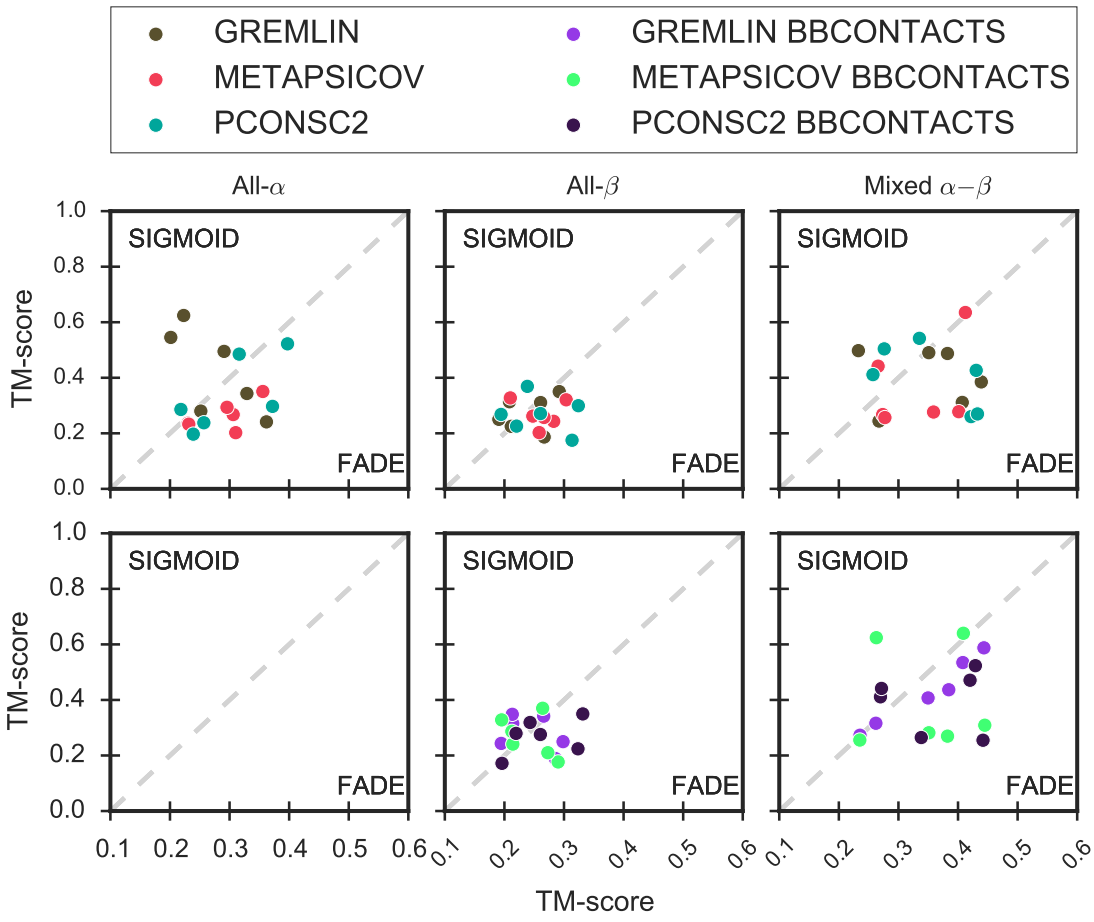

Figure 3.7: Median TM-score comparison of FADE and SIGMOID ROSETTA energy functions differentiated by fold and the addition of BBCONTACTS restraints.

Besides the structure prediction accuracy of each set of decoys, the single, most accurate decoy is also of great interest. If one energy function consistently predicts single decoys more accurately, it might be appropriate to reconsider the structure identification routine (i.e. clustering) in AMPLE for search model preparation. However, a similar difference to that of the decoy quality of entire sets is observed for the top-1 decoy

in each set (Fig. 3.8). The FADE energy function outperforms the SIGMOID function for the majority of target-contact prediction permutations (FADE: 51; SIGMOID: 39). However, the GREMLIN distance restraints in combination with the SIGMOID energy function produce better top-1 decoys than GREMLIN restraints with the FADE energy function. This suggests that GREMLIN restraints and the SIGMOID energy function were tailored to complement each other with the ultimate goal of predicting single decoys to high accuracy over entire sets of decoys. Additionally, the spread of decoy quality differences between the two energy functions widens when only looking at the best decoy in each predicted set ($\Delta MedianTM - score_{ALL} : min = 0.002, max = 0.429$; $\Delta MedianTM - score_{TOP} : min = 0.002, max = 0.456$).

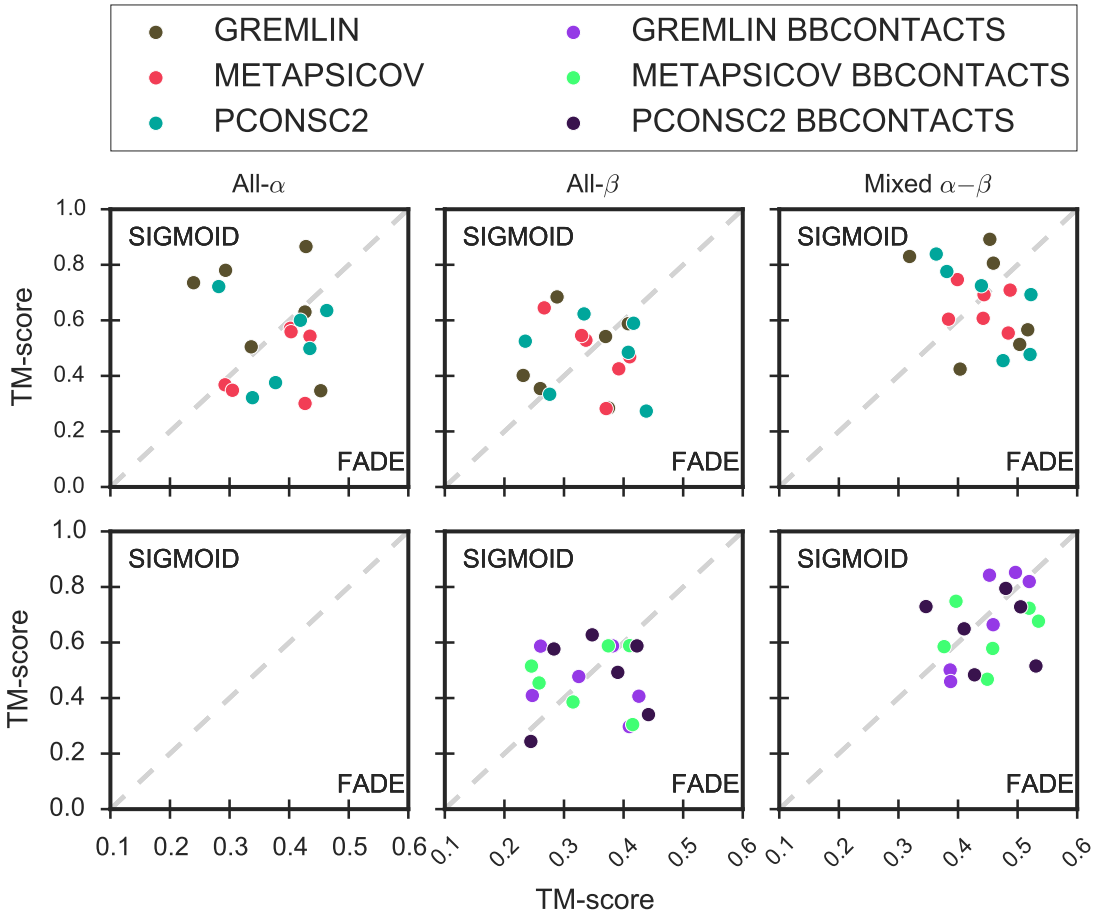

Figure 3.8: Top TM-score comparison of FADE and SIGMOID ROSETTA energy functions differentiated by fold and the addition of BBCONTACTS restraints.

A Kernel Density Estimate (KDE) of TM-scores using each predicted decoy was generated with the TM-scores of individual decoys separated only by fold class and ROSETTA energy function (Fig. 3.9). This density estimate further supports the results presented above: the FADE energy function generates more accurate decoys. However, a very important detail is highlighted by the estimates. Distinct regions with high density are visible in the estimates of the TM-scores of individual decoys for all-α and mixed α-β targets (Fig. 3.9). The bimodal distribution of decoy TM-scores from both energy func-

tions strongly suggests that predicted structures are either native-like or not (based on the TM-score threshold of ≤ 0.5). However, the number of correctly predicted decoys versus incorrectly predicted decoys is in favour of the latter. The decoy sets of all-β targets do not show such distinct regions of high density for decoys with TM-scores < 0.5 units in any of its density estimates (Fig. 3.9). The generally poor decoy quality of decoys predicted without any distance restraint information (ROSETTA) highlights the benefit of contact predictions to *ab initio* protein structure prediction.

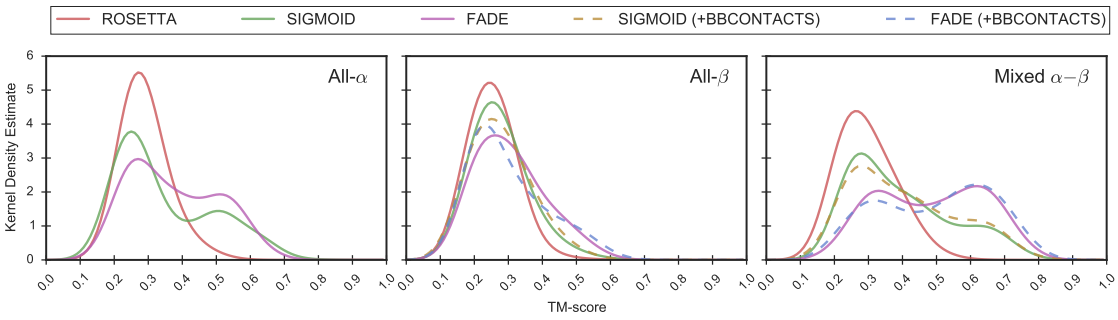

Figure 3.9: TM-score density estimate of all decoys in each respective fold class separating by ROSETTA energy function (SIGMOID or FADE) and no contact information used (ROSETTA). Dashed lines indicate decoys which were predicted with the addition of BBCONTACTS.

A further important aspect of this study is to explore the benefits of adding BBCONTACTS restraints to the structure prediction of β-containing targets. Although previous results (see Chapter XYZ) in combination with those presented above outline overall improvements in decoy quality, it is essential to understand which targets benefit from this treatment. Figure 3.10a highlights the effects of adding BBCONTACTS restraints to the structure prediction strategies employed here. In summary, the addition of BBCONTACTS restraints hardly affects the decoy quality of most targets under the various contact prediction and energy function combinations. Nevertheless, three target, contact prediction and energy function combinations yielded TM-score improvements of at least 0.1 TM-score units compared to the same condition without the addition of BBCONTACTS restraints. In contrast, the addition of BBCONTACTS restraints did not lower the median TM-score by more than 0.1 units for any target (Fig. 3.10b).

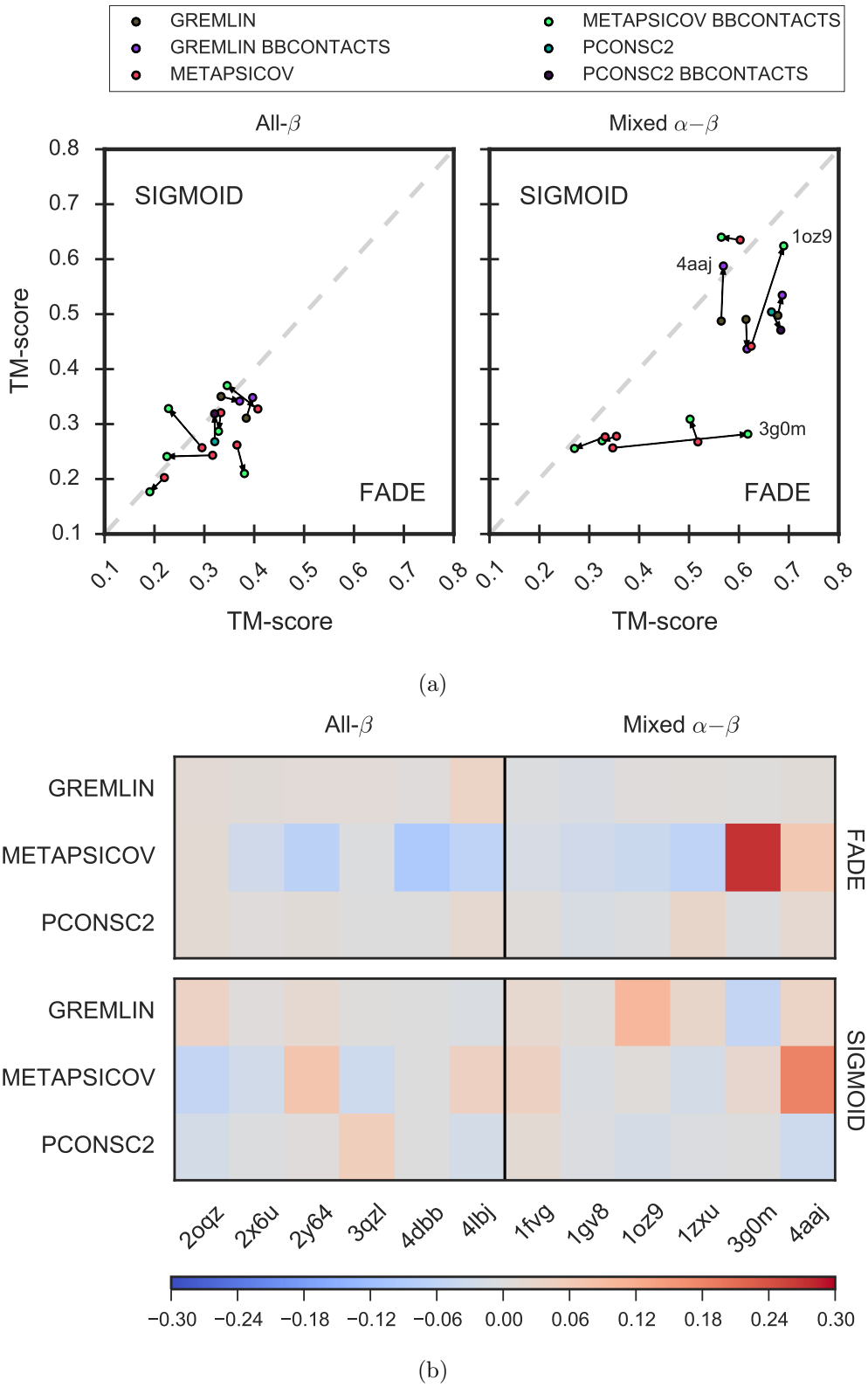

(a)

(b)

Figure 3.10: Median TM-score comparison of FADE and SIGMOID ROSETTA energy functions differentiated by fold (excl. all-α). (a) Arrows indicate the effect on decoy quality through the addition of BBCONTACTS restraints. Targets with a distance < 0.03 TM-score units between normal and BBCONTACTS-added conditions were excluded from the scatter plots. (b) Effect on decoy quality through the addition of BBCONTACTS restraints highlighted by heatmap difference. The color scale corresponds to the difference in median TM-score between normal and BBCONTACTS-added contact maps.

Two further aspects in understanding the differences in effects of the FADE and SIGMOID ROSETTA energy functions on decoy quality are the target chain length and restraints precision. The former appears to affect the final decoy quality of all 1,000 decoys insignificantly (Fig. 3.11). However, the restraint precision results in some differences between the two ROSETTA energy functions (Fig. 3.11). The FADE energy function (L restraints) generally appears to be less sensitive to restraint lists with higher false positive contact pairs. In contrast, the SIGMOID function ($3L/2$ restraints) produces less accurate decoys than the FADE function with more accurate restraints. Most strikingly, the FADE energy function generated decoys with a median TM-score of 0.678 for the N-(5'-phosphoribosyl)anthranilate isomerase domain (PDB: 4aaj) compared to the SIGMOID function with a median TM-score of 0.498. Nevertheless, both energy functions appear to broadly follow a positive linear trend, i.e. better restraint precision results in more accurate decoys.

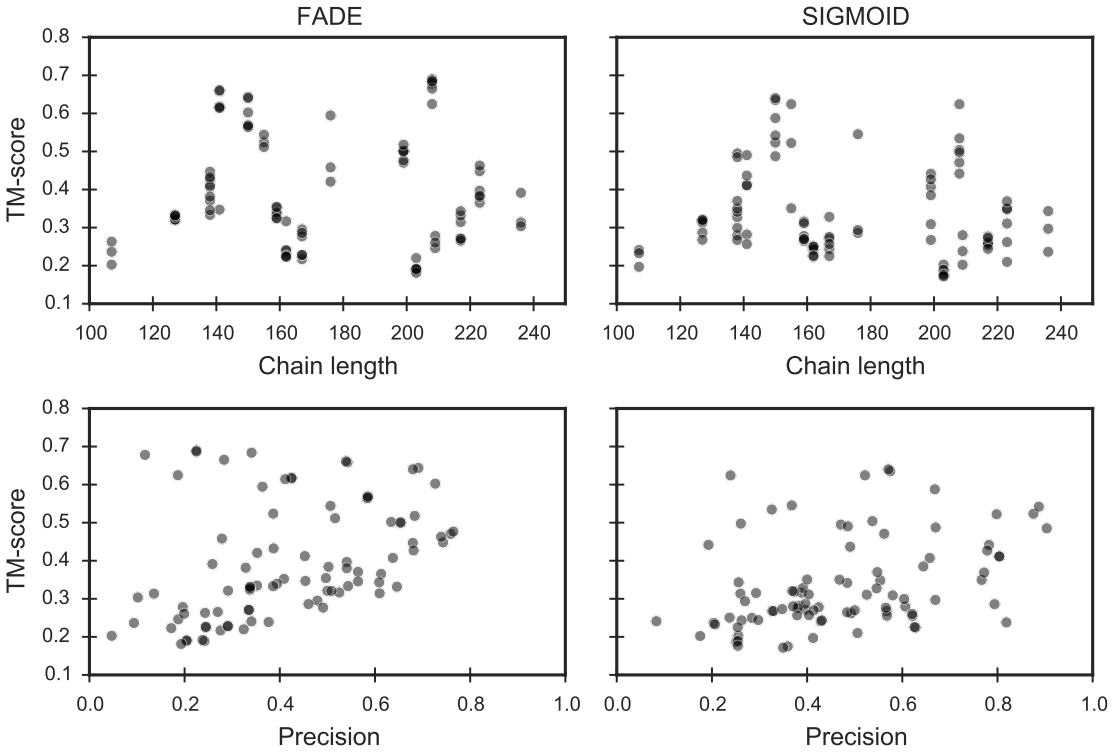

Figure 3.11: Effects of target chain length and restraint precision on the median TM-score for FADE and SIGMOID ROSETTA energy functions. Each scatter point represents a 1,000-decoy set.

3.3.3 Impact of metapredictors and energy functions on unconventional Molecular Replacement

The results obtained from the decoy quality comparison outlined above highlighted differences between the FADE and SIGMOID ROSETTA energy functions. This difference is more pronounced for some targets and less so for others. Thus, the next step in this

study was to analyse the consequences of these differences for unconventional MR using the automated pipeline AMPLE.

Overall, the decoys restrained with GREMLIN distance restraints via the SIGMOID energy function throughout the structure prediction process yielded six out of 18 possible structure solutions (Fig. 3.12). This result was the highest of all trialled conditions and only resulted in one more structure solution compared to unrestrained ROSETTA decoys. All remaining conditions resulted in fewer structure solutions than those from ROSETTA decoys. Furthermore, the conditions METAPSICOV (FADE function), METAPSICOV BBCONTACTS (FADE function) and PCONSC2 BBCONTACTS (FADE function) yielded no more than half of the structure solutions achieved by GREMLIN (SIGMOID function). The remaining two conditions — PCONSC2 (FADE function) and GREMLIN BBCONTACTS (FADE function) — resulted in four out of 18 structure solutions. The addition of BBCONTACTS did not improve decoy quality enough to increase the chances of structure solution success; however, the structure of the bovine peptide methionine sulfoxide reductase (PDB: 1fvg) was only solved with the GREMLIN BBCONTACTS (FADE function) decoys further supporting the small but important value of BBCONTACTS restraint addition to separately determined contact predictions.

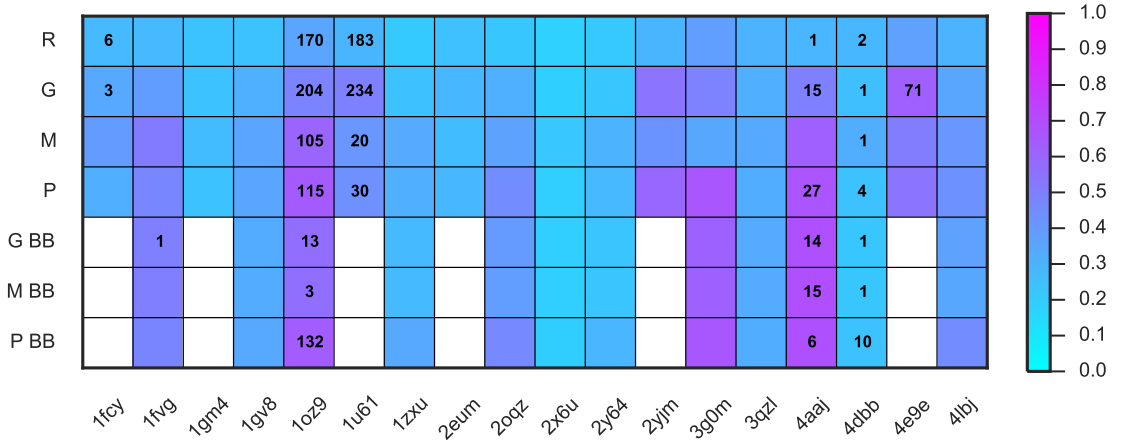

Figure 3.12: Structure solution count for AMPLE search models generated from decoys with varying contact prediction and ROSETTA energy function conditions: unrestrained ROSETTA (R); GREMLIN (G; SIGMOID function); METAPSICOV (M; FADE function); PCONSC2 (P; FADE function); GREMLIN BBCONTACTS (G BB; FADE function); METAPSICOV BBCONTACTS (M BB; FADE function); PCONSC2 BBCONTACTS (P BB; FADE function). The color scale of each square indicates the median TM-score of all 1,000 starting decoys.

The number of structure solutions obtained from the decoy sets subjected to the AMPLE pipeline are somewhat surprising given that ROSETTA decoys result in the second-most structure solutions. These results suggest that the current implementation cannot exploit the true value of more accurate decoy sets. This hypothesis is further supported when considering the decoy set quality and the number of structure solutions (Fig. 3.12).

For example, PCONSC2 (FADE function) decoys predicted for the hypothetical protein AQ_1354 (PDB: 1oz9) yield high accuracy, and thus would generally be considered highly desirable starting structures for the AMPLE protocol; nevertheless, the AMPLE protocol was unable to exploit such highly accurate decoys for successful structure solutions of other targets, e.g. cysteine desulferation protein SufE (PDB: 3g0m; median TM-score PCONSC2 BBCONTACTS (FADE function)=0.661). In comparison, the median TM-scores for all successful ROSETTA decoy sets do not exceed 0.355 TM-score units.

Naturally, one would expect the best decoys to result in the most accurate ensemble search models, which in turn yield the highest number of structure solutions per target. However, here we demonstrate that the most accurate decoys do not guarantee structure solution, and in contrast some poorly predicted decoy sets achieve structure solution. Thus, it is essential to investigate the stage in AMPLE's cluster-and-truncate approach at which the higher decoy quality results in less suitable ensemble search models for MR.

The data generated as part of this study reveals a positive correlation ($\rho_{Spearman} = 0.78$; $p < 0.001$) between the decoy quality and the number of resulting AMPLE ensemble search models (Fig. 3.13). The plotted data alongside a fitted LOWESS function further illustrate that small differences in decoy quality in the lower TM-score regions increases the total number of generated ensemble search models dramatically. However, once the threshold of 0.5 TM-score units [193] is surpassed the number of generated ensemble search models plateaus at around 350-400 ensemble search models, approaching the maximum number of search models generatable by AMPLE. Furthermore, the data suggests that sets containing fewer than 100 ensemble search models do not lead to structure solution, although this result needs to be considered with care given the difficulty of predicting which search model will lead to structure solution.

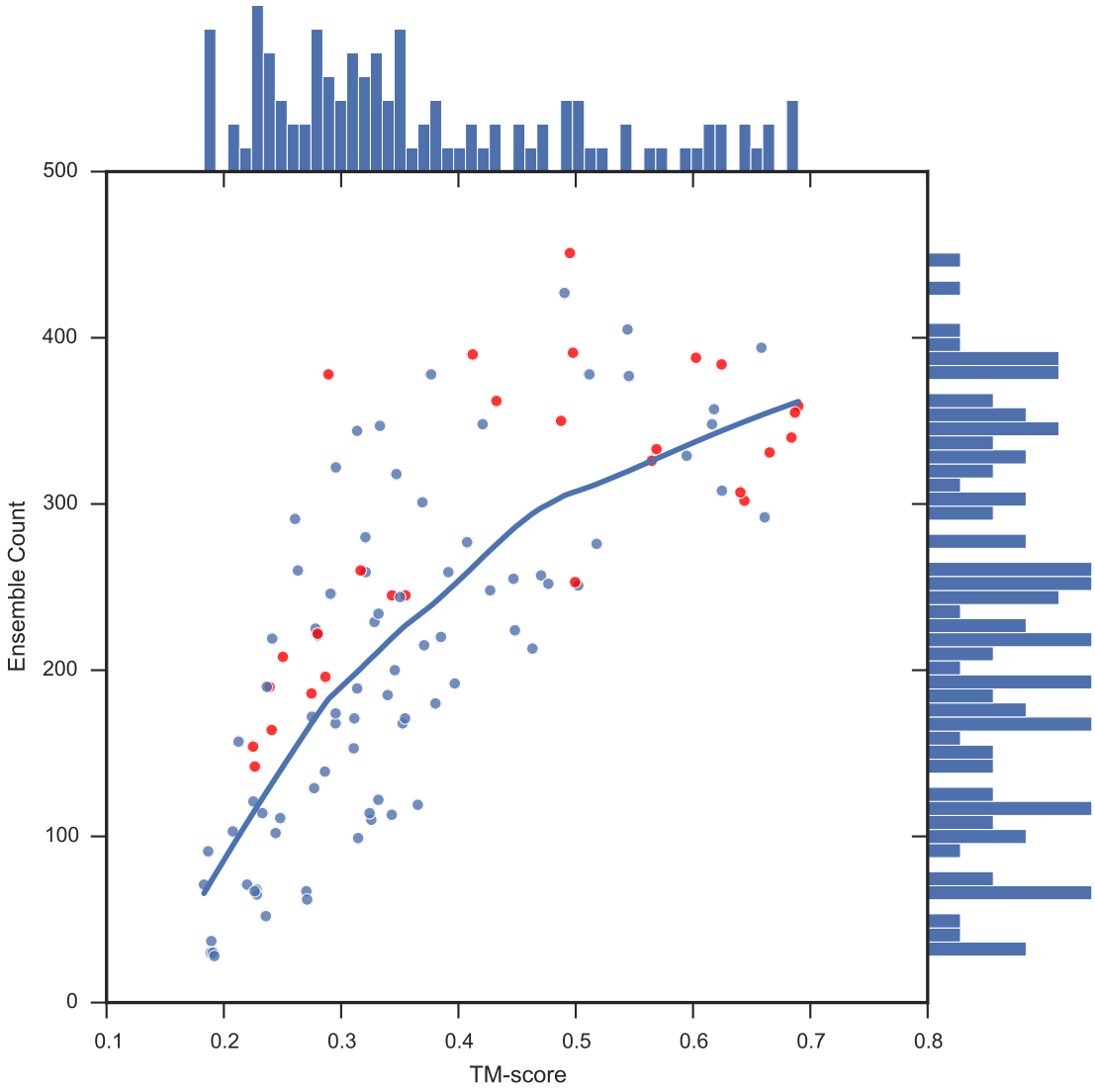

Figure 3.13: Comparison of median TM-score comparison (per 1,000 decoys) against the resulting AMPLE ensemble search model count. LOWESS function fitted to data to illustrate relationship. Red dots indicate successful ensemble sets.

Besides looking at the relationship between entire decoy sets and the resulting structure solutions on a per-target or per-condition basis, it is important to also consider individual ensemble search models, their origins and their properties in relation to MR metrics. Previous findings highlighted the relationship between the number of decoys in the first cluster and the quality of the decoys it contains (see Chapter XYZ). Here, we further support these findings given the positive relationship between the median TM-scores and the corresponding size of the largest SPICKER cluster (Fig. 3.14). An analysis of the cluster sizes demonstrates the downstream benefits of increased decoy quality through contact restraints in the folding process (Fig. 3.15). The sizes of the first three clusters generated from most contact-restraint decoy sets greatly surpass their equivalent cluster sizes for unrestrained ROSETTA decoys. Given that cluster sizes correlate with decoy quality, the findings in this study also support that the mean Cα RMSD — as calculated

by THESEUS for cluster truncation — is directly related to better decoy quality via the larger number of decoys in each cluster (Fig. 3.16a). The same mean Cα RMSD is also related to the number of ensemble search models generated after subclustering (Fig. 3.16b), which hints towards a direct relationship between increased quality of 1,000 decoys per set and the total number of ensemble search models generated. Interestingly, GREMLIN decoys show similar Cα RMSD per cluster compared to unrestrained ROSETTA decoys (Fig. 3.17), unlike all other contact restraint guided structure predictions. However, it is worth noting that almost no distinction can be made amongst the remaining contact restraint treatments albeit some differences in cluster size distributions exist (Fig. 3.15).

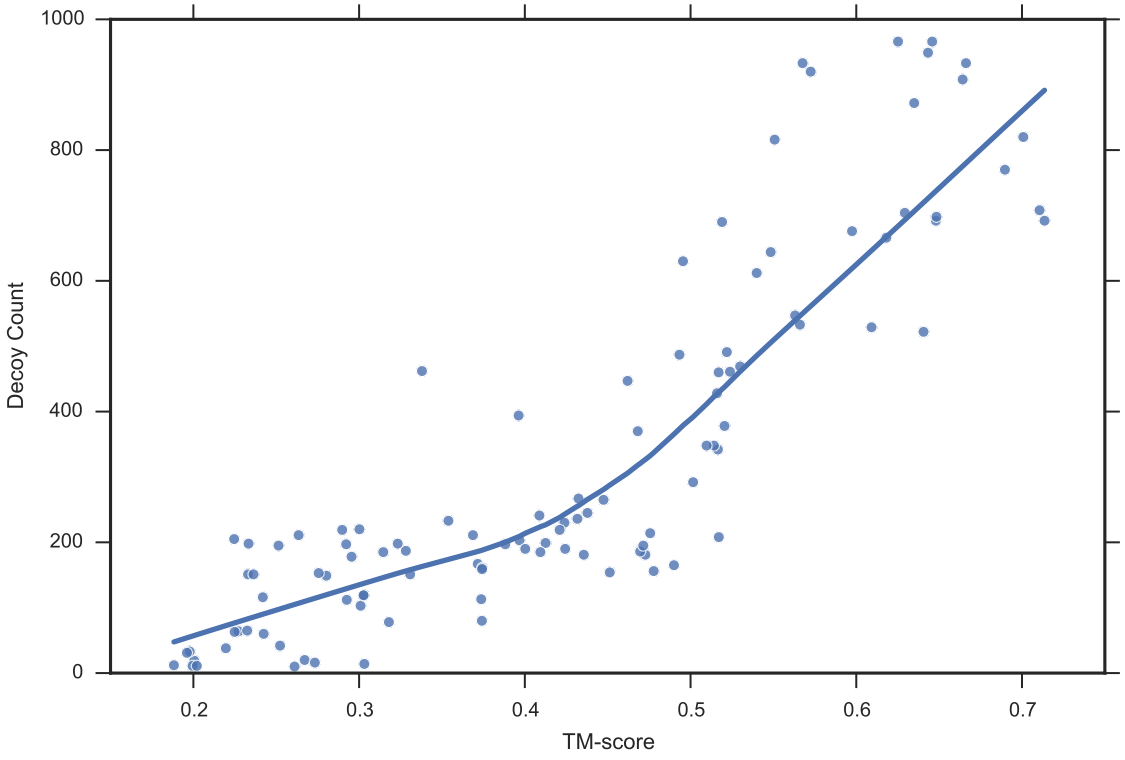

Figure 3.14: Relationship between cluster median TM-score and the number of cluster decoys. Blue line represents LOWESS relationship fitted to data.

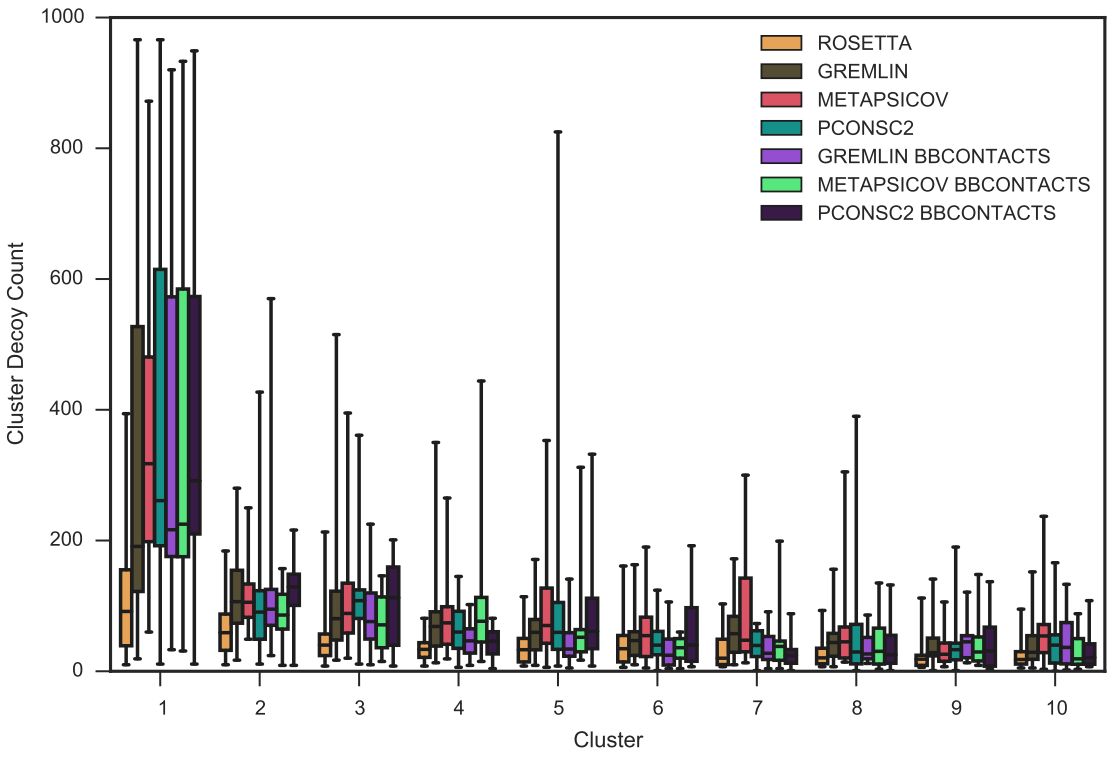

Figure 3.15: SPICKER cluster sizes of each target grouped the restraint condition used during the structure prediction protocol. Whiskers span the range from the minimum to maximum counts.

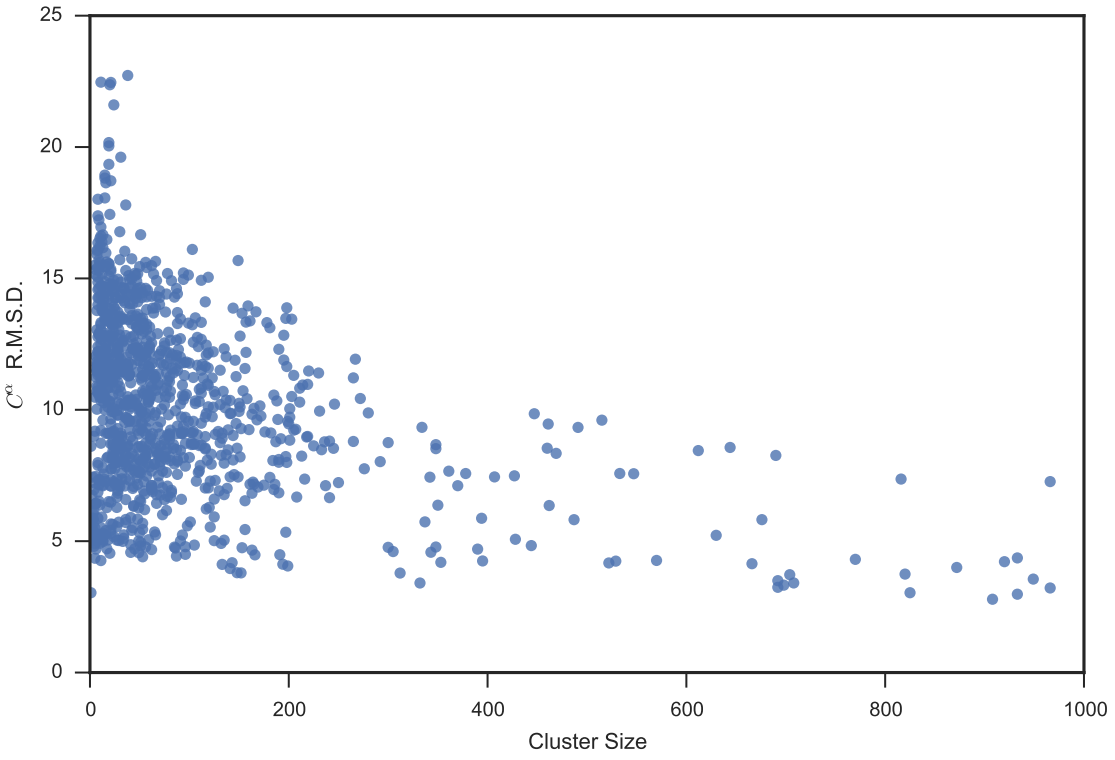

(a)

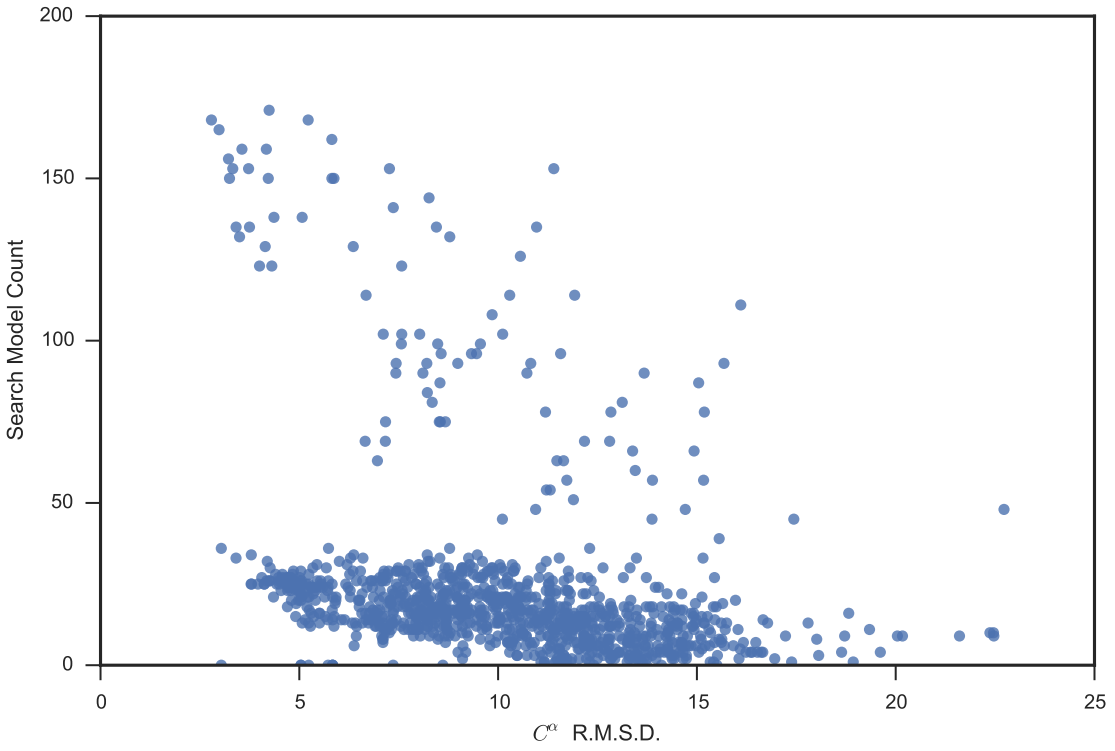

(b)

Figure 3.16: (a) Number of decoys per SPICKER cluster plotted against the mean Cα-atom RMSD for all decoys in each cluster. (b) Mean Cα-atom RMSD for decoys per cluster plotted against the number of search models derived from the cluster.

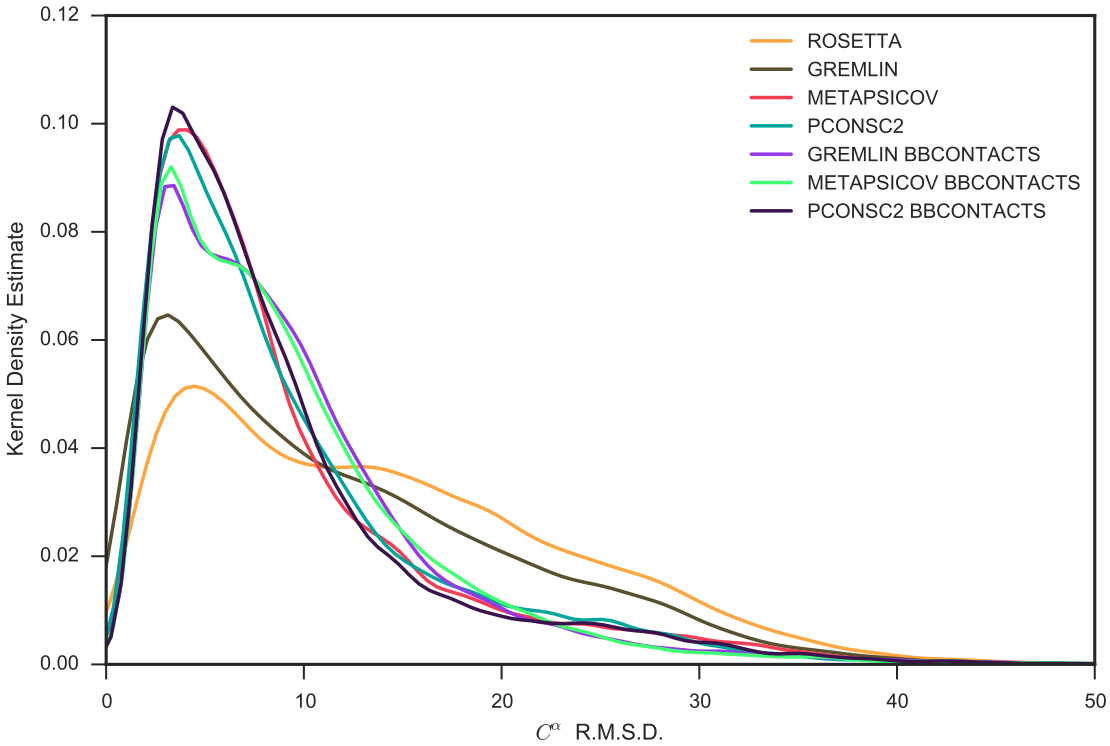

Figure 3.17: Kernel density estimate of Cα interatomic RMSD for SPICKER clusters.

The structure solution through pipelines like AMPLE and other unconventional MR software [197, 198] can result from the placement of generated (ensemble) search models either in- or out-of-sequence register. The RIO metric [116] can reliably assess the register placement, and thus was used to analyse the MR placements of all search models of the seven targets with structure solutions from one or more decoy sets. The RIO scores for the hypothetical protein AQ_1354 (PDB: 1oz9) strongly support the high quality decoys used as input across all seven contact conditions (Fig. 3.18). Most search models are placed in-register and hardly any search models with out-of-register RIO scores failed either. In contrast, the search models of N-(5-phosphoribosyl)anthranilate isomerase (PDB: 4aaj) — derived from high quality decoys in most conditions — shows a low percentage of AMPLE search models with RIO scores leading to structure solution (Fig. 3.18). Furthermore, the RIO scores normalized by the target chain length indicate that search models, independent of MR structure solution, were relatively small only exceeding 20% of the total target sequence in a few cases.

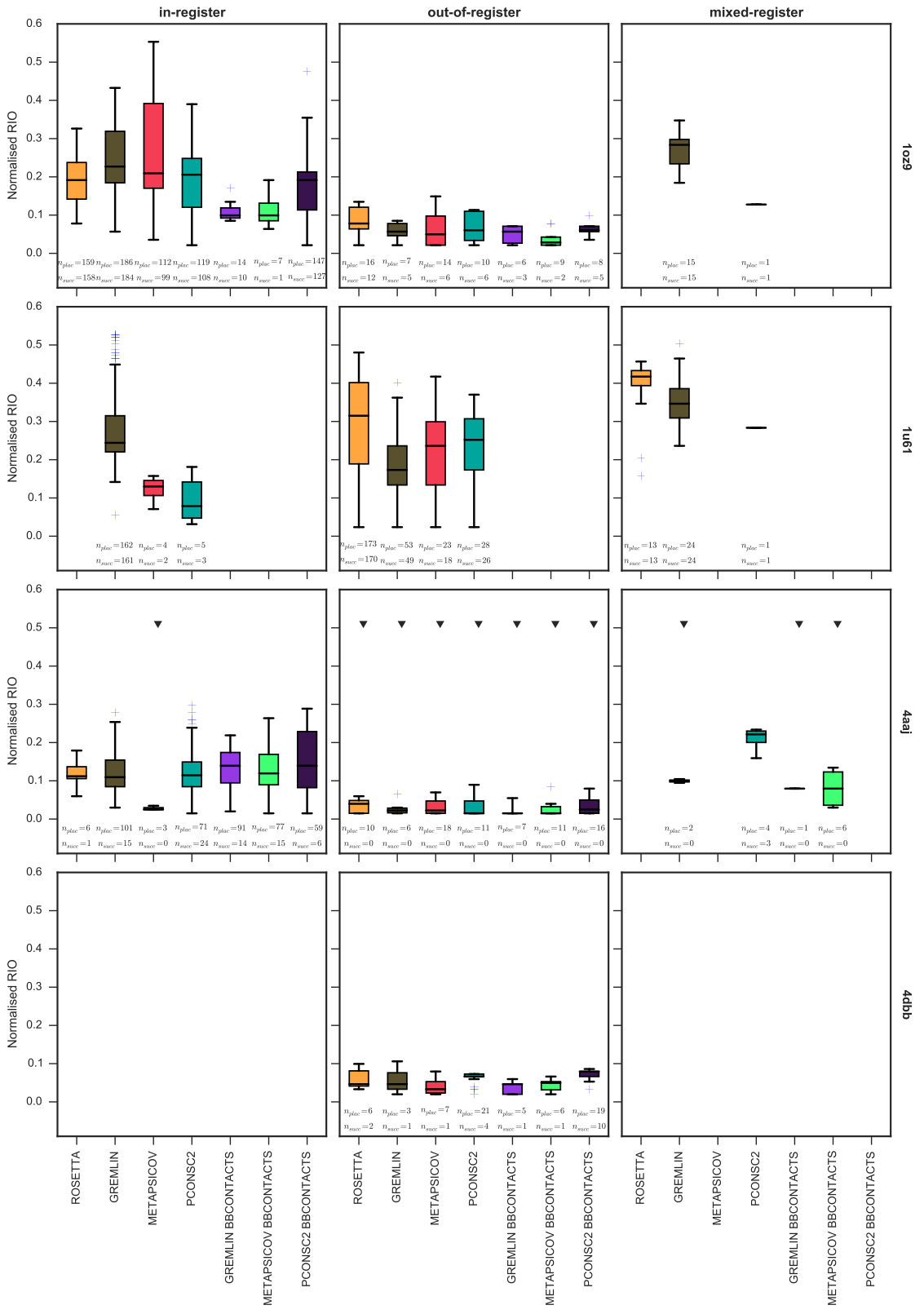

Figure 3.18: Normalised RIO score analysis of four successful targets in the MR dataset. Black triangles indicate AMPLE search model sets without a structure solution.

One interesting target in this set with respect to the sequence register of the AMPLE search models leading to structure solution is putative ribonuclease III (PDB: 1u61). Al-

though decoys from all contact conditions readily solved this target with at least 20 or more AMPLE search models, one interesting aspect arises from the RIO register analysis. Only GREMLIN decoys are primarily placed in-register (Fig. 3.18). AMPLE search models derived from the other three contact conditions, and in particular those from ROSETTA decoys, are primarily placed out-of-register with sequence coverage values of roughly 25%. In fact, a close analysis of the diversity of AMPLE search models highlights the accuracy of GREMLIN search models which represent a closely-matched substructure of the target protein (Fig. 3.19).

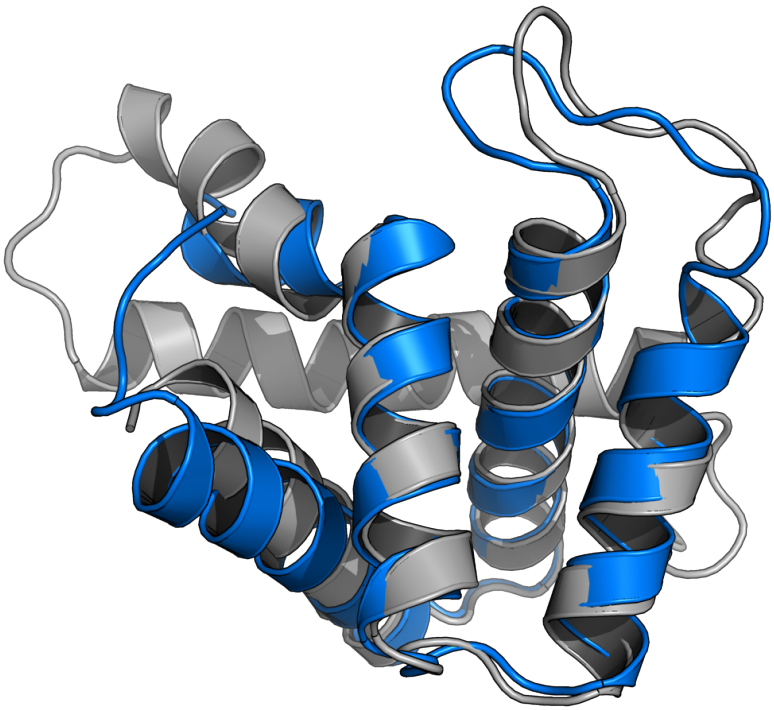

Figure 3.19: Successful search model (blue cartoon) post-PHASER placement superposed with the native structure (gray cartoon) for putative ribonuclease III (PDB: 1u61).

Compared to all other targets with structure solutions in at least one condition, the PTB domain of Mint1 (PDB: 4dbb) produced interesting yet somewhat surprising results. None of the search models, independent of their decoy source, achieved correct placement with any residue being in register. All structure solutions were obtained from out-of-register search model placements (Fig. 3.18). A visual inspection of all successful search models revealed that structure solutions were exclusively obtained with idealised fragments. ROSETTA, GREMLIN and METAPSICOV decoys resulted in one or more single-helix ensemble search models that led to structure solution (Fig. 3.20). More interestingly though, PCONSC2, GREMLIN BBCONTACTS, METAPSICOV BBCONTACTS and PCONSC2 BBCONTACTS decoys yielded one or more two-strand β-sheets which, after successful MR, yielded fully built structures (Fig. 3.20).

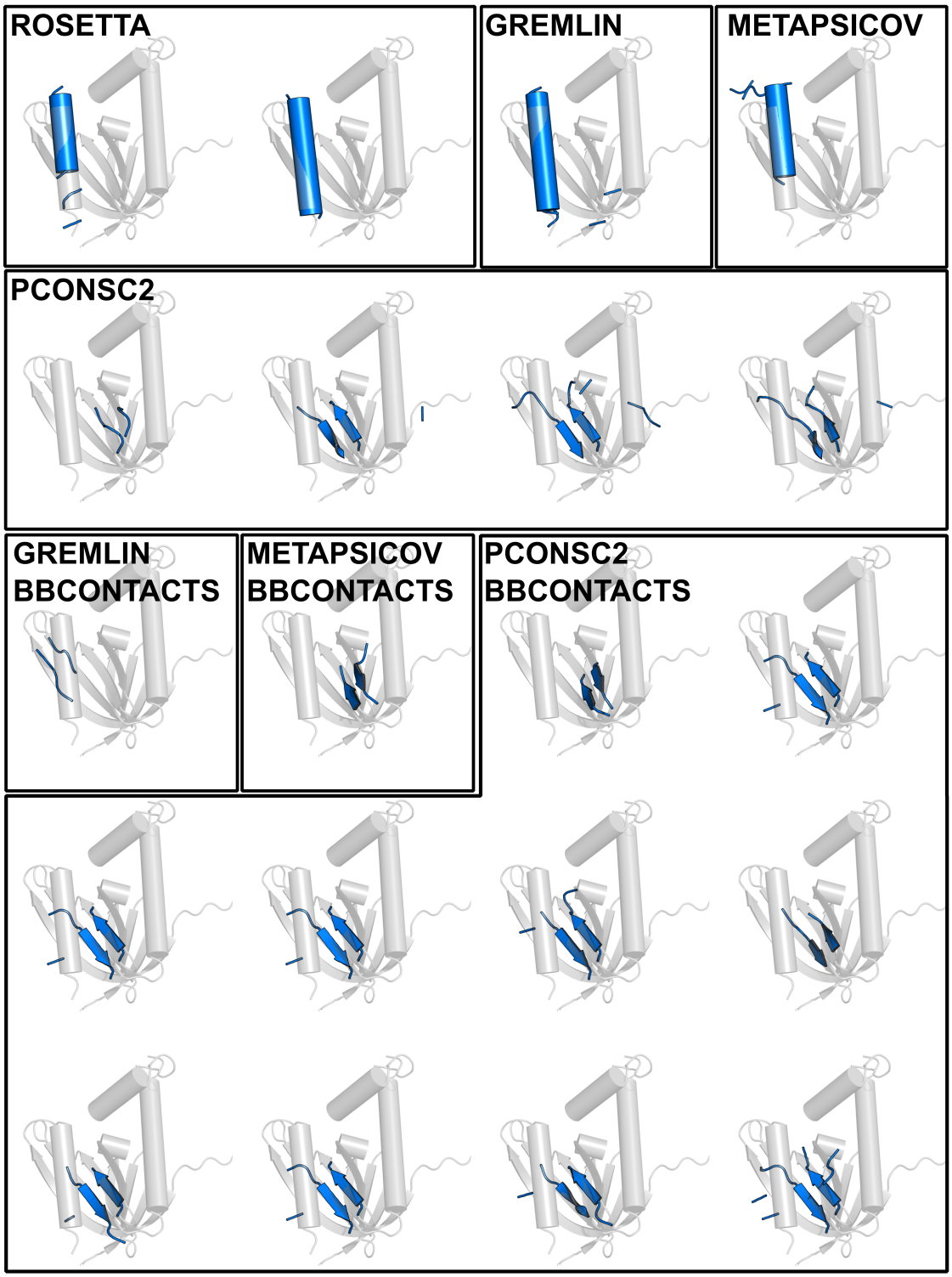

Figure 3.20: Successful search models post-PHASER placement (blue) superposed to the reference crystal structure (grey) for PTB domain of Mint1 (PDB: 4dbb).

Lastly, three targets were solved with one or two decoy sets alone. The structures of the retinoic acid nuclear receptor HRAR (PDB: 1fcy) and the peptide methionine sulfoxide reductase (PDB: 1fvg) were only solved with a handful of AMPLE search models.

Often singleton solutions like these are achieved through AMPLEs cluster-and-truncate procedure producing a single, idealised helix as search model. Here, we confirm such findings for target 1fcy, whereby single out-of-register helices derived from ROSETTA and GREMLIN decoys achieved structure solutions. However, the singleton search model derived from the GREMLIN BBCONTACTS decoys for the peptide methionine sulfoxide reductase (PDB: 1fvg) was placed in-register. A closer inspection of this AMPLE ensemble search model highlights a great success of the approach of adding BBCONTACTS distance restraints to separately predicted contact maps. In this instance, the successful AMPLE ensemble search model has 77% of its 49 residues placed in-register. More importantly, the search model is made up of two β-strands packing against each other, which was supported by BBCONTACTS predictions (Fig. 3.21). The last case, glycosylase domain of MBD4 (PDB: 4e9e), solved solely with GREMLIN decoys yielding 71 structure solutions. All successful AMPLE search models derived from the GREMLIN decoys were placed in-register.

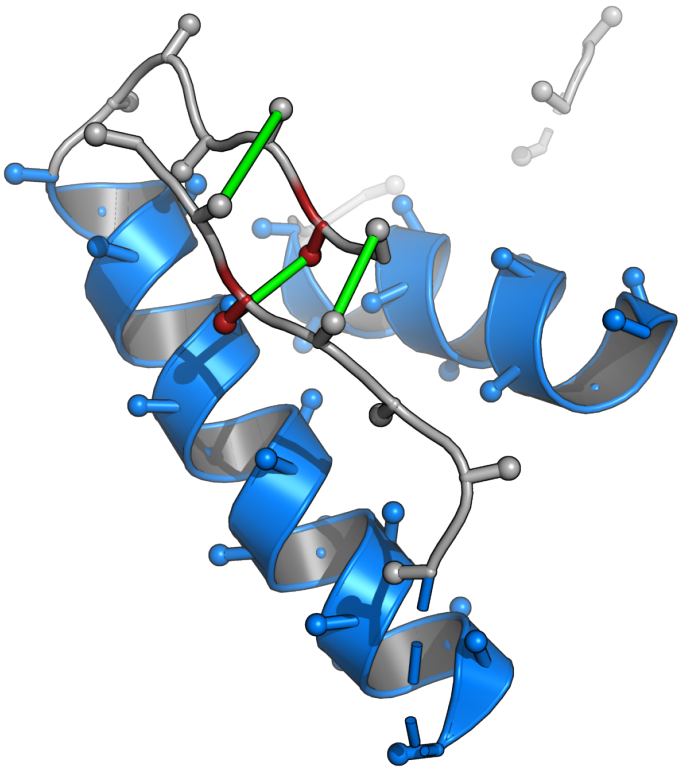

Figure 3.21: Successful search model post-PHASER placement for peptide methionine sulfoxide reductase (PDB: 1fvg). BBCONTACTS distance restraints are represented as green lines, α-helices in blue and β-strands in red. Secondary structure assignment calculated with STRIDE [199].

3.4 Discussion

This study was designed to explore the state-of-the-art metapredictor pipelines for residue-residue contact prediction. The main focus of this work was to distinguish differences in three key parts: raw contact predictions, their use in *ab initio* structure prediction and finally the effects on unconventional MR using AMPLE.

Key findings in this study revealed METAPSICOV and PCONSC2 metapredictors to yield the most precise contact predictions regardless of target fold or size. These results are in line with previous findings, which independently confirmed METAPSICOV contact predictions to yield the highest precision across numerous prediction algorithms [111, 112]. However, work in this study cannot confirm their findings, which demonstrate more precise contact predictions for all-β and mixed α-β protein targets compared to all-α ones. Several reasons might give insights into this discrepancy: (1) a much smaller sample size was trialled in this study (Wuyun et al. [112]: 680; De Oliveira et al. [111]: 3500); (2) the targets were chosen to deliberately sample various alignment depths including relatively low Neff (< 200) values; (3) only final contact predictions were analysed as part of this work, thus benefiting from post-prediction consensus finding and contact map processing through unsupervised machine-learning algorithms.

Furthermore, we demonstrated in this study that two similar ROSETTA energy functions yield different structure prediction results. The FADE function on average achieves more accurate structure predictions compared to the SIGMOID one. This result seems striking at first; however, a closer inspection of each of the energy function parameters gives possible insights into the reasons for the different outcomes. The FADE energy function defines both a maximum and minimum distance. The FADE energy function also does not consider amino acid-specific distances while the SIGMOID function does [90]. Furthermore, a custom weight factor is added for SIGMOID restraints to balance the restraint term in the overall energy term of each decoy (Sergey Ovchinnikov, personal communication). Thus, small changes in each of those definitions could have significant effects on the final structure prediction. Unfortunately, it is out of the scope of this study to explore all variations, and thus results aid primarily as guide for future work and AMPLE users. This study highlighted again the benefits of adding BBCONTACTS predictions to existing contact maps to further restrain β-rich regions during structure prediction. This work provides further support to work outlined in Chapter XYZ.

Lastly, part of the comparison carried out in this study was aimed specifically at macromolecular crystallographers and, in particular, AMPLE users. Beyond the proof-of-principle study described in Chapter XYZ, this work further illustrates how important additional restraint information can be to increase the chances of unconventional MR success. However, this work also highlighted limitations in the AMPLE routine whereby decoys that were restrained by residue-residue contacts achieved much higher decoy quality compared to unrestrained ROSETTA decoys, yet solved fewer targets. The idea that

restrained decoys might benefit from a different kind of processing was further supported by the most successful decoy sets, which were obtained with GREMLIN contact predictions. Given that GREMLIN and ROSETTA decoys achieved similar decoy qualities for a large set, their structure solutions were identical for all of ROSETTAs successful solutions. GREMLIN decoys outperformed ROSETTA decoys solely on the basis that it acquired highly accurate decoys for one further target, and thus achieved the most structure solutions in this study.

Therefore, further work is required to identify the optimal strategy for decoy sets with high structural similarities to the native fold. Such work could focus on the recent idea of selecting decoys based on their long-range contact precision [74, 111] to specifically eliminate the worst decoys, and thus enhance a more fine-grained clustering approach in SPICKER. Alternatively, truncation could be guided by alternative means, such as the importance of each residue in the predicted contact map. Ultimately, it is key to improve the AMPLE protocol to exploit the much higher decoy quality to enhance the users chance of success.

Chapter 4

Protein fragments as search models in Molecular Replacement

4.1 Introduction

Ab initio structure prediction algorithms typically start with a coarse grained search of conformational space through the assembly of previously picked structural fragments. As such, the accuracy of structure prediction is heavily dependent on the similarity of fragments to the target fold for each position [54]. Thus, the necessary structural information for accurate structure prediction must be encoded in the fragment library for a given target sequence. This approach allows the modelling of new protein folds by considering them as assemblies of already known building blocks, such as super-secondary structure motifs [200]. Furthermore, fragments similar to those typically selected for ab initio structure prediction were successfully used in other areas of structural biology including NMR [201, 202] and X-ray crystallography [203] studies to elucidate unknown protein folds. Despite their modest success, almost all attempts neglected target-specific information generally available to structural biologists obtainable through bioinformatics software. This information includes the primary sequence of the target, torsion angle predictions, predicted solvent accessibility or co-evolution information. In theory, all additional information should improve the generation of such fragment libraries by aiding the selection process or cross-validating the identified fragments.

Over the last decade, efforts have been made to improve the precision of structural fragment libraries used in *ab initio* structure prediction [47–54]. Various different algorithms have been developed to generate static and dynamic fragment libraries. Static fragment libraries are those pre-computed and generally consist of common super-secondary structure motifs. In comparison, dynamic fragment libraries consist of fragments of variable lengths acknowledging the fragment-dependent optimal length. Most commonly used in *ab initio* structure prediction are dynamic algorithms, such as FLIB [53], NNmake [54] or HHfrag [50]. Dynamic-library producing algorithms differ in their definition of ideal fragment lengths, the default number of fragments used per position and the way in which fragments are extracted. However, these algorithms typically share the same additional sequence-based information used to aid the selection of target fragments, which usually includes sequence similarity, three-state secondary structure prediction and torsion angle prediction.

Given that fragment libraries selected to perform *ab initio* structure prediction can contain high quality fragments or super-secondary structure motifs, those fragments must sometimes be suitable as MR search models. Correct identification of true positives should allow for dynamic fragment selection to achieve MR structure solution without the overhead of *ab initio* structure prediction. Furthermore, dynamic algorithms could pick fragments of varying lengths, possibly matching co-evolution data or other externally obtainable restraints to validate fragments prior to any MR attempt. As such, the work in this chapter focuses on exploring this idea using FLIB [53], a dynamic fragment picking algorithm considering co-evolution data to verify fragments during the picking process.

4.2 Methods

4.2.1 Target selection

Four targets were manually selected for this study. The crystallographic data needed a resolution of around 1.5A with a single molecule in the asymmetric unit. The target chain length needed to be below 150 residues, and the fold of the protein structure to be either mixed α-βor all-β. A further target selection criterion was the availability of precise contact information for fragment selection.

The PDB identifiers of the selected targets are: 1aba, 1lo7, 1u06, and 5nfc. The former two are described in Table 2.1. Target 1u06 is a recently published structure of α-spectrin SH3 domain (PDB ID: 1kjl in Table 2.1) with a resolution of 1.49Å. Target 5nfc is a recently published structure of Galectin-3 (PDB ID: 1kjl in Table 2.1) with a resolution of 1.59Å. This resulted in a dataset with similar attributes for each target: crystallographic data resolution of 1.5Å with a single molecule in the asymmetric unit, and the target chain length of < 150 residues. Each fold class, mixed α-βand all-β, contained two targets.

4.2.2 Fragment picking using FLIB

FLIB [53] requires four inputs: the predicted secondary structure, predicted torsion angles, residue-residue contact pair data and a copy of the PDB. The secondary structure for each target was predicted using PSIPRED v4.0 [204] with default parameters. The torsion angles were predicted using SPIDER2 [205] with default parameters, and residue-residue contact pairs using METAPSICOV v1.04 [100] with default parameters. HHBLITS v2.0.16 [189] with database version `uniprot20_2016_02` was used by METAPSICOV to generate the MSA for contact prediction of each target sequence. BLASTP v2.2.31+ [206, 207] was used by PSIPRED with the UNIPROT database version `uniref90-2016_06`. The local copy of the PDB for fragment picking was downloaded on August 11, 2016.

Two modifications were made to the default FLIB v1.01 (`https://github.com/sauloho/FLIB-Coevo`, commit `abade3b`) protocol. The first focuses on exclusion of fragments with $> 90\%$ helical content (assigned by DSSP [199]). If fragments with $> 90\%$ helical content are allowed and residues are predicted to be part of an α-helix, fragment libraries tend to be overpopulated for these positions with short helices. This would generate fragment libraries similar to ideal helix libraries, which is not the purpose of this work. The second modification was to allow fragments with RMSD > 10.0Å to the reference structure to be considered. This modification to the FLIB algorithm was implemented for development purposes by the authors to validate the performance of the algorithm. However, to allow for the automatic calculation of RMSD value of each fragment without deliberately excluding less-similar fragments this modification was lifted.

Two-hundred fragments were picked per target sequence position. Top-L or $L/2$ contact pairs were selected from both METAPSICOV STAGE 1 and STAGE 2 predictions with a minimum sequence separation of either 6 or 12 residues. Helical fragments were either included or excluded. The fragment length ranged from either 6 or 12 (dependent on minimum sequence separation) to 63 residues. In all instances the `-coevo_only` flag was set to exclude fragments with starting residues undefined by any contact pair in the set [1]. Overall, this generated 16 fragment libraries per target.

Each fragment library was then filtered to remove homologs of the target to be solved. BLASTP [206, 207] and HHPRED [208] searches were conducted to identify homologous PDB entries. The BLASTP search was performed identically to Oliveira et al. [53] using an E-value cutoff of 0.05. The HHPRED search parameters were identical to the MPI-Toolkit [209] webserver version (`https://toolkit.tuebingen.mpg.de/`). Fragments derived from PDB entries identified by BLASTP and HHPRED (probability score of ≥ 20.0) were excluded from the fragment libraries.

All per-target fragments were then binned by their peptide lengths. Subsequently, they were ranked by FLIB scores and RMSD values, and the best fragment from each length-dependent bin selected. Partially redundant fragments of the same template structure consisting of the same region with varying flanking residues were kept, if they were ranked top for each fragment length group. Finally, the coordinates of the fragment backbone atoms were extracted to create poly-alanine search models.

Note, the FLIB score refers in this chapter to the predicted torsion angle score for a given fragment, which FLIB uses in its default routine to rank fragments with lower scores being more favourable [53].

4.2.3 Molecular Replacement in MRBUMP

The previously extracted fragments were subjected to the MR pipeline MRBUMP [122]. This uses PHASER [123] for MR, REFMAC5 [27] for refinement and SHELXE [125] for density modification and main-chain tracing. MRBUMP default parameters were used with exception of the PHASER RMSD estimate. Each fragment was subjected to MRBUMP using PHASER RMSD values of 0.1, 0.6 and 1.0Å.

4.2.4 Assessment of FLIB fragments

Fragment torsion angles — predicted by SPIDER2 [205] — were assessed using the Mean Absolute Error (MAE), which evaluates the average absolute difference between the pre-

[1] The `-coevo_only` flag was intended to select only fragments that satisfied at least one contact pair. This intended behaviour was not part of the source code throughout this study, and only detected post-analysis. The issue was reported to the developers and has since been fixed in the FLIB source code (commit "`b3eb01d`").

dicted and experimentally determined angles [205]. To account for the periodicity of an angle, the smaller value of the absolute difference d_i and $360 - d_i$ was used. The coverage of a fragment library was assessed by the proportion of residues present in at least one fragment in the library. The precision of a fragment library was defined by the fraction of TP fragments. All fragments with an RMSD of < 1.5Å were considered TP else FP. The equation used to calculated the precision score is Eq. 2.3. The RMSD value, as calculated by FLIB [53], was computed between the aligned residues of the corresponding crystal structure and the fragment. The number of satisfied contact pairs in each fragment was calculated by scoring the number of TP contact pairs by using a contact's residue indexes according to sequence alignment provided by FLIB. MR success for each search model was solely assessed by SHELXE scores, whereby a CC score of ≥ 25.0 combined with an ACL score of ≥ 10.0 was required.

4.3 Results

In this study, the main objective was to determine if peptide fragments derived from protein structures in the PDB could be reliably selected and trialed in MR to achieve structure solutions. The fragment picking algorithm FLIB [53] was used to pick fragments given its novel approach of validating selected fragments against a set of predicted residue-residue contacts.

4.3.1 Precision of FLIB input data

The FLIB algorithm requires two sets of input data — the predicted secondary structure and per-residue torsion angles — for each target sequence alongside an optional third source of information in form of co-evolution data. The first part of the analysis in this study focuses on these data given that the FLIB fragment picking heavily relies on the individual features in the selection and scoring of each individual fragment [53]. Poor data at this stage could lead to poor fragments that would be unsuitable for MR trials given that high accuracy, i.e. a low RMSD value between the search model and target, is required.

The secondary structure prediction highlighted high precision between each target's prediction and the DSSP-assigned [199] secondary structure of the target reference structure (Fig. 4.1). The three targets with PDB identifiers 1aba, 1lo7 and 1u06 have secondary structure predictions with a precision of $> 89\%$. The fourth target, 5nfc, shows comparatively poor precision of 50.7% over all residues in the PSIPRED prediction and the DSSP assignment using the reference crystal structure. However, 11 out of 13 secondary structure features are correctly predicted, suggesting successful fragment picking is possible.

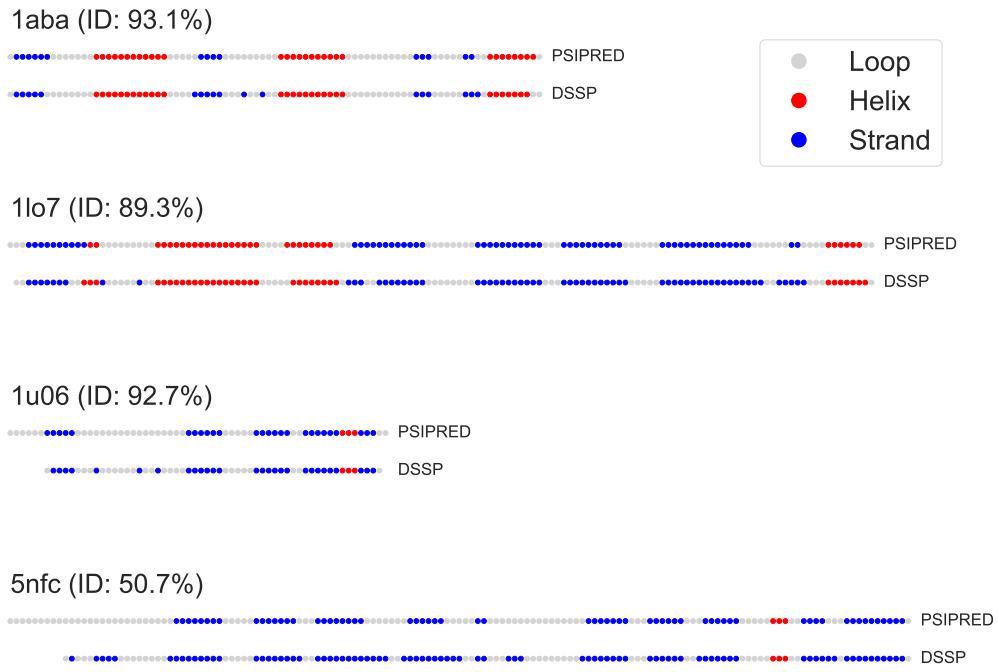

Figure 4.1: Schematic comparison of PSIPRED [204] secondary structure prediction and DSSP [199] assignment. Percentage identity is provided next to each identifier. The identity was computing using the Hamming distance over all positions present in the target sequence and reference structure.

The contact prediction data for METAPSICOV STAGE 1 and STAGE 2 predictions demonstrate the high precision scores achievable by this algorithm (Table 4.1). In this study, the top contact pairs at cutoffs L and $L/2$ were provided to the FLIB algorithm. All targets have precision scores for both sets of predictions at both cutoff levels of $>$ 0.6 (Table 4.1). A comparison of the sets of contact pairs shows that only every third (for $L/2$ contacts) or every other (for L contacts) contact pair is shared between both METAPSICOV STAGE predictions highlighting the importance of trialling both when selecting FLIB fragments (Jaccard index in Table 4.1).

Table 4.1: Precision scores for METAPSICOV [100] STAGE 1 and STAGE 2 contact predictions. Jaccard index calculated for the same L-dependent selection of contact pairs between METAPSICOV STAGE 1 and STAGE 2 predictions.

Target	$L/2$ **contact pairs**			L **contact pairs**		
	$\text{Prec}_{\text{STAGE 1}}$	$\text{Prec}_{\text{STAGE 2}}$	Jaccard	$\text{Prec}_{\text{STAGE 1}}$	$\text{Prec}_{\text{STAGE 2}}$	Jaccard
1aba	0.884	0.884	0.303	0.713	0.759	0.513
1lo7	0.857	0.957	0.308	0.738	0.837	0.446
1u06	0.839	0.806	0.378	0.710	0.787	0.459
5nfc	0.822	0.836	0.327	0.619	0.762	0.434

Given the two METAPSICOV contact prediction files, both show localised clusters of contact pairs characteristic for secondary structure features (Fig. 4.2). These clusters are more populated with contact pairs in METAPSICOV STAGE 2 predictions. This behaviour is to-be-expected given that the second stage in METAPSICOV screens the first to remove singleton contact pairs whilst enriching the already existing clusters [100]. Besides the visual analysis, a cluster determination study on each of those contact maps further confirmed a higher singleton frequency in METAPSICOV STAGE 1 predictions. The latter contain on average 9% more singleton contact pairs, and thus a higher degree of noise.

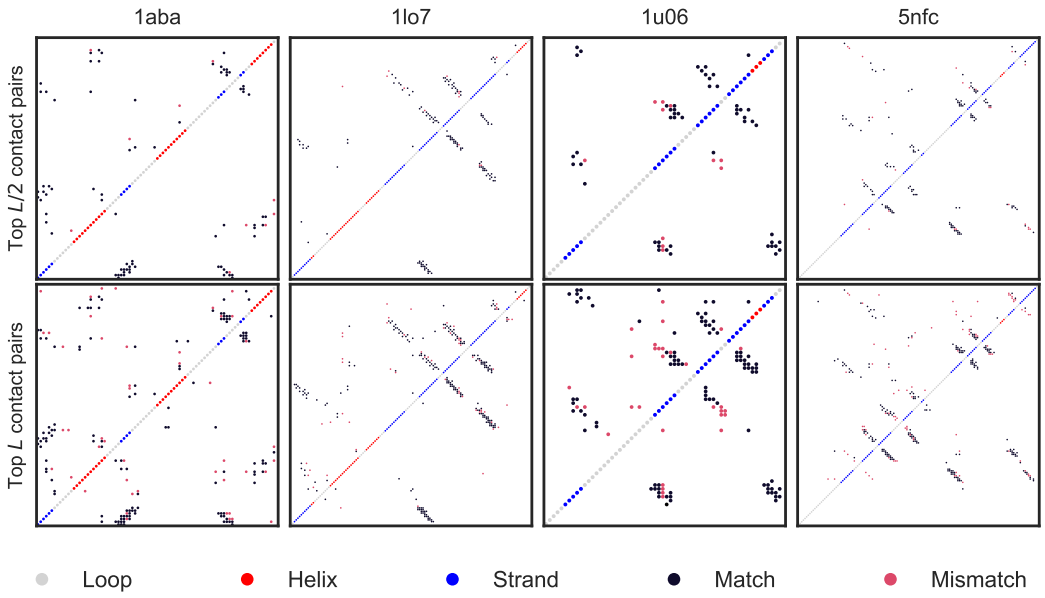

Figure 4.2: Comparison of $L/2$ and L correctly and incorrectly predicted contact pairs for four FLIB targets. Contacts were predicted using METAPSICOV [100] STAGE 1 (top left) and STAGE 2 (bottom right). True and false positive contact pairs were identified using a 8Å cutoff between Cα (Cβ in case of GLY) atoms of a reference crystal structure. PSIPRED [204] secondary structure prediction provided along the diagonal.

An analysis of the MAE of torsion angles between the SPIDER2 [205] prediction and a corresponding reference crystal structure highlights accurate predictions for three of four targets (Fig. 4.3). The largest MAE_{φ} across the four target sequences is 24.347°, and the largest MAE_{ψ} is 45.459° (MAE values for PDB entry 1u06). The smallest MAE_{φ} is 13.822° (PDB ID: 1aba) and smallest MAE_{ψ} is 17.273° (PDB ID: 1lo7). Segments in sequence space with regular secondary structure, as predicted by PSIPRED [204], result primarily in low MAE values of torsion angles. In contrast, unstructured regions highlight much larger MAE values indicating the difficulty of predicting these regions. Noticeably, the MAE_{ψ} appears to be much larger in those regions than the MAE_{φ} for the same residue.

In summary, all target sequences have FLIB input data of good quality, which should allow FLIB to select fragments of suitable accuracy for MR.

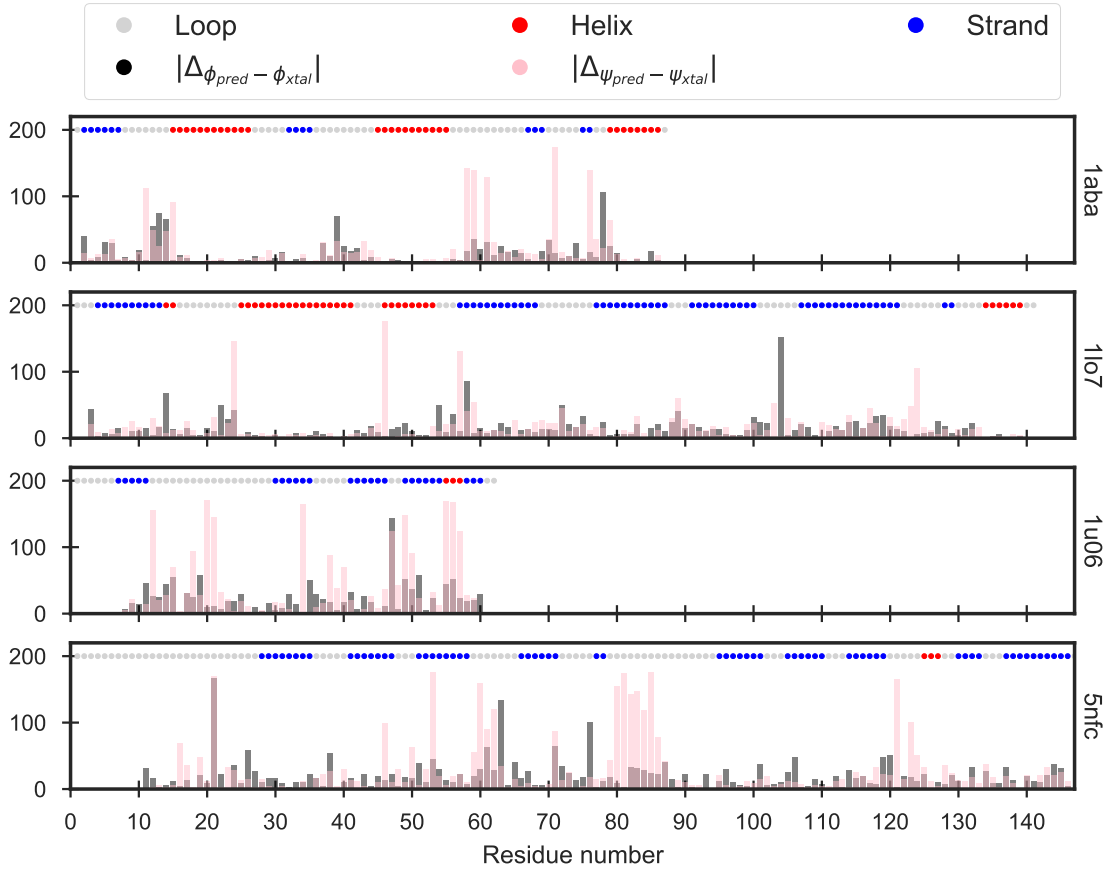

Figure 4.3: Comparison of MAE of torsion angles predicted by SPIDER2 and extracted from a corresponding PDB structure. PSIPRED [204] secondary structure prediction provided alongside the MAE values.

4.3.2 FLIB fragment picking

Sixteen FLIB fragment libraries were picked for each protein target in this study. Each fragment library consisted of one permutation of one of two contact prediction files and altering input parameters.

Across all four targets, the FLIB algorithm selected a total of 8,535,458 fragments (Table 4.2). The fragment libraries show similar statistics across the four protein targets despite the diversity in fold and chain lengths. The mean FLIB score is 3,200 score units with a mean RMSD of 9.00Å. Fragments for the alpha-spectrin SH3 domain (PDB ID: 1u06) scored the lowest mean FLIB score with 3,034 units; however, the same target scored the worst by mean RMSD with an average of 9.47Å. In contrast, fragments picked for the sequence of the bacteriophage T4 glutaredoxin (PDB ID: 1aba) achieved the best mean RMSD of 7.85Å given the second highest mean FLIB score of 3,217 units (Table 4.2).

Table 4.2: Summary of fragment statistics for FLIB libraries selected for four protein targets. Count_H corresponds to the count of fragments extracted from homologs.

Target	Count	Count_H	FLIB score			RMSD		
			Median	Mean	Std Dev	Median	Mean	Std Dev
1aba	2,091,321	45,133	3,061	3,217	1,405	7.70	7.85	3.81
1lo7	2,497,813	23,396	3,187	3,371	1,497	9.00	9.43	4.61
1u06	1,133,517	60,159	2,901	3,034	1,306	9.51	9.47	3.94
5nfc	2,812,807	48,828	2,982	3,127	1,316	8.89	9.16	4.18
Total	8,535,458	177,516	3,049	3,208	1,397	8.68	8.96	4.25

A split of the per-target fragment libraries by input options highlights the better fragment library quality under certain conditions with regards to the mean FLIB score and RMSD (Fig. 4.4). In particular, top-L (6 residues sequence separation) METAPSICOV STAGE 1 contact predictions yielded the lowest for both metrics across all targets. A comparison of the sequence separation, i.e. using all contact pairs or medium- and long-range ones only, strongly suggests much lower and thus more favourable scores for using short-, medium- and long-range contact pairs. A very similar difference is noticeable for METAPSICOV STAGE 2 contact predictions (Fig. 4.4).

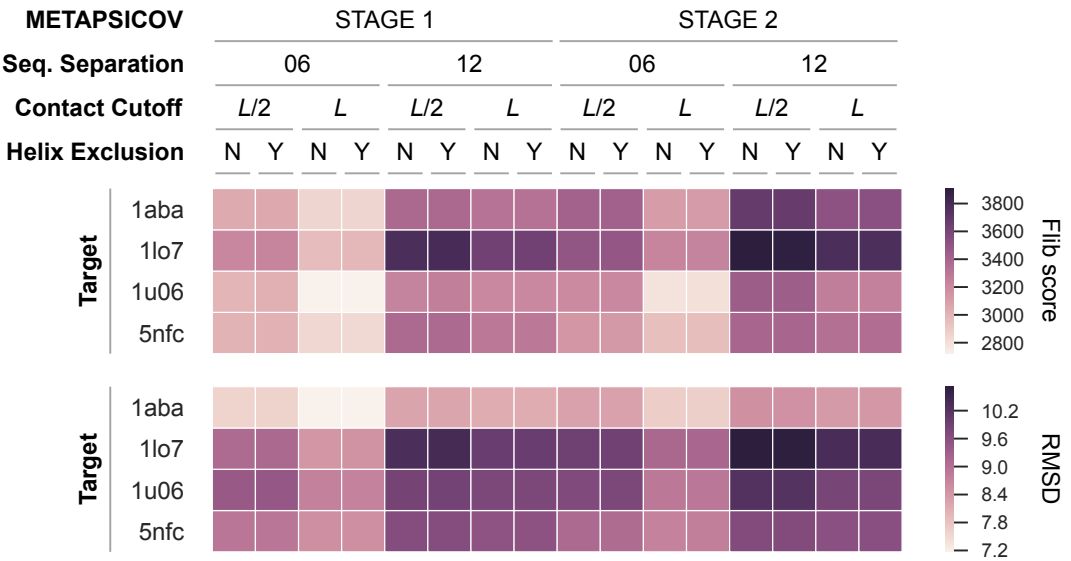

Figure 4.4: FLIB fragment library comparison for four targets highlighting the differences in mean FLIB score and RMSD by starting with different subsets of contact predictions. L refers to the number of residues per target sequence. Y refers to idealised α-helical fragment exclusion during fragment picking; N refers to treating those fragments like all others.

In this study, predicted contact information was used to further guide fragment selection. The FLIB algorithm only selected fragment for positions of the target sequence with at least one contact pair. Given this scenario, an analysis of the coverage of the target sequence with respect to each picking strategy further demonstrates the benefits of starting with METAPSICOV STAGE 1, i.e. noisier contact predictions (Fig. 4.5).

Coverage is more evenly spread across the target sequences compared to missing regions especially for target 4-hydroxybenzoyl CoA thioesterase (PDB ID: 1lo7) when starting with METAPSICOV STAGE 2 predictions. Noticeably, none of the picking strategies yielded any fragments for the C-termini of α-spectrin SH3 domain (PDB ID: 1u06) and galectin-3 CRD (PDB ID: 5nfc) (Fig. 4.5). Furthermore, an analysis of the precision of fragments in each library strongly supports the benefits of starting with top-L (6 residues sequence separation) METAPSICOV STAGE 1 contact pairs. Across all four targets, the coverage of correct fragments (classed by RMSD < 1.5Å to the reference structure) is highest for this condition. This is of particular importance for α-spectrin SH3 domain (PDB ID: 1u06) and galectin-3 CRD (PDB ID: 5nfc), for which most strategies picked very few to no correct fragments. Excluding idealised α-helical fragments does not affect the quality of the FLIB libraries greatly. A consideration of differences in mean FLIB and RMSD scores shows Δ differences of 25.68 and 0.06 between the comparable libraries, i.e. with and without idealised α-helical fragments.

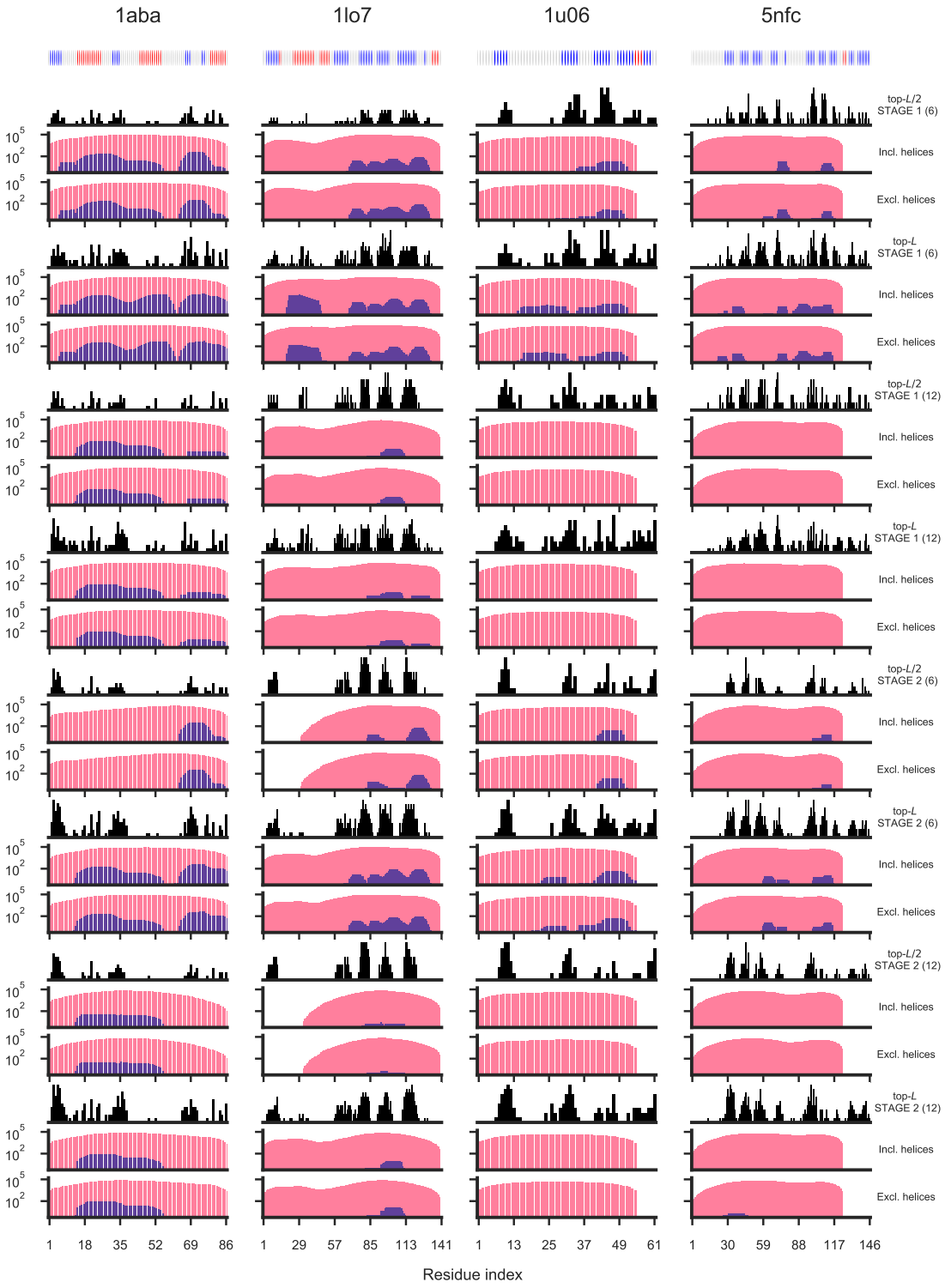

Figure 4.5: Summary of the coverage and precision of FLIB fragment libraries according to their target sequence. The coverage of all fragments with respect to their target-aligned sequence register are shown in red bars, and fragments with RMSD < 1.5Å to the reference structure in blue. The predicted secondary structure of each target sequence is given at the top: α-helices (red), β-strands (blue), and loops (gray). Contact prediction information is illustrated using black bars. The fragment frequency is shown using a log-scale.

Given that FLIB uses co-evolution data to help select fragments, it is little surprise that higher degrees of TP fragments co-localise with high-density contact pair regions along the target sequence (Fig. 4.5). This characteristic explains less TP fragments in top-$L/2$ fragment libraries because less contacts (compared to top-L) are available during fragment selection. The resulting selection is purely based on the FLIB score which might not yield high-accuracy fragments (RMSD < 1Å) as frequently. Therefore, the co-localisation of TP FLIB fragments and regions of high-density contact predictions highlights the importance of adding this additional source of information to pick fragments.

4.3.3 FLIB fragment selection for Molecular Replacement

One of the most important aspects of bypassing *ab initio* structure prediction and using the relevant fragments directly as MR search models is the selection of the fragments with the highest similarity between fragment and target structure.

A fragment's FLIB score — its cumulative absolute error of predicted torsion angles — has the highest correlation with the RMSD of a fragment compared to all other scores used in the FLIB protocol [53]. To validate this finding, all non-homologous fragments in this study were tested for a correlation between a their FLIB scores and RMSD values. The Spearman's rank-order correlation coefficient analysis confirms the correlation between a fragment's FLIB and RMSD scores (Fig. 4.6). However, the strength of the correlation varies greatly between different fragment libraries and targets. The optimal fragment picking strategy — top-L (6 residues sequence separation) METAPSICOV STAGE 1 — results in the strongest correlations across all targets. The same contact pair selection with METAPSICOV STAGE 2 predictions results in the second greatest correlations. Noticeably, the bacteriophage T4 glutaredoxin (PDB ID: 1aba) fragment libraries show much more positive correlations than the remaining targets. The fragments selected for α-spectrin SH3 domain (PDB ID: 1u06) show the overall weakest correlations. It is worth noting that the both targets, PDB IDs 1aba and 1lo7, are classed as mixed α-β targets, and thus the strength of this correlation might be fold dependent.

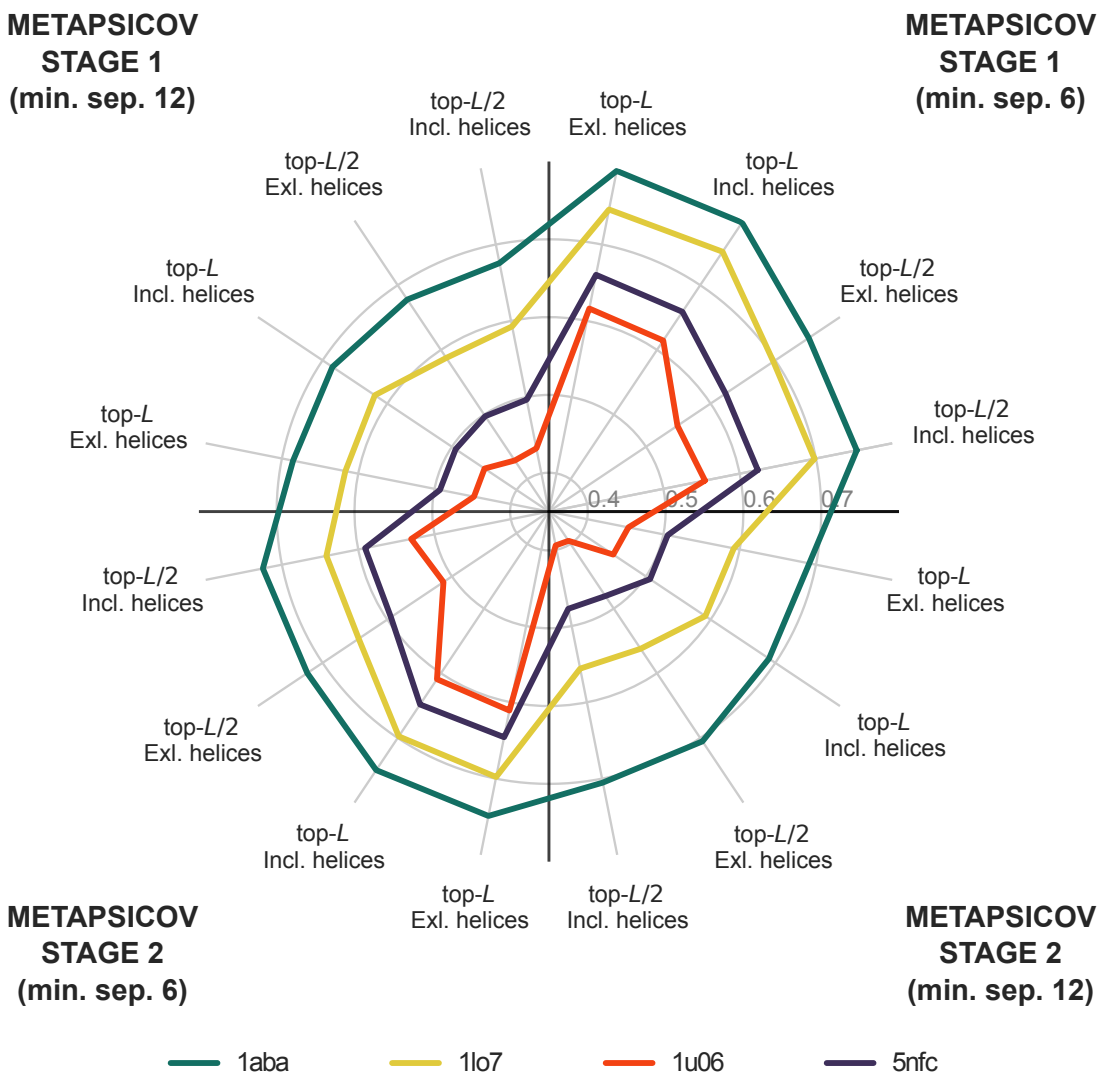

Figure 4.6: Spearman rank-order correlation coefficient analysis of FLIB fragments' FLIB score and RMSD value given the 16 unique fragment picking strategies across four targets. P-values of all Spearman correlations are < 0.001 and not shown for simplicity of the plot.

Further inspection of the fragments and the relationship between each fragment's FLIB score and RMSD value reveals a small subset of outliers in each fragment library. These fragments (hereafter referred to as outlier fragments) are sparse in each library with an overall mean count of $< 0.2\%$. An analysis for unique characteristics of these outliers, which would allow for their exclusion, reveals no unique feature. These fragments contain all secondary structure types, span the entire target sequence and range over all peptide lengths. Furthermore, they occur in all fragment libraries, irrelevant of their original picking strategy. The only characteristic setting these outlier fragments apart from the remaining set is a RMSD value of > 30Å. Nevertheless, it appears that these outlier fragments with unusually high RMSD values are never included in the final fragment search model set, given that their overall FLIB_{min} score is 796 units (one order of magnitude more than the overall minimum for the remaining fragments).

An analysis of the fragment metrics in the final MR set (6,547 fragments) further supports the positively linear relationship between a fragment's FLIB score and RMSD (Fig. 4.7a). However, the best FLIB fragments by RMSD show much less spread compared to the best fragments by FLIB score (Fig. 4.7b). Furthermore, the size of the fragments also positively correlates with the the FLIB ($\rho_{Spearman} = 0.860$, $p < 0.001$) and RMSD ($\rho_{Spearman} = 0.697$, $p < 0.001$) values. Longer fragments with higher dissimilarity with respect to the target show higher FLIB scores and RMSD values (Fig. 4.7a).

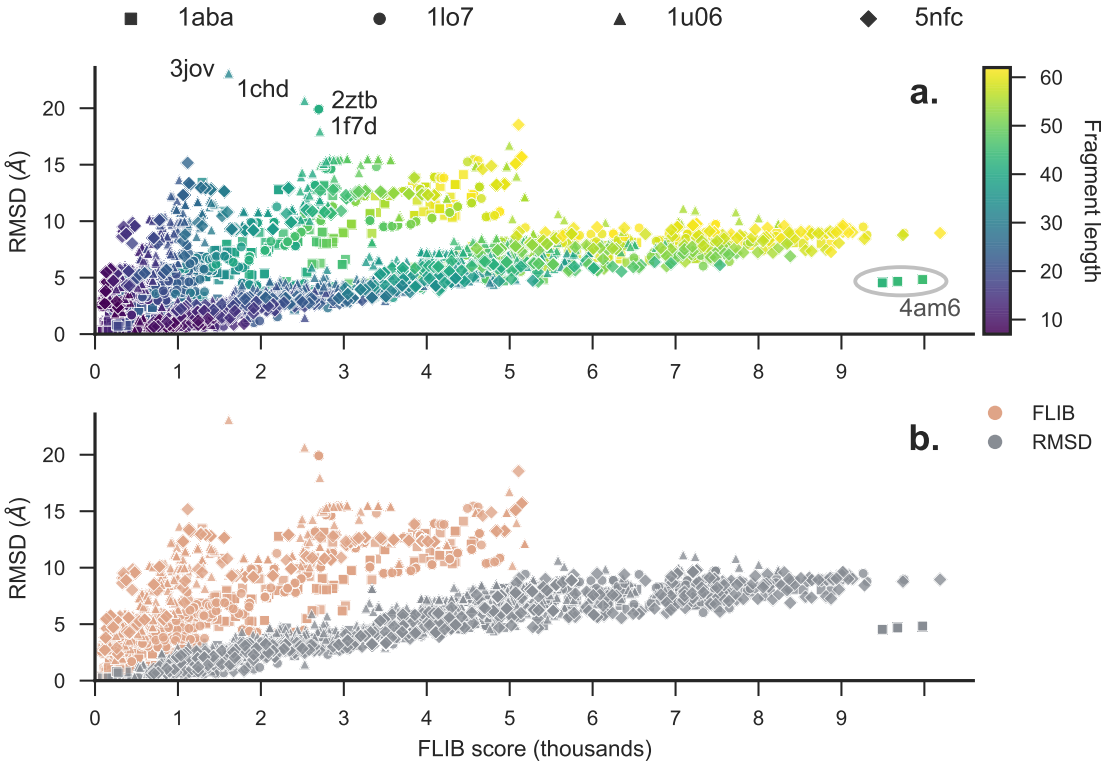

Figure 4.7: Scatterplot highlighting the positive correlation between fragment FLIB scores and RMSD values. The plot contains all fragments independent of target or picking strategy. **a.** The colour of each scatter point illustrates the fragment length. All extreme outlier fragments are highlighted with their PDB identifiers as labels. **b.** The colour codes indicate the sorting strategy to select the top FLIB fragments for each fragment peptide length bin.

Notably, a cluster of large fragments with some of the highest FLIB scores in the set show a reasonable similarity to their target structure (Fig. 4.7a). All fragments in this cluster were picked for the bacteriophage T4 glutaredoxin sequence (PDB ID: 1aba) and extracted from the same region of the crystal structure of the actin-related protein ARP8 (PDB ID: 4am6). In comparison, some smaller fragments with peptide lengths < 50 residues and lower FLIB scores of < 3000 show the highest RMSD values in the final set.

One further unique aspect of this study compared to other fragment-MR approaches is the use of residue-residue contact information to select fragments during picking, only selecting fragments for target-sequence residues with at least one contact pair in the pre-

dicted set (Saulo de Oliveira, personal communication). In the final set 39% of all fragments satisfy at least one, 26% at least two and 20% at least three contact pairs. Across the four targets, 50% of all fragments selected for 4-hydroxybenzoyl CoA thioesterase (PDB ID: 1lo7) satisfy at least one predicted contact pair (Fig. 4.8). In comparison, 28% of fragments selected for the α-spectrin SH3 domain (PDB ID: 1u06) satisfy at least one contact pair.

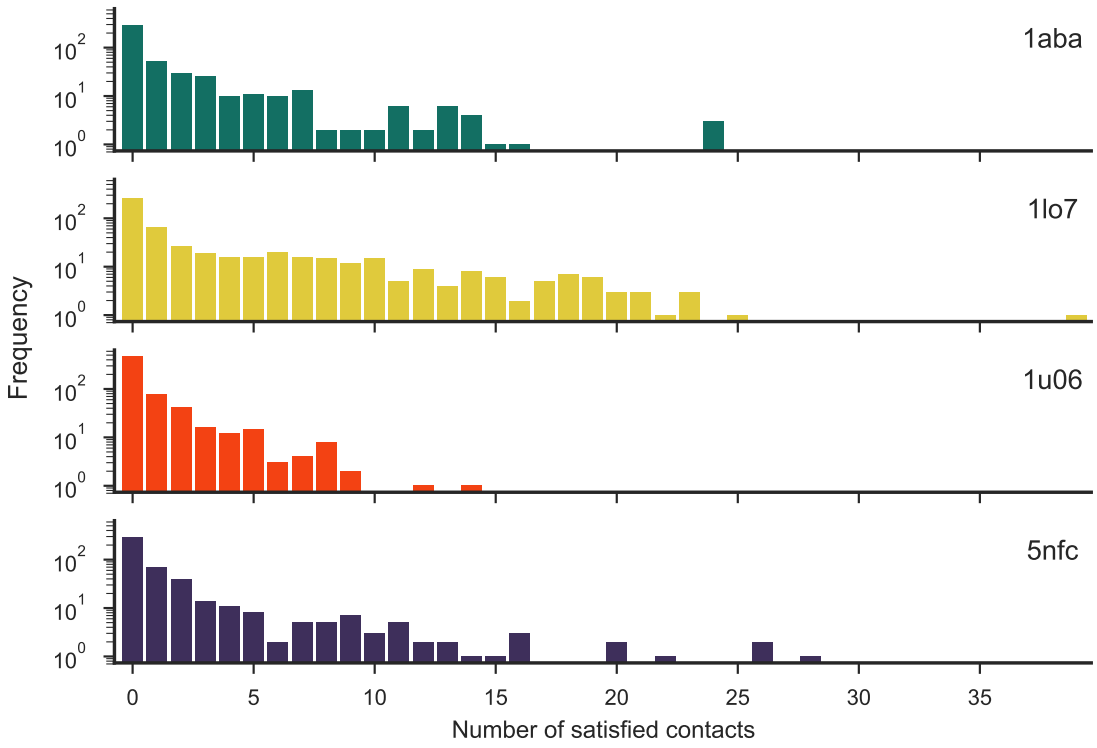

Figure 4.8: Distribution of contact precision for FLIB fragments selected as MR search models separated on a per-target basis.

Thus, the final set of FLIB fragment MR search models spans a wide range of peptide lengths, RMSD values, contact precision scores, and generally secondary structure make-up. To illustrate the latter, a random selection of sample fragments is illustrated in Fig. 4.9. Importantly, not a single super-secondary structure motif dominates the set, increasing the sampling diversity to be undertaken during MR.

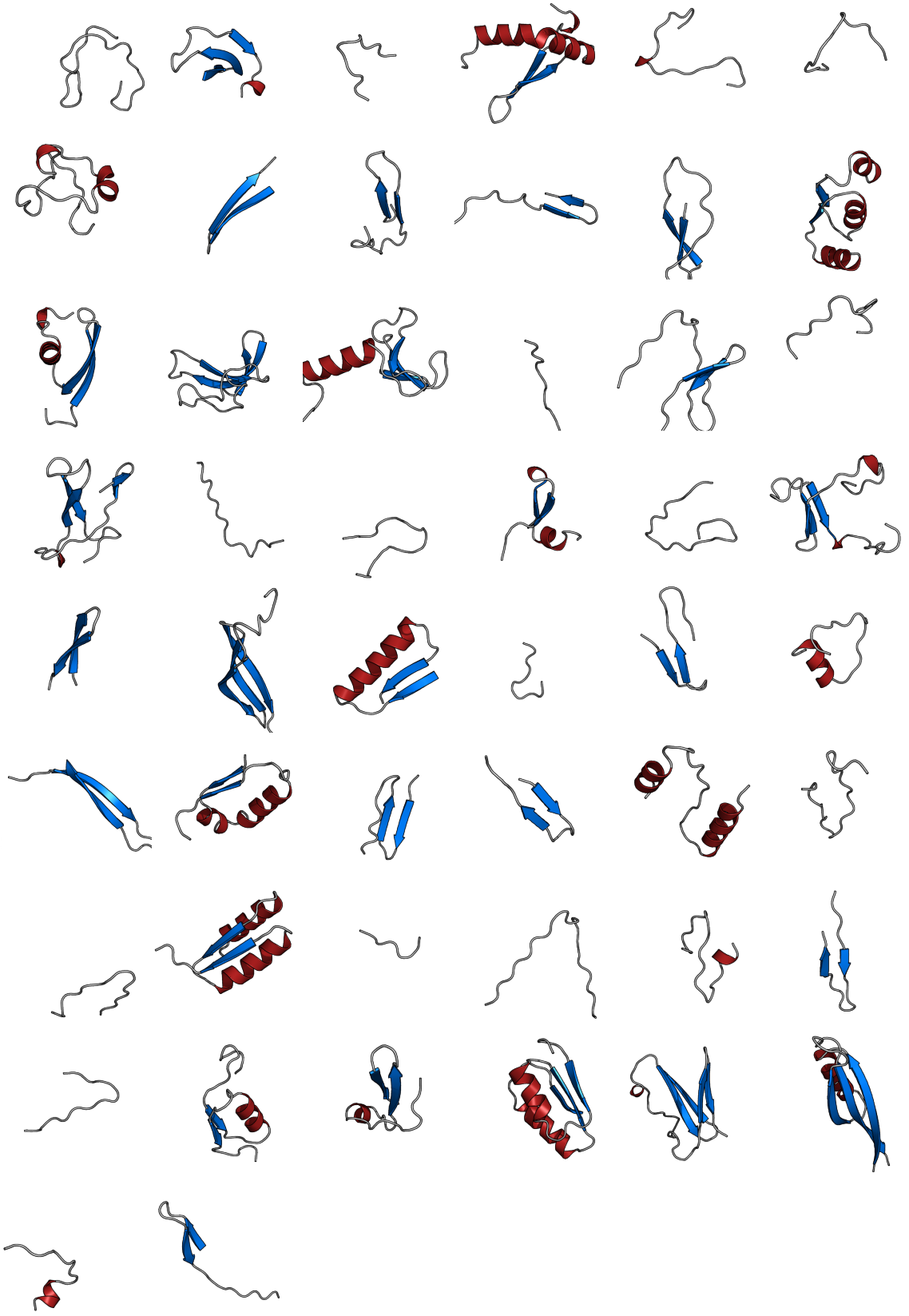

Figure 4.9: Non-redundant sample of FLIB fragment search models selected for four different protein targets. Secondary structure defined by and visualisation done in PyMOL [210]. Unpaired β-strands rendered using the loop style.

4.3.4 Molecular Replacement using FLIB fragments

FLIB fragments picked for four target sequences using a variety of FLIB input options generated $> 6,500$ fragments, which were subjected to the MR pipeline MRBUMP with their corresponding target experimental data. Given that each fragment was trialled with three different PHASER RMSD values, a total of 19,716 MR attempts were made across four target structures. Out of nearly 20,000 MR attempts, 299 led to the structure solutions of two targets, namely the T4 glutaredoxin (PDB ID: 1aba) and α-spectrin SH3 domain (PDB ID: 1u06) (Fig. 4.10).

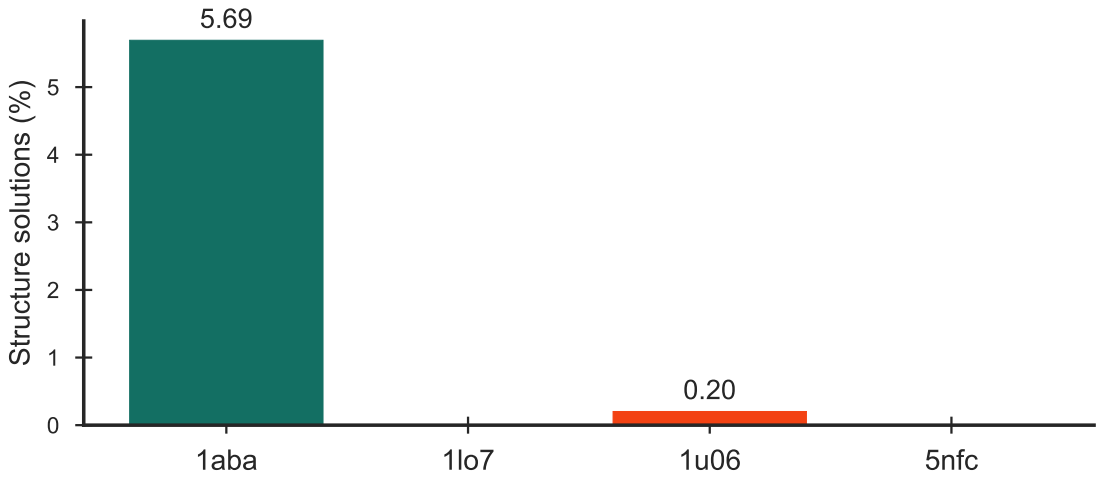

Figure 4.10: Distribution of structure solutions by FLIB target. All MR attempts total to 19,716, out of which 299 are structure solutions. Values above each bar indicates percentage search models successful out of the corresponding set.

The total of 299 MR structure solutions were achieved by 70 sequence-unique fragments. Sixty-nine of those fragments were picked from 60 unique structures for the T4 glutaredoxin (PDB ID: 1aba) leading to 97% of all structure solutions. In comparison, a single fragment, selected from three different fragment libraries, led to 9 structure solutions of the α-spectrin SH3 domain (PDB ID: 1u06). The largest FLIB fragment leading to a structure solution contained 37 residues and the smallest 10.

A division of FLIB-fragment search models by their respective origin libraries provides strong evidence that METAPSICOV STAGE 1 contact predictions allows for the selection of the most accurate fragments (Fig. 4.4), which directly translates into the structure solution count (Fig. 4.11). Furthermore, this division also highlights and supports the quality of fragment libraries picked with top-L (6 residues sequence separation) METAPSICOV STAGE 1 predictions. Trialling the optimal fragment picking strategy with and without helical fragments ($> 90\%$ α-helical content assigned using DSSP) resulted in the library without outperforming the other (Fig. 4.11, 3^{rd} and 4^{th} bars).

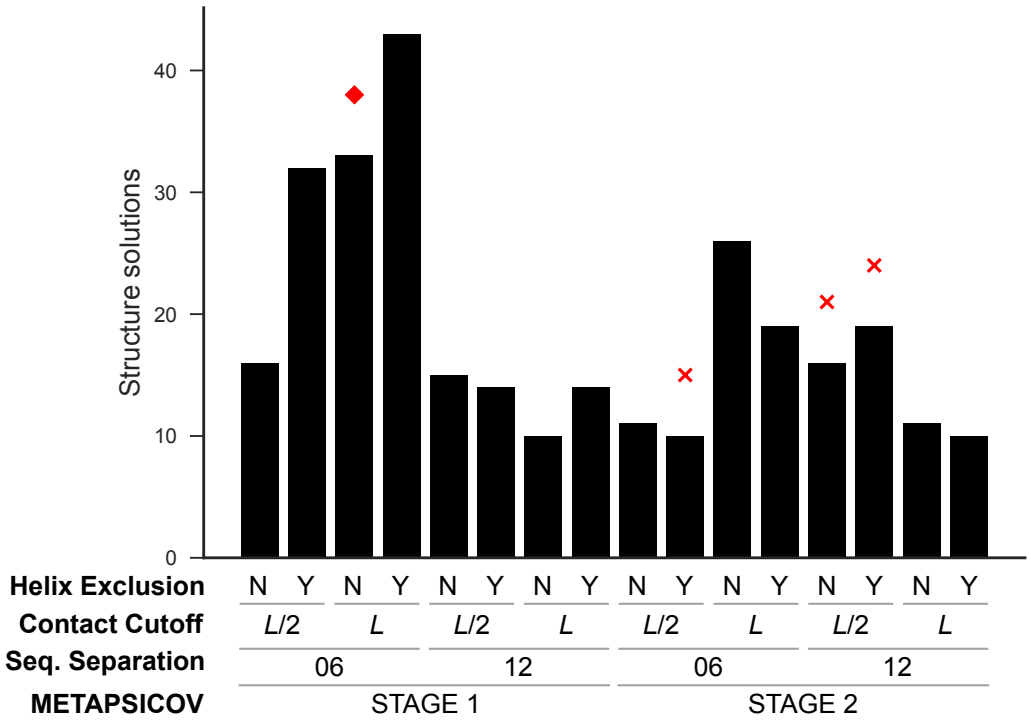

Figure 4.11: Distribution of structure solutions by FLIB library configuration. The optimal fragment picking strategy, as assessed by FLIB values, is highlighted with a red diamond to illustrate that the method that picks the best fragments is close to, but not the absolute best for ultimate structure solution. Fragment picking strategies leading to solutions of α-spectrin SH3 domain (PDB ID: 1u06) are highlighted with red crosses.

An analysis of the binned results by fragment-ranking or PHASER RMSD value confirms the expected outcome: the top fragments selected by fragment RMSD score result in more structure solutions than their FLIB score counterparts (Fig. 4.12). To reiterate, all FLIB fragments were grouped by their peptide length, and the top fragment in each group selected when sorted by either FLIB or RMSD values. When separating the total number of structure solutions by the score that made each fragment the best in its original library, it becomes clear that two-thirds of solutions were achieved with fragments scoring best by RMSD. However, the structure of α-spectrin SH3 domain (PDB ID: 1u06) was only solved with fragments that scored best in their FLIB fragment libraries by FLIB score. A further subdivision of successful fragments, sorted either by FLIB scores or RMSD values, highlights that a larger proportion of successful RMSD-sorted fragments satisfied at least 1 contact (FLIB-sorted: 7%; RMSD-sorted: 13%). A separation of attempts by PHASER input RMSD value suggests a value of 0.1 to be the most favourable.

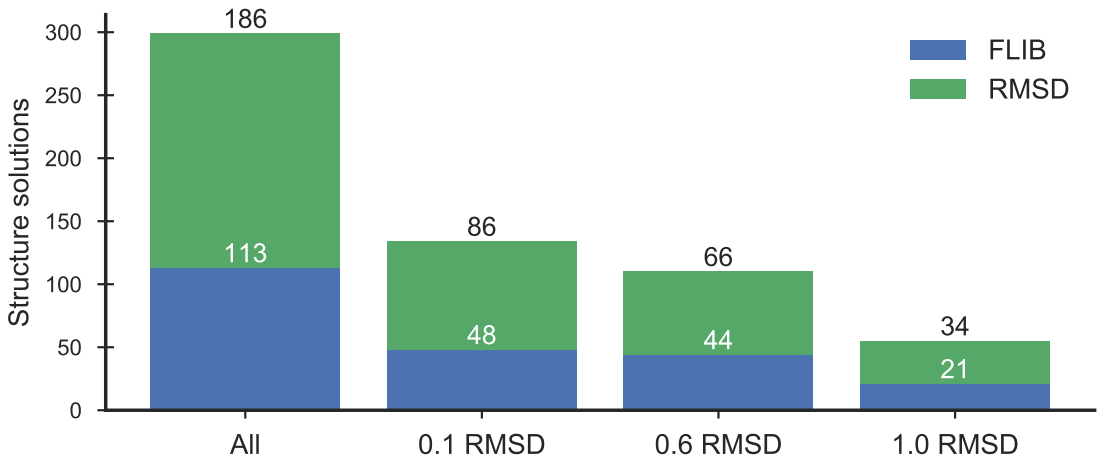

Figure 4.12: Distribution of structure solutions by fragment and MRBUMP configuration. The structure solution count is provided above each bar.

In MR, the correct placement of very small structural fragment may not always be detectable by the output metrics of underlying software. In benchmarking exercises, the RIO metric has shown to be a very useful and powerful metric to detect such situations [116, 117]. Given that the peptide lengths of FLIB fragments in this study range from 6 to 63 residues, the RIO score is most suitable in validating the correct placement of FLIB-fragment search models. Indeed, all fragments with SHELXE CC $\geq$ 25 and ACL $\geq$ 10 contain at least 3 correctly placed Cα atoms (i.e. a RIO score $\geq$ 3). Furthermore, the RIO metric indicates that more than 500 fragments have Cα atoms placed within 1.5Å of any atom in the target structure. However, only 4 residues are on average placed correctly, which was not enough to achieve structure solution (Fig. 4.13). All successful FLIB fragments have a minimum model- and target-normalised RIO scores of 29.7% and 9.2% (Fig. 4.13, green markers).

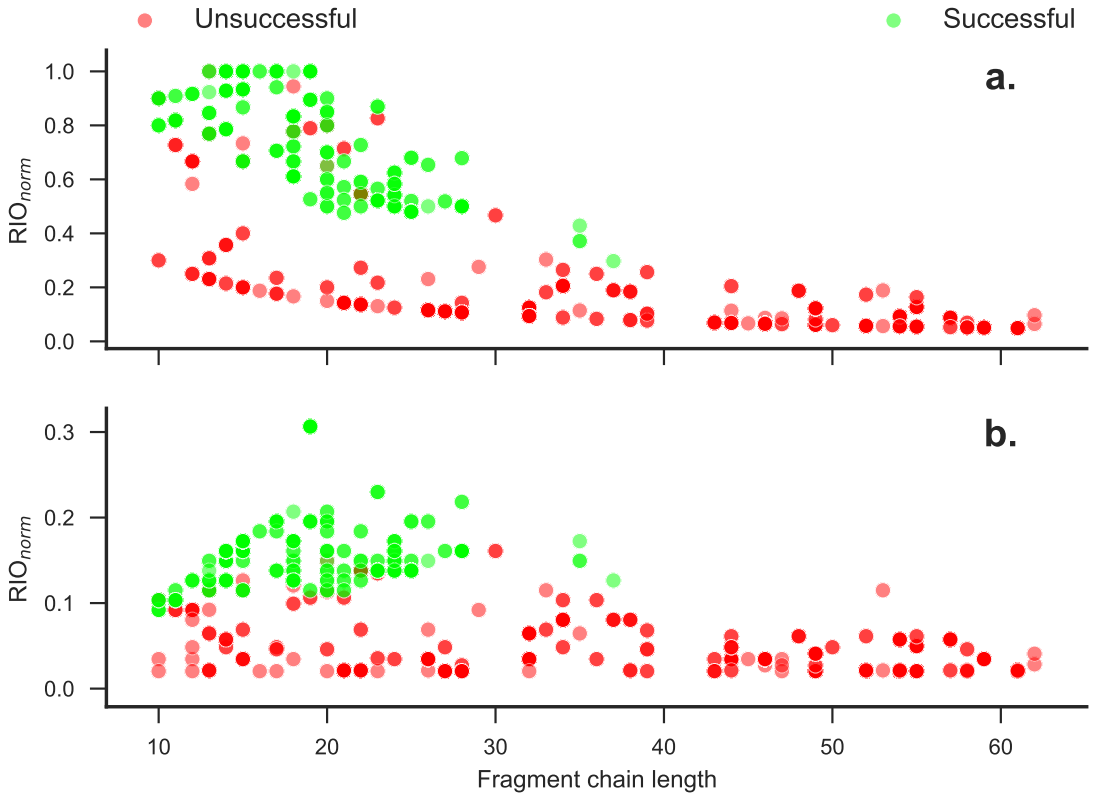

Figure 4.13: Dependence of normalised Residue-Independent Overlap (RIO_{norm}) score on the fragment chain length. The two plots show RIO scores normalised by the chain lengths of (a) the fragment and (b) the target. Colour coding indicates if the FLIB-fragment search model resulted in a structure solution. Each plot contains 890 fragment points; however, not all points are visible due to the superposition of individual scatter points because the same fragment was scored under different MR conditions.

In 33 MR attempts more than 60% of a fragment's residues were placed correctly, yet structure solution was not achieved. These trials affect exclusively fragments picked for the target sequences of T4 glutaredoxin (PDB ID: 1aba) and 4-hydroxybenzoyl CoA thioesterase (PDB ID: 1lo7). Overall, the 33 MR attempts made were done with 17 fragments extracted from 15 templates containing between 10 and 23 amino acids. The fragments' RMSD values range from 0.19 to 2.72Å with a mean RMSD of 1.10Å. Surprisingly, almost all of these fragments contain primarily α-helices. Given the presence of helices in the fold of both targets (Fig. 4.1) and the success of idealised fragments to solve such targets with data resolution < 2.0Å, it is a surprise to not see more structure solutions from these fragments.

Finally, the co-evolution data used in this study select fragments is a novelty in the field. Thus, it is of great interest to identify if fragments leading to structure solution satisfy many predicted residue-residue contacts. Eighty-seven percent ($n = 61$) of all unique fragments leading to structure solutions for either target satisfy no predicted residue-residue contact. The remaining nine fragments, all of which lead to structure solutions of T4 glutaredoxin (PDB ID: 1aba), satisfy either one ($n = 4$), two ($n = 4$) or 24 ($n = 1$)

predicted contacts.

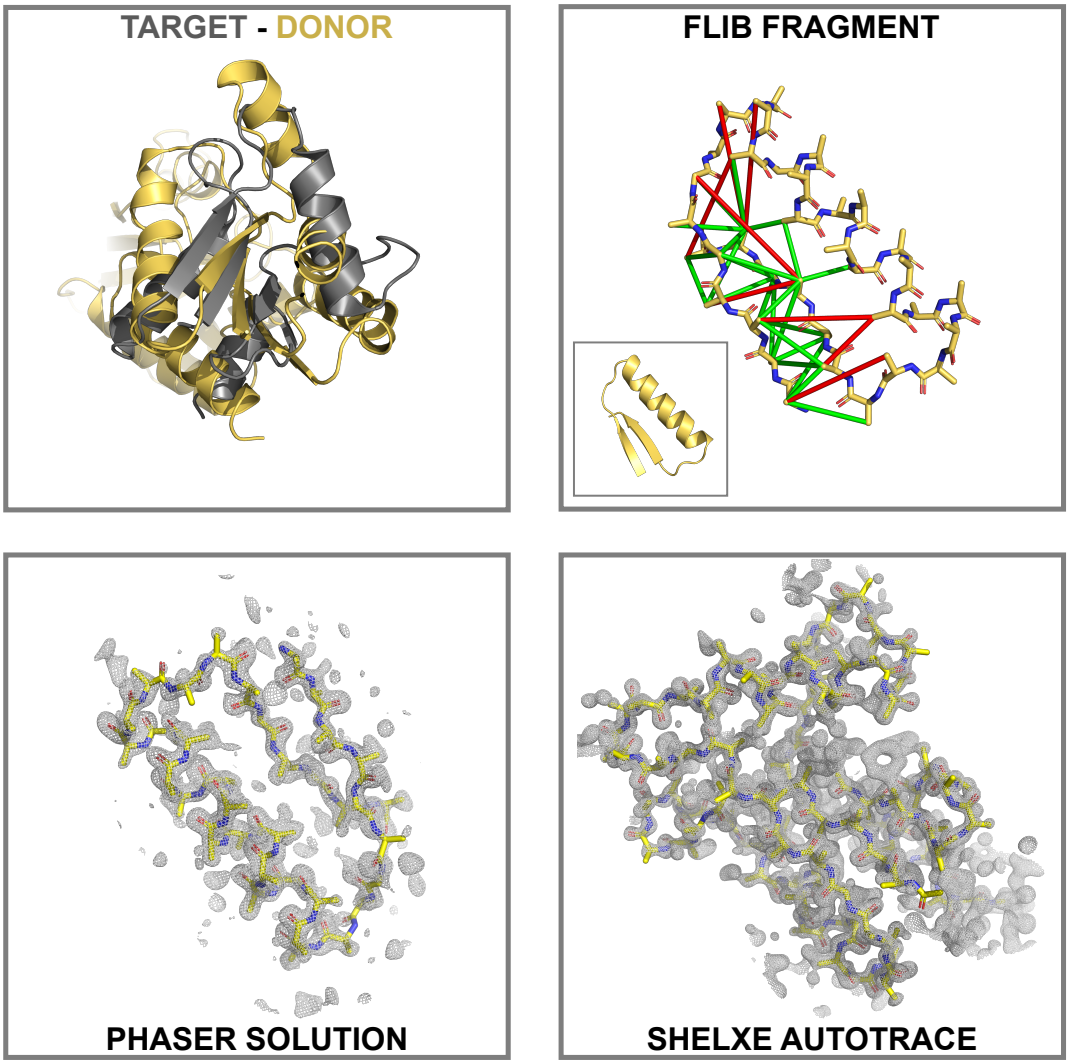

Figure 4.14: Intermediary steps from donor structure to SHELXE main-chain autotrace for a fragment derived from cobalt chelatase found in *Salmonella typhimurium* (PDB ID: 1qgo). The structure solution was obtained against the target crystallographic data of T4 glutaredoxin (PDB ID: 1aba). METAPSICOV STAGE 2 predicted contacts, against which the fragment was selected, are illustrated with True Positive (green) and False Positive (red) contacts (distance cutoff of 8Å). 2mFo-DFc electron density maps shown at 2.0 sigma and radius around the peptide atoms of 5Å. The RMSD between the sequence-independently superposed structures of target and donor is 10.384Å (computed with the `super` command in PyMOL [210]).

The fragment with 24 satisfied contacts is a particularly striking example of the value of the approach explored in this study (Fig. 4.14). The fragment was derived from the template structure of cobalt chelatase found in *Salmonella typhimurium* (PDB ID: 1qgo). The picked fragment contains 35 residues and its supersecondary structure consists of a two-strand β-sheet packing against a single α-helix. The majority of satisfied contact pairs are between Cβ atoms of the β-strands; however, a small number of individual contact

pairs also identifies the packing of one β-strand against the α-helix (Fig. 4.14, top-right). Although not considered at this stage in the FLIB algorithm, this particular fragment satisfies 75% of all relevant contact pairs. Most importantly though, this fragment was derived from an entirely unrelated protein structure, and thus illustrated the value in *ab initio* structure prediction fragments as MR search models.

4.4 Discussion

The main objective of this study was to investigate the application of FLIB structural fragments to MR. Four experimental datasets were chosen and 16 FLIB fragment libraries built per target sequence varying primarily in the predicted residue-residue contact information. A selection of highest scoring fragments were then forwarded to MRBUMP to trial each fragment as MR search model. The findings in this study validate the concept of this approach. Firstly, a positive correlation between a fragment's FLIB score and RMSD value was identified. These correlations were target-independent and found, with various strengths, in all FLIB fragment libraries. Furthermore, this work has identified top-L (6 residue sequence separation) METAPSICOV STAGE 1 contact pairs to be the optimal selection of contact pairs for the FLIB algorithm when starting with METAPSICOV predictions. The additional noise, typically filtered in the second STAGE of the METAPSICOV algorithm [100], allowed for the selection of more accurate fragments across the entire target sequence. Lastly, trialling a selection of high-scoring FLIB fragments in routine MR showed the usefulness of such fragments in attempting to solve protein structures. Two out of four targets were successfully solved albeit only trialling a small proportion of FLIB fragments per library (mean MRBUMP runtime of 10.5 CPU hours per fragment).

Intuitively, most crystallographers would declare the limitations of this approach to be the size and quality of the selected FLIB fragments as well as the resolution of the crystallographic data. Although the former was long-thought to be a major limitation, more recent work highlighted the success of likelihood-based MR methods (i.e., PHASER [123]) with very small search models. McCoy et al. [211] demonstrated the successful *ab initio* MR structure solution of aldose reductase starting from as little as two correctly placed atoms. Furthermore, automated MR pipelines, such as AMPLE [113], ARCIMBOLDO [197], BORGES [198], FRAGON [212] or FRAP [213], also successfully demonstrated MR successes with search models comprising a fraction of the target structure. Thus, MR structure solutions with FLIB fragments as short as 6 residues should be considered possible, especially when high resolution data is available and the fragment size is proportionally large compared to target size.

MR search models need to be sufficiently accurate to derive phase information for successful structure solution. The findings in this study highlight the success of identifying accurate fragments solely by the fragment's FLIB score. Given that the FLIB implementation used in this study only selected fragments for positions with at least one available

contact pair, future research is required to identify the potential benefits of specifically selecting fragments that satisfy at least one contact pair. Furthermore, it is important to understand the potentially beneficial implications of using the contact satisfaction score in the FLIB score metric of a given fragment. In theory, higher precision scores should imply a closer match of the overall tertiary structure of the trialled region. Alternatively, selecting secondary structure motifs or substructures of templates by means of searching with a predicted contact map could be an attractive alternative. Recent studies indicated success in identifying sub-folds by means of Contact Map Overlap (CMO) [74, 214]. Further work also needs to explore the benefits of considering the expected Log-Likelihood Gain (eLLG) as a conceptual framework to identify the linked effects of the fragment search model size, its accuracy and the resolution on the solvability of a target structure McCoy et al. [211].

Nevertheless, FLIB fragments with near-identical subfolds to the target might not be traceable by current means of assessing structure solutions. Commonly, MR success is judged by the combination of SHELXE CC and ACL scores [125]. However, it is known that β-strands are notoriously difficult to trace, and thus SHELXE might not pick up on correctly placed search models. Although this study did not suffer from this problem for fragments containing primarily β-strands, it did have correctly placed α-helices without structure solutions. Thus, the approach taken in this study would benefit from improvements to the density modification and sequence tracing algorithms.

Finally, this work served primarily as proof-of-concept study, and thus attempted to explore a diversity of options. With a better understanding of input parameters future work could build on the work presented here and use a large-scale analysis to assess the suitability of this concept more thoroughly. Furthermore, improvements to the FLIB algorithm through the incorporation of co-evolution data should also improve the quality of *ab initio* structure predictions, which should result in a greater success rate of other MR pipelines, such as AMPLE [113].

Bibliography

[1] W Friedrich, P Knipping, M Laue, *Ann. Phys.* **1913**, *346*, 971–988.

[2] M Laue, *Ann. Phys.* **1913**, *346*, 989–1002.

[3] W. H. Bragg, W. L. Bragg, *Proceedings of the Royal Society A: Mathematical Physical and Engineering Sciences* **July 1913**, *88*, 428–438.

[4] W. L. Bragg, *Scientia* **1929**, *23*, 153.

[5] W. L. Bragg, *Nature* **Dec. 1912**, *90*, 410.

[6] J. D. Watson, F. H. C. Crick, Others, *Nature* **1953**, *171*, 737–738.

[7] D. C. Hodgkin, J Kamper, M Mackay, J Pickworth, K. N. Trueblood, J. G. White, en, *Nature* **July 1956**, *178*, 64–66.

[8] T. L. Blundell, J. F. Cutfield, S. M. Cutfield, E. J. Dodson, G. G. Dodson, D. C. Hodgkin, D. A. Mercola, M Vijayan, en, *Nature* **June 1971**, *231*, 506–511.

[9] C. C. Blake, D. F. Koenig, G. A. Mair, A. C. North, D. C. Phillips, V. R. Sarma, en, *Nature* **May 1965**, *206*, 757–761.

[10] M. F. Perutz, M. G. Rossmann, A. F. Cullis, H Muirhead, G Will, A. C. North, en, *Nature* **Feb. 1960**, *185*, 416–422.

[11] J. C. Kendrew, G Bodo, H. M. Dintzis, R. G. Parrish, H Wyckoff, D. C. Phillips, en, *Nature* **Mar. 1958**, *181*, 662–666.

[12] H. M. Berman, J. Westbrook, Z. Feng, G. Gilliland, T. N. Bhat, H. Weissig, I. N. Shindyalov, P. E. Bourne, *Nucleic Acids Res.* **Jan. 2000**, *28*, 235–242.

[13] B. Rupp, *Biomolecular crystallography : principles, practice, and application to structural biology*, English, Garland Science, New York, **2010**.

[14] M. G. Rossmann, *Acta Crystallogr. D Biol. Crystallogr.* **2001**, *57*, 1360–1366.

[15] M. G. Rossmann, en, *Acta Crystallogr. A* **Feb. 1990**, *46 (Pt 2)*, 73–82.

[16] C. R. Kissinger, D. K. Gehlhaar, D. B. Fogel, en, *Acta Crystallogr. D Biol. Crystallogr.* **Feb. 1999**, *55*, 484–491.

[17] N. M. Glykos, M Kokkinidis, en, *Acta Crystallogr. D Biol. Crystallogr.* **Feb. 2000**, *56*, 169–174.

[18] R. J. Read, en, *Acta Crystallogr. D Biol. Crystallogr.* **Oct. 2001**, *57*, 1373–1382.

[19] M. G. Rossmann, D. M. Blow, *Acta Crystallogr.* **Jan. 1962**, *15*, 24–31.

[20] M. Bayes, M. Price, *Philosophical Transactions of the Royal Society of London* **Jan. 1763**, *53*, 370–418.

[21] L. C. Storoni, A. J. McCoy, R. J. Read, en, *Acta Crystallogr. D Biol. Crystallogr.* **Mar. 2004**, *60*, 432–438.

[22] B. C. Wang, en, *Methods Enzymol.* **1985**, *115*, 90–112.

[23] V. Y. Lunin, *Acta Crystallogr. A* **Mar. 1988**, *44*, 144–150.

[24] G. M. Sheldrick, *Zeitschrift für Kristallographie - Crystalline Materials* **Jan. 2002**, *217*, 371.

[25] T. C. Terwilliger, en, *Acta Crystallogr. D Biol. Crystallogr.* **Aug. 2000**, *56*, 965–972.

[26] P. V. Afonine, R. W. Grosse-Kunstleve, N. Echols, J. J. Headd, N. W. Moriarty, M. Mustyakimov, T. C. Terwilliger, A. Urzhumtsev, P. H. Zwart, P. D. Adams, en, *Acta Crystallogr. D Biol. Crystallogr.* **Apr. 2012**, *68*, 352–367.

[27] G. N. Murshudov, P. Skubák, A. A. Lebedev, N. S. Pannu, R. A. Steiner, R. A. Nicholls, M. D. Winn, F. Long, A. A. Vagin, en, *Acta Crystallogr. D Biol. Crystallogr.* **Apr. 2011**, *67*, 355–367.

[28] G. M. Sheldrick, en, *Acta Crystallogr. D Biol. Crystallogr.* **Apr. 2010**, *66*, 479–485.

[29] V. S. Lamzin, A Perrakis, K. S. Wilson, *International Tables for Crystallography* **2001**, 720–722.

[30] T. Terwilliger, en, *J. Synchrotron Radiat.* **Jan. 2004**, *11*, 49–52.

[31] K. Cowtan, en, *Acta Crystallogr. D Biol. Crystallogr.* **Sept. 2006**, *62*, 1002–1011.

[32] B. Qian, S. Raman, R. Das, P. Bradley, A. J. McCoy, R. J. Read, D. Baker, en, *Nature* **Nov. 2007**, *450*, 259–264.

[33] D. J. Rigden, R. M. Keegan, M. D. Winn, en, *Acta Crystallogr. D Biol. Crystallogr.* **Dec. 2008**, *64*, 1288–1291.

[34] R. Das, D. Baker, en, *Acta Crystallogr. D Biol. Crystallogr.* **Feb. 2009**, *65*, 169–175.

[35] P. E. Leopold, M Montal, J. N. Onuchic, en, *Proc. Natl. Acad. Sci. U. S. A.* **Sept. 1992**, *89*, 8721–8725.

[36] C. B. Anfinsen, en, *Science* **July 1973**, *181*, 223–230.

[37] C. Levinthal, *Mossbauer spectroscopy in biological systems* **1969**, *67*, 22–24.

[38] M. Karplus, en, *Nat. Chem. Biol.* **June 2011**, *7*, 401–404.

[39] Wikipedia, Folding Funnel — Wikipedia, The Free Encyclopedia, [Online; accessed 09-April-2018], **2004**.

[40] J. Lee, P. L. Freddolino, Y. Zhang in *From Protein Structure to Function with Bioinformatics (2nd Ed.) Vol. 69*, (Ed.: D. J. Rigden), Springer Netherlands, Dordrecht, **2017**, pp. 3–35.

[41] J. Skolnick, en, *Curr. Opin. Struct. Biol.* **Apr. 2006**, *16*, 166–171.

[42] C. A. Rohl, C. E. M. Strauss, K. M. S. Misura, D. Baker, en, *Methods Enzymol.* **2004**, *383*, 66–93.

[43] D. Xu, Y. Zhang, en, *Proteins* **July 2012**, *80*, 1715–1735.

[44] M. Blaszczyk, M. Jamroz, S. Kmiecik, A. Kolinski, en, *Nucleic Acids Res.* **July 2013**, *41*, W406–11.

[45] T. Kosciolek, D. T. Jones, en, *PLoS One* **Mar. 2014**, *9*, e92197.

[46] S. H. P. de Oliveira, E. C. Law, J. Shi, C. M. Deane, en, *Bioinformatics* **Nov. 2017**, DOI `10.1093/bioinformatics/btx722`.

[47] J. Abbass, J.-C. Nebel, en, *BMC Bioinformatics* **Apr. 2015**, *16*, 136.

[48] Y. Shen, G. Picord, F. Guyon, P. Tuffery, en, *PLoS One* **Nov. 2013**, *8*, e80493.

[49] S. C. Li, D. Bu, X. Gao, J. Xu, M. Li, en, *Bioinformatics* **July 2008**, *24*, i182–9.

[50] I. Kalev, M. Habeck, en, *Bioinformatics* **Nov. 2011**, *27*, 3110–3116.

[51] D. Bhattacharya, B. Adhikari, J. Li, J. Cheng, en, *Bioinformatics* **July 2016**, *32*, 2059–2061.

[52] T. Wang, Y. Yang, Y. Zhou, H. Gong, en, *Bioinformatics* **Mar. 2017**, *33*, 677–684.

[53] S. H. P. de Oliveira, J. Shi, C. M. Deane, en, *PLoS One* **Apr. 2015**, *10*, e0123998.

[54] D. Gront, D. W. Kulp, R. M. Vernon, C. E. M. Strauss, D. Baker, en, *PLoS One* **Aug. 2011**, *6*, e23294.

[55] N Metropolis, S Ulam, en, *J. Am. Stat. Assoc.* **Sept. 1949**, *44*, 335–341.

[56] D Shortle, K. T. Simons, D Baker, en, *Proc. Natl. Acad. Sci. U. S. A.* **Sept. 1998**, *95*, 11158–11162.

[57] Y. Zhang, J. Skolnick, *J. Comput. Chem.* **2004**, *25*, 865–871.

[58] P. Bradley, K. M. S. Misura, D. Baker, en, *Science* **Sept. 2005**, *309*, 1868–1871.

[59] S Ołdziej, C Czaplewski, A Liwo, M Chinchio, M Nanias, J. A. Vila, M Khalili, Y. A. Arnautova, A Jagielska, M Makowski, H. D. Schafroth, R Kaźmierkiewicz, D. R. Ripoll, J Pillardy, J. A. Saunders, Y. K. Kang, K. D. Gibson, H. A. Scheraga, en, *Proc. Natl. Acad. Sci. U. S. A.* **May 2005**, *102*, 7547–7552.

[60] Y. Zhang, J. Skolnick, en, *Proc. Natl. Acad. Sci. U. S. A.* **May 2004**, *101*, 7594–7599.

[61] J. Yang, R. Yan, A. Roy, D. Xu, J. Poisson, Y. Zhang, en, *Nat. Methods* **Jan. 2015**, *12*, 7–8.

[62] A. Kryshtafovych, A. Barbato, B. Monastyrskyy, K. Fidelis, T. Schwede, A. Tramontano, en, *Proteins* **Sept. 2016**, *84 Suppl 1*, 349–369.

[63] C.-H. Tai, H. Bai, T. J. Taylor, B. Lee, en, *Proteins* **Feb. 2014**, *82 Suppl 2*, 57–83.

[64] Z. He, M. Alazmi, J. Zhang, D. Xu, en, *PLoS One* **Sept. 2013**, *8*, e74006.

[65] L. Kinch, S. Yong Shi, Q. Cong, H. Cheng, Y. Liao, N. V. Grishin, en, *Proteins* **Oct. 2011**, *79 Suppl 10*, 59–73.

[66] O. F. Lange, P. Rossi, N. G. Sgourakis, Y. Song, H.-W. Lee, J. M. Aramini, A. Ertekin, R. Xiao, T. B. Acton, G. T. Montelione, D. Baker, en, *Proc. Natl. Acad. Sci. U. S. A.* **July 2012**, *109*, 10873–10878.

[67] S. Raman, O. F. Lange, P. Rossi, M. Tyka, X. Wang, J. Aramini, G. Liu, T. A. Ramelot, A. Eletsky, T. Szyperski, M. A. Kennedy, J. Prestegard, G. T. Montelione, D. Baker, en, *Science* **Feb. 2010**, *327*, 1014–1018.

[68] C. Göbl, T. Madl, B. Simon, M. Sattler, en, *Prog. Nucl. Magn. Reson. Spectrosc.* **July 2014**, *80*, 26–63.

[69] D. S. Marks, L. J. Colwell, R. Sheridan, T. A. Hopf, A. Pagnani, R. Zecchina, C. Sander, en, *PLoS One* **Dec. 2011**, *6*, e28766.

[70] M. Michel, S. Hayat, M. J. Skwark, C. Sander, D. S. Marks, A. Elofsson, en, *Bioinformatics* **Sept. 2014**, *30*, i482–8.

[71] S. Ovchinnikov, L. Kinch, H. Park, Y. Liao, J. Pei, D. E. Kim, H. Kamisetty, N. V. Grishin, D. Baker, en, *Elife* **Sept. 2015**, *4*, e09248.

[72] S. Ovchinnikov, D. E. Kim, R. Y.-R. Wang, Y. Liu, F. DiMaio, D. Baker, en, *Proteins* **Sept. 2016**, *84 Suppl 1*, 67–75.

[73] M. Michel, D. Menéndez Hurtado, K. Uziela, A. Elofsson, *Bioinformatics* **2017**, *33*, i23–i29.

[74] S. Ovchinnikov, H. Park, N. Varghese, P.-S. Huang, G. A. Pavlopoulos, D. E. Kim, H. Kamisetty, N. C. Kyrpides, D. Baker, en, *Science* **Jan. 2017**, *355*, 294–298.

[75] S. Wang, S. Sun, Z. Li, R. Zhang, J. Xu, en, *PLoS Comput. Biol.* **Jan. 2017**, *13*, e1005324.

[76] W. R. Taylor, K Hatrick, en, *Protein Eng.* **Mar. 1994**, *7*, 341–348.

[77] U Göbel, C Sander, R Schneider, A Valencia, en, *Proteins* **Apr. 1994**, *18*, 309–317.

[78] E Neher, en, *Proc. Natl. Acad. Sci. U. S. A.* **Jan. 1994**, *91*, 98–102.

[79] I. N. Shindyalov, N. A. Kolchanov, C Sander, en, *Protein Eng.* **Mar. 1994**, *7*, 349–358.

[80] D. D. Pollock, W. R. Taylor, en, *Protein Eng.* **June 1997**, *10*, 647–657.

[81] A. S. Lapedes, B. Giraud, L. Liu, G. D. Stormo, en in *Statistics in molecular biology and genetics*, Institute of Mathematical Statistics, **1999**, pp. 236–256.

[82] A. Lapedes, B. Giraud, C. Jarzynski, **July 2012**.

[83] F. Simkovic, S. Ovchinnikov, D. Baker, D. J. Rigden, *IUCrJ* **May 2017**, *4*, 291–300.

[84] M. Weigt, R. A. White, H. Szurmant, J. A. Hoch, T. Hwa, en, *Proc. Natl. Acad. Sci. U. S. A.* **Jan. 2009**, *106*, 67–72.

[85] L. Burger, E. van Nimwegen, en, *PLoS Comput. Biol.* **Jan. 2010**, *6*, e1000633.

[86] S. Balakrishnan, H. Kamisetty, J. G. Carbonell, S.-I. Lee, C. J. Langmead, en, *Proteins* **Apr. 2011**, *79*, 1061–1078.

[87] F. Morcos, A. Pagnani, B. Lunt, A. Bertolino, D. S. Marks, C. Sander, R. Zecchina, J. N. Onuchic, T. Hwa, M. Weigt, en, *Proceedings of the National Academy of Sciences* **Dec. 2011**, *108*, E1293–E1301.

[88] D. T. Jones, D. W. A. Buchan, D. Cozzetto, M. Pontil, *Bioinformatics* **Jan. 2012**, *28*, 184–190.

[89] M. Ekeberg, C. Lövkvist, Y. Lan, M. Weigt, E. Aurell, en, *Phys. Rev. E Stat. Nonlin. Soft Matter Phys.* **Jan. 2013**, *87*, 012707.

[90] H. Kamisetty, S. Ovchinnikov, D. Baker, *Proceedings of the National Academy of Sciences* **Sept. 2013**, *110*, 15674–15679.

[91] S. Seemayer, M. Gruber, J. S??ding, en, *Bioinformatics* **Nov. 2014**, *30*, 3128–3130.

[92] T. A. Hopf, D. S. Marks in *From Protein Structure to Function with Bioinformatics*, (Ed.: D. J. Rigden), Springer Netherlands, Dordrecht, **2017**, pp. 37–58.

[93] R. R. Stein, D. S. Marks, C. Sander, en, *PLoS Comput. Biol.* **July 2015**, *11*, e1004182.

[94] T. A. Hopf, S. Morinaga, S. Ihara, K. Touhara, D. S. Marks, R. Benton, en, *Nat. Commun.* **Jan. 2015**, *6*, 6077.

[95] S. D. Dunn, L. M. Wahl, G. B. Gloor, en, *Bioinformatics* **Feb. 2008**, *24*, 333–340.

[96] D. S. Marks, T. A. Hopf, C. Sander, en, *Nat. Biotechnol.* **Nov. 2012**, *30*, 1072–1080.

[97] J. Andreani, J. Söding, en, *Bioinformatics* **June 2015**, *31*, 1729–1737.

[98] T. A. Hopf, L. J. Colwell, R. Sheridan, B. Rost, C. Sander, D. S. Marks, en, *Cell* **June 2012**, *149*, 1607–1621.

[99] M. J. Skwark, D. Raimondi, M. Michel, A. Elofsson, en, *PLoS Comput. Biol.* **Nov. 2014**, *10*, e1003889.

[100] D. T. Jones, T. Singh, T. Kosciolek, S. Tetchner, en, *Bioinformatics* **Apr. 2015**, *31*, 999–1006.

[101] T. Du, L. Liao, C. H. Wu, B. Sun, en, *Methods* **Nov. 2016**, *110*, 97–105.

[102] A. J. González, L Liao, C. H. Wu, *Bioinformatics* **2013**.

[103] G. Shackelford, K. Karplus, en, *Proteins* **2007**, *69 Suppl 8*, 159–164.

[104] J. Cheng, P. Baldi, en, *Bioinformatics* **June 2005**, *21 Suppl 1*, i75–84.

[105] H. Zhang, Q. Huang, Z. Bei, Y. Wei, C. A. Floudas, en, *Proteins: Struct. Funct. Bioinf.* **Mar. 2016**, *84*, 332–348.

[106] Z. Wang, J. Xu, en, *Bioinformatics* **July 2013**, *29*, i266–73.

[107] J. Ma, S. Wang, Z. Wang, J. Xu, en, *Bioinformatics* **Nov. 2015**, *31*, 3506–3513.

[108] B. Adhikari, J. Hou, J. Cheng, en, *Bioinformatics* **Dec. 2017**, DOI `10.1093/bioinformatics/btx781`.

[109] B. He, S. M. Mortuza, Y. Wang, H. B. Shen, Y. Zhang, en, *Bioinformatics* **Mar. 2017**, *33*, 2296–2306.

[110] M. Michel, M. J. Skwark, D. M. Hurtado, M. Ekeberg, A. Elofsson, en, *Bioinformatics* **Sept. 2017**, *33*, 2859–2866.

[111] S. H. P. De Oliveira, J. Shi, C. M. Deane, en, *Bioinformatics* **Feb. 2017**, *33*, 373–381.

[112] Q. Wuyun, W. Zheng, Z. Peng, J. Yang, *Brief. Bioinform.* **Oct. 2016**, bbw106.

[113] J. Bibby, R. M. Keegan, O. Mayans, M. D. Winn, D. J. Rigden, en, *Acta Crystallogr. D Biol. Crystallogr.* **Dec. 2012**, *68*, 1622–1631.

[114] R. M. Keegan, J. Bibby, J. M. H. Thomas, D. Xu, Y. Zhang, O. Mayans, M. D. Winn, D. J. Rigden, en, *Acta Crystallogr. D Biol. Crystallogr.* **Feb. 2015**, *71*, 338–343.

[115] F. Simkovic, J. M. H. H. Thomas, R. M. Keegan, M. D. Winn, O. Mayans, D. J. Rigden, en, *IUCrJ* **July 2016**, *3*, 259–270.

[116] J. M. H. Thomas, R. M. Keegan, J. Bibby, M. D. Winn, O. Mayans, D. J. Rigden, en, *IUCrJ* **Mar. 2015**, *2*, 198–206.

[117] J. M. H. Thomas, F. Simkovic, R. M. Keegan, O. Mayans, Y. Zhang, D. J. Rigden, C. Zhang, Y. Zhang, D. J. Rigden, *Acta Crystallographica Section D Structural Biology* **Dec. 2017**, *73*, 985–996.

[118] J. Bibby, R. M. Keegan, O. Mayans, M. D. Winn, D. J. Rigden, en, *Acta Crystallogr. D Biol. Crystallogr.* **Nov. 2013**, *69*, 2194–2201.

[119] D. J. Rigden, J. M. H. Thomas, F. Simkovic, A. Simpkin, M. D. Winn, O. Mayans, R. M. Keegan, *Acta Crystallographica Section D Structural Biology* **Mar. 2018**, *74*, 183–193.

[120] J. F. Bruhn, K. C. Barnett, J. Bibby, J. M. H. Thomas, R. M. Keegan, D. J. Rigden, Z. A. Bornholdt, E. O. Saphire, *J. Virol.* **2014**, *88*, 758–762.

[121] K. Hotta, R. M. Keegan, S. Ranganathan, M. Fang, J. Bibby, M. D. Winn, M. Sato, M. Lian, K. Watanabe, D. J. Rigden, C. Y. Kim, en, *Angewandte Chemie - International Edition* **Jan. 2014**, *53*, 824–828.

[122] R. M. Keegan, S. J. McNicholas, J. M. H. Thomas, A. J. Simpkin, F. Simkovic, V. Uski, C. C. Ballard, M. D. Winn, K. S. Wilson, D. J. Rigden, *Acta Crystallographica Section D Structural Biology* **Mar. 2018**, *74*, 167–182.

[123] A. J. McCoy, R. W. Grosse-Kunstleve, P. D. Adams, M. D. Winn, L. C. Storoni, R. J. Read, en, *J. Appl. Crystallogr.* **Aug. 2007**, *40*, 658–674.

[124] A. Vagin, A. Teplyakov, en, *Acta Crystallogr. D Biol. Crystallogr.* **Jan. 2010**, *66*, 22–25.

[125] A. Thorn, G. M. Sheldrick, en, *Acta Crystallogr. D Biol. Crystallogr.* **Nov. 2013**, *69*, 2251–2256.

[126] S. X. Cohen, M. Ben Jelloul, F. Long, A. Vagin, P. Knipscheer, J. Lebbink, T. K. Sixma, V. S. Lamzin, G. N. Murshudov, A. Perrakis, en, *Acta Crystallogr. D Biol. Crystallogr.* **Jan. 2007**, *64*, 49–60.

[127] W. Kabsch, C. Sander, en, *Biopolymers* **Dec. 1983**, *22*, 2577–2637.

[128] J. Vojtěchovský, K. Chu, J. Berendzen, R. M. Sweet, I. Schlichting, en, *Biophys. J.* **Oct. 1999**, *77*, 2153–2174.

[129] H. Eklund, M. Ingelman, B. O. Söderberg, T. Uhlin, P. Nordlund, M. Nikkola, U. Sonnerstam, T. Joelson, K. Petratos, en, *J. Mol. Biol.* **Nov. 1992**, *228*, 596–618.

[130] F. K. Athappilly, W. A. Hendrickson, en, *Structure* **Dec. 1995**, *3*, 1407–1419.

[131] S. Bañuelos, M. Saraste, K. D. Carugo, en, *Structure* **Nov. 1998**, *6*, 1419–1431.

[132] A. H. West, E. Martinez-Hackert, A. M. Stock, en, *J. Mol. Biol.* **July 1995**, *250*, 276–290.

[133] J. Ménétrey, E. Macia, S. Pasqualato, M. Franco, J. Cherfils, en, *Nat. Struct. Biol.* **June 2000**, *7*, 466–469.

[134] C. C. Thomas, S Dowler, M Deak, D. R. Alessi, D. M. van Aalten, en, *Biochem. J.* **Sept. 2001**, *358*, 287–294.

[135] S. Grizot, F. Fieschi, M. C. Dagher, E. Pebay-Peyroula, en, *J. Biol. Chem.* **June 2001**, *276*, 21627–21631.

[136] P. Sörme, P. Arnoux, B. Kahl-Knutsson, H. Leffler, J. M. Rini, U. J. Nilsson, en, *J. Am. Chem. Soc.* **Feb. 2005**, *127*, 1737–1743.

[137] C. A. Kim, M. Gingery, R. M. Pilpa, J. U. Bowie, en, *Nat. Struct. Biol.* **June 2002**, *9*, 453–457.

[138] J. B. Thoden, H. M. Holden, Z. Zhuang, D. Dunaway-Mariano, en, *J. Biol. Chem.* **July 2002**, *277*, 27468–27476.

[139] X. Zhang, J.-C. D. Schwartz, X. Guo, S. Bhatia, E. Cao, M. Lorenz, M. Cammer, L. Chen, Z.-Y. Zhang, M. A. Edidin, S. G. Nathenson, S. C. Almo, en, *Immunity* **Mar. 2004**, *20*, 337–347.

[140] B. A. Fields, H. H. Bartsch, H. D. Bartunik, F Cordes, J. M. Guss, H. C. Freeman, en, *Acta Crystallogr. D Biol. Crystallogr.* **Sept. 1994**, *50*, 709–730.

[141] Y. Cheng, S. M. Sequeira, L. Malinina, V. Tereshko, T. H. Söllner, D. J. Patel, en, *Protein Sci.* **Oct. 2004**, *13*, 2665–2672.

[142] M. Graille, C. Z. Zhou, V. Receveur-Bréchot, B. Collinet, N. Declerck, H. Van Tilbeurgh, en, *J. Biol. Chem.* **Apr. 2005**, *280*, 14780–14789.

[143] T. Merz, S. K. Wetzel, S. Firbank, A. Plückthun, M. G. Grütter, P. R. E. Mittl, en, *J. Mol. Biol.* **Feb. 2008**, *376*, 232–240.

[144] D. A. K. Traore, A. J. Brennan, R. H. P. Law, C. Dogovski, M. A. Perugini, N. Lukoyanova, E. W. W. Leung, R. S. Norton, J. A. Lopez, K. A. Browne, H. Yagita, G. J. Lloyd, A. Ciccone, S. Verschoor, J. A. Trapani, J. C. Whisstock, I. Voskoboinik, en, *Biochem. J.* **Dec. 2013**, *456*, 323–335.

[145] S. J. Atkinson, P. E. Soden, D. C. Angell, M. Bantscheff, C.-W. Chung, K. A. Giblin, N. Smithers, R. C. Furze, L. Gordon, G. Drewes, I. Rioja, J. Witherington, N. J. Parr, R. K. Prinjha, en, *Med. Chem. Commun.* **Feb. 2014**, *5*, 342–351.

[146] B. T. Porebski, A. A. Nickson, D. E. Hoke, M. R. Hunter, L. Zhu, S. McGowan, G. I. Webb, A. M. Buckle, en, *Protein Eng. Des. Sel.* **Mar. 2015**, *28*, 67–78.

[147] A. M. Crowe, P. J. Stogios, I. Casabon, E. Evdokimova, A. Savchenko, L. D. Eltis, en, *J. Biol. Chem.* **Jan. 2015**, *290*, 872–882.

[148] R. D. Finn, P. Coggill, R. Y. Eberhardt, S. R. Eddy, J. Mistry, A. L. Mitchell, S. C. Potter, M. Punta, M. Qureshi, A. Sangrador-Vegas, G. A. Salazar, J. Tate, A. Bateman, en, *Nucleic Acids Res.* **Jan. 2016**, *44*, D279–D285.

[149] J. M. Chandonia, N. K. Fox, S. E. Brenner, en, *J. Mol. Biol.* **Feb. 2017**, *429*, 348–355.

[150] G. E. Tusnády, Z. Dosztányi, I. Simon, en, *Nucleic Acids Res.* **Jan. 2005**, *33*, D275–8.

[151] B. P. Klaholz, A. Mitschler, D. Moras, en, *J. Mol. Biol.* **Sept. 2000**, *302*, 155–170.

[152] W. T. Lowther, N Brot, H Weissbach, B. W. Matthews, en, *Biochemistry* **Nov. 2000**, *39*, 13307–13312.

[153] R. O. Louro, I. Bento, P. M. Matias, T. Catarino, A. M. Baptista, C. M. Soares, M. A. Carrondo, D. L. Turner, A. V. Xavier, en, *J. Biol. Chem.* **Nov. 2001**, *276*, 44044–44051.

[154] P. Kuser, D. R. Hall, L. H. Mei, M. Neu, R. W. Evans, P. F. Lindley, en, *Acta Crystallogr. D Biol. Crystallogr.* **May 2002**, *58*, 777–783.

[155] I. Hayashi, K. Vuori, R. C. Liddington, en, *Nat. Struct. Biol.* **Feb. 2002**, *9*, 101–106.

[156] G. David, K. Blondeau, M. Schiltz, S. Penel, A. Lewit-Bentley, en, *J. Biol. Chem.* **Oct. 2003**, *278*, 43728–43735.

[157] V. Oganesyan, D. Busso, J. Brandsen, S. Chen, J. Jancarik, R. Kim, S. H. Kim, en, *Acta Crystallographica - Section D Biological Crystallography* **July 2003**, *59*, 1219–1223.

[158] J. Liu, H. Yokota, R. Kim, S. H. Kim, en, *Proteins: Structure Function and Genetics* **June 2004**, *55*, 1082–1086.

[159] L. Cendron, A. Seydel, A. Angelini, R. Battistutta, G. Zanotti, en, *J. Mol. Biol.* **July 2004**, *340*, 881–889.

[160] L. Malinina, M. L. Malakhova, A. T. Kanack, M. Lu, R. Abagyan, R. E. Brown, D. J. Patel, en, *PLoS Biol.* **Nov. 2006**, *4*, 1996–2011.

[161] K. Makabe, S. Yan, V. Tereshko, G. Gawlak, S. Koide, en, *J. Am. Chem. Soc.* **Nov. 2007**, *129*, 14661–14669.

[162] A. W. Maresso, R. Wu, J. W. Kern, R. Zhang, D. Janik, D. M. Missiakas, M. E. Duban, A. Joachimiak, O. Schneewind, en, *J. Biol. Chem.* **Aug. 2007**, *282*, 23129–23139.

[163] C. U. Stirnimann, D. Ptchelkine, C. Grimm, C. W. Müller, en, *J. Mol. Biol.* **July 2010**, *400*, 71–81.

[164] L. Von Schantz, M. Håkansson, D. T. Logan, B. Walse, J. Osterlin, E. Nordberg-Karlsson, M. Ohlin, M. Hkansson, D. T. Logan, B. Walse, J. Österlin, E. Nordberg-Karlsson, M. Ohlin, en, *Glycobiology* **July 2012**, *22*, 948–961.

[165] S. J. Coulthurst, A. Dawson, W. N. Hunter, F. Sargent, en, *Biochemistry* **Feb. 2012**, *51*, 1678–1686.

[166] M. Myllykoski, A. Raasakka, M. Lehtimäki, H. Han, I. Kursula, P. Kursula, en, *J. Mol. Biol.* **Nov. 2013**, *425*, 4307–4322.

[167] X. Yang, M. Morita, H. Wang, T. Suzuki, W. Yang, Y. Luo, C. Zhao, Y. Yu, M. Bartlam, T. Yamamoto, Z. Rao, en, *Nucleic Acids Res.* **Dec. 2008**, *36*, 6872–6881.

[168] J. C. Grigg, C. X. Mao, M. E. P. Murphy, en, *J. Mol. Biol.* **Oct. 2011**, *413*, 684–698.

[169] H. Repo, J. S. Oeemig, J. Djupsjöbacka, H. Iwaï, P. Heikinheimo, en, *Acta Crystallogr. D Biol. Crystallogr.* **Nov. 2012**, *68*, 1479–1487.

[170] M. F. Matos, Y. Xu, I. Dulubova, Z. Otwinowski, J. M. Richardson, D. R. Tomchick, J. Rizo, A. Ho, en, *Proc. Natl. Acad. Sci. U. S. A.* **Mar. 2012**, *109*, 3802–3807.

[171] S. Moréra, I. Grin, A. Vigouroux, S. Couvé, V. Henriot, M. Saparbaev, A. A. Ishchenko, en, *Nucleic Acids Res.* **Oct. 2012**, *40*, 9917–9926.

[172] P. M. Collins, K. Bum-Erdene, X. Yu, H. Blanchard, en, *J. Mol. Biol.* **Apr. 2014**, *426*, 1439–1451.

[173] T. Weinert, V. Olieric, S. Waltersperger, E. Panepucci, L. Chen, H. Zhang, D. Zhou, J. Rose, A. Ebihara, S. Kuramitsu, D. Li, N. Howe, G. Schnapp, A. Pautsch, K. Bargsten, A. E. Prota, P. Surana, J. Kottur, D. T. Nair, F. Basilico, V. Cecatiello, S. Pasqualato, A. Boland, O. Weichenrieder, B. C. Wang, M. O. Steinmetz, M. Caffrey, M. Wang, en, *Nat. Methods* **Feb. 2015**, *12*, 131–133.

[174] K. Edman, A. Royant, P. Nollert, C. A. Maxwell, E. Pebay-Peyroula, J. Navarro, R. Neutze, E. M. Landau, en, *Structure* **Apr. 2002**, *10*, 473–482.

[175] J. Standfuss, A. C. T. Van Scheltinga, M. Lamborghini, W. Kühlbrandt, en, *EMBO J.* **Mar. 2005**, *24*, 919–928.

[176] J. K. Lee, D. Kozono, J. Remis, Y. Kitagawa, P. Agre, R. M. Stroud, en, *Proc. Natl. Acad. Sci. U. S. A.* **Dec. 2005**, *102*, 18932–18937.

[177] D. F. Savage, R. M. Stroud, en, *J. Mol. Biol.* **May 2007**, *368*, 607–617.

[178] D. Pogoryelov, Ö. Yildiz, J. D. Faraldo-Gómez, T. Meier, en, *Nat. Struct. Mol. Biol.* **Oct. 2009**, *16*, 1068–1073.

[179] K. R. Vinothkumar, K. Strisovsky, A. Andreeva, Y. Christova, S. Verhelst, M. Freeman, en, *EMBO J.* **Nov. 2010**, *29*, 3797–3809.

[180] J. D. Ho, R. Yeh, A. Sandstrom, I. Chorny, W. E. C. Harries, R. A. Robbins, L. J. W. Miercke, R. M. Stroud, en, *Proceedings of the National Academy of Sciences* **May 2009**, *106*, 7437–7442.

[181] N. H. Joh, A. Oberai, D. Yang, J. P. Whitelegge, J. U. Bowie, en, *J. Am. Chem. Soc.* **Aug. 2009**, *131*, 10846–10847.

[182] S. Ye, Y. Li, Y. Jiang, en, *Nat. Struct. Mol. Biol.* **Aug. 2010**, *17*, 1019–1023.

[183] M. G. Derebe, D. B. Sauer, W. Zeng, A. Alam, N. Shi, Y. Jiang, en, *Proceedings of the National Academy of Sciences* **Jan. 2011**, *108*, 598–602.

[184] H. Saino, Y. Ukita, H. Ago, D. Irikura, A. Nisawa, G. Ueno, M. Yamamoto, Y. Kanaoka, B. K. Lam, K. F. Austen, M. Miyano, en, *J. Biol. Chem.* **May 2011**, *286*, 16392–16401.

[185] G. B. Erkens, R. P. A. Berntsson, F. Fulyani, M. Majsnerowska, A. Vujiĉić-Žagar, J. Ter Beek, B. Poolman, D. J. Slotboom, en, *Nat. Struct. Mol. Biol.* **June 2011**, *18*, 755–760.

[186] J. Symersky, V. Pagadala, D. Osowski, A. Krah, T. Meier, J. D. Faraldo-Gómez, D. M. Mueller, en, *Nat. Struct. Mol. Biol.* **Apr. 2012**, *19*, 485–91, S1.

[187] R. P.-A. Berntsson, J. ter Beek, M. Majsnerowska, R. H. Duurkens, P. Puri, B. Poolman, D.-J. Slotboom, en, *Proceedings of the National Academy of Sciences* **Aug. 2012**, *109*, 13990–13995.

[188] S. Hayat, C. Sander, D. S. Marks, A. Elofsson, en, *Proc. Natl. Acad. Sci. U. S. A.* **Apr. 2015**, *112*, 5413–5418.

[189] M. Remmert, A. Biegert, A. Hauser, J. Söding, en, *Nat. Methods* **Dec. 2011**, *9*, 173–175.

[190] A. Bateman, M. J. Martin, C. O'Donovan, M. Magrane, E. Alpi, R. Antunes, B. Bely, M. Bingley, C. Bonilla, R. Britto, B. Bursteinas, H. Bye-AJee, A. Cowley, A. Da Silva, M. De Giorgi, T. Dogan, F. Fazzini, L. G. Castro, L. Figueira, P. Garmiri, G. Georghiou, D. Gonzalez, E. Hatton-Ellis, W. Li, W. Liu, R. Lopez, J. Luo, Y. Lussi, A. MacDougall, A. Nightingale, B. Palka, K. Pichler, D. Poggioli, S. Pundir, L. Pureza, G. Qi, S. Rosanoff, R. Saidi, T. Sawford, A. Shypitsyna, E. Speretta, E. Turner, N. Tyagi, V. Volynkin, T. Wardell, K. Warner, X. Watkins, R. Zaru, H. Zellner, I. Xenarios, L. Bougueleret, A. Bridge, S. Poux, N. Redaschi, L. Aimo, G. ArgoudPuy, A. Auchincloss, K. Axelsen, P. Bansal, D. Baratin, M. C. Blatter, B. Boeckmann, J. Bolleman, E. Boutet, L. Breuza, C. Casal-Casas, E. De Castro, E. Coudert, B. Cuche, M. Doche, D. Dornevil, S. Duvaud, A. Estreicher, L. Famiglietti, M. Feuermann, E. Gasteiger, S. Gehant, V. Gerritsen, A. Gos, N. Gruaz-Gumowski, U. Hinz, C. Hulo, F. Jungo, G. Keller, V. Lara, P. Lemercier, D. Lieberherr, T. Lombardot, X. Martin, P. Masson, A. Morgat, T. Neto, N. Nouspikel, S. Paesano, I. Pedruzzi, S. Pilbout, M. Pozzato, M. Pruess, C. Rivoire, B. Roechert, M. Schneider, C. Sigrist, K. Sonesson, S. Staehli, A. Stutz, S. Sundaram, M. Tognolli, L. Verbregue, A. L. Veuthey, C. H. Wu, C. N. Arighi, L. Arminski, C. Chen, Y. Chen, J. S. Garavelli, H. Huang, K. Laiho, P. McGarvey, D. A. Natale, K. Ross, C. R. Vinayaka, Q. Wang, Y. Wang, L. S. Yeh, J. Zhang, en, *Nucleic Acids Res.* **Jan. 2017**, *45*, D158–D169.

[191] J. Söding, en, *Bioinformatics* **Apr. 2005**, *21*, 951–960.

[192] Y. Zhang, J. Skolnick, en, *Proteins: Structure Function and Genetics* **Dec. 2004**, *57*, 702–710.

[193] J. Xu, Y. Zhang, en, *Bioinformatics* **Apr. 2010**, *26*, 889–895.

[194] M Fujinaga, R. J. Read, *J. Appl. Crystallogr.* **Dec. 1987**, *20*, 517–521.

[195] B. Adhikari, D. Bhattacharya, R. Cao, J. Cheng, en, *Proteins: Struct. Funct. Bioinf.* **Aug. 2015**, *83*, 1436–1449.

[196] B. Adhikari, J. Cheng, en, *BMC Bioinformatics* **Jan. 2018**, *19*, 22.

[197] D. Rodríguez, M. Sammito, K. Meindl, I. M. de Ilarduya, M. Potratz, G. M. Sheldrick, I. Usón, en, *Acta Crystallogr. D Biol. Crystallogr.* **Apr. 2012**, *68*, 336–343.

[198] M. Sammito, C. Millán, D. D. Rodríguez, I. M. De Ilarduya, K. Meindl, I. De Marino, G. Petrillo, R. M. Buey, J. M. De Pereda, K. Zeth, G. M. Sheldrick, I. Usón, en, *Nat. Methods* **Nov. 2013**, *10*, 1099–1104.

[199] D Frishman, P Argos, en, *Proteins* **Dec. 1995**, *23*, 566–579.

[200] N. Fernandez-Fuentes, J. M. Dybas, A. Fiser, en, *PLoS Comput. Biol.* **Apr. 2010**, *6*, e1000750.

[201] F. Delaglio, G. Kontaxis, A. Bax, *J. Am. Chem. Soc.* **Mar. 2000**, *122*, 2142–2143.

[202] G. Kontaxis, F. Delaglio, A. Bax, en, *Methods Enzymol.* **2005**, *394*, 42–78.

[203] T. A. Jones, S Thirup, en, *EMBO J.* **Apr. 1986**, *5*, 819–822.

[204] D. T. Jones, en, *J. Mol. Biol.* **Sept. 1999**, *292*, 195–202.

[205] R. Heffernan, K. Paliwal, J. Lyons, A. Dehzangi, A. Sharma, J. Wang, A. Sattar, Y. Yang, Y. Zhou, en, *Sci. Rep.* **June 2015**, *5*, 11476.

[206] S. F. Altschul, W. Gish, W. Miller, E. W. Myers, D. J. Lipman, en, *J. Mol. Biol.* **Oct. 1990**, *215*, 403–410.

[207] C. Camacho, G. Coulouris, V. Avagyan, N. Ma, J. Papadopoulos, K. Bealer, T. L. Madden, en, *BMC Bioinformatics* **Dec. 2009**, *10*, 421.

[208] J. Söding, A. Biegert, A. N. Lupas, en, *Nucleic Acids Res.* **July 2005**, *33*, W244–8.

[209] A. Biegert, C. Mayer, M. Remmert, J. Söding, A. N. Lupas, en, *Nucleic Acids Res.* **July 2006**, *34*, W335–9.

[210] W. L. DeLano, The PyMOL Molecular Graphics System, `http://www.pymol.org`, **Nov. 2002**.

[211] A. J. McCoy, R. D. Oeffner, A. G. Wrobel, J. R. M. Ojala, K. Tryggvason, B. Lohkamp, R. J. Read, en, *Proceedings of the National Academy of Sciences* **Apr. 2017**, *114*, 3637–3641.

[212] H. T. Jenkins, *Acta Crystallographica Section D Structural Biology* **Mar. 2018**, *74*, 205–214.

[213] R. Shrestha, K. Y. J. Zhang, *Acta Crystallogr. D Biol. Crystallogr.* **2015**, *71*, 304–312.

[214] D. W. A. Buchan, D. T. Jones, *Bioinformatics* **Sept. 2017**, *33*, 2684–2690.